Migration component dynamics in epithelial cell motility

Doctoral Thesis

submitted in partial fullfilment of the requirements
for the degree of

Doctor rerum naturalium (Dr. rer. nat.)

to the
Mathematisch-Naturwissenschaftliche Fakultät
of the
Rheinische Friedrich-Wilhelms-Universität Bonn

by
Kritika Sahni
from New Delhi, India

Bonn, April 2019

Angefertigt mit Genehmigung der Mathematisch-Naturwissenschaftlichen Fakultät der
Rheinischen Friedrich-Wilhelms-Universität Bonn

1. Gutachter (Betreuer) : Prof. Dr. Rudolf Merkel
2. Gutachter : Prof. Dr. Ulrich Kubitscheck
3. Fachnahes Mitglied: Prof. Dr. Arne Lützen
4. Fachfremdes Mitglied: Priv-Doz Dr. Gregor Kirfel

Tag der Promotion: 10.07.2019

Erscheinungsjahr: 2019

Thesis Information

Author:	Kritika Sahni
Title:	Migration component dynamics in epithelial cell motility
Matriculation number:	2946894
Document type:	Doctoral Thesis
Extent:	Number of pages- 135, Number of references- 159, Number of tables- 07, Number of figures- 65
Research institution:	Institute of Complex Systems: ICS-7 Forschungszentrum Jülich GmbH, Jülich, Germany
Submission date:	15.04.2019
Keywords:	Cell migration, Stress fibers, Focal adhesions, Protein dynamics, Cell polarity

Zusammenfassung

Die Zellmigration ist ein grundlegender Prozess in der Entwicklung und Erhaltung von multizellulärer Organismen. Harmonische Zellbewegungen werden durch fein abgestimmte Montage und Freisetzung von Zell-Substrat-Befestigungsstellen koordiniert. Die funktionelle Asymmetrie an der Vorder- und Rückseite der Zelle ermöglicht die Aktivierung/Deaktivierung spezifischer Moleküle, die bei der Bildung neuer Bindungsstellen an der Vorderseite und der Freisetzung alter an der Rückseite hilft. Diese Zellbindungspunkte sind diskrete Multi-Protein-Komplexe und werden als fokale Adhäsionen bezeichnet. Darüber hinaus fungiert das zytoskelettale Mikrofilamentnetzwerk als zelluläres Gerüst, das die Vorwärtsprotrusion der Zellvorderkante unterstützt und das gleichzeitige Zurückziehen der Zellhinterkante koordiniert. Das Mikrofilamentnetzwerk, das aus Aktin und Myosin besteht, ist in dünne Filamente und dicke Stressfasern unterteilt. Komponenten des Mikrofilamentnetzwerks arbeiten in Übereinstimmung miteinander und mit fokalen Adhäsionskomplexproteinen, um die Bildung diskreter Zellen vorne und hinten zu erleichtern und so die gerichtete Zellbewegung zu bestimmen. Eine effiziente Zellbewegung erfordert eine schnelle Neuanordnung (Montage-Demontagezyklen) von Mikrofilamenten und fokalen Adhäsionsnetzen.

In dieser Arbeit wurde das dynamische Verhalten von zytoskelettaler und fokaler Adhäsionskomponenten untersucht, wobei als Modellsysteme primäre menschliche epidermale Keratinozyten (nHEKs) verwendet wurden. Um den Transport von Molekülen sowie deren Austauschverhalten in verschiedenen subzellulären Strukturen während der Migration zu charakterisieren, wurde die grün-rote Photokonversionseigenschaft von dendra2 Fluorophor verwendet. In Kombination mit der Bildgebung von lebenden Zellen ermöglichte die lokalisierte lichtinduzierte Umwandlung von dendra2-getaggten Proteinen die Verfolgung ihrer Umverteilung und ihres strukturellen Umsatzes. Mit Hilfe von dendra2-Fusionskonstrukten aus Actin und Myosin wurden dynamische Eigenschaften beider Proteine in verschiedenen Arten von Stressfaserstrukturen identifiziert. Nach der Aktinverteilung durch zytosolischen Transfer zeigten Querbögen im Zellkörper einen sehr geringen Austausch für Aktin. Allerdings wurde ein höherer Aktinumsatz bei ventralen Stressfasern beobachtet, die sich am Zellrücken befinden. Im Gegensatz zu Actin zeigte Myosin keinen messbaren zytosolischen Transfer. Stattdessen erfolgte die Myosinausbreitung ausschließlich entlang des bestehenden Aktin-Stress-Fasernetzwerks. Die Myosinausbreitungsgeschwindigkeit entlang der hinteren ventralen Stressfaser wurde weiterhin beobachtet, um direkt mit der Gesamtgeschwindigkeit der Zellbewegung zu korrelieren.

Zusätzlich wurde in dieser Arbeit die Umsatzdynamik eines fokalen Adhäsions-Residenten Proteins, Vinculin, in verschiedenen fokalen Adhäsionstypen beobachtet. Die analysierten Adhäsionsarten waren aufkommende Adhäsionen (vorne), reife Adhäsionen (im Zellkörper) und disassemblierende Adhäsionen (hinten). Mit eigenen Bildverarbeitungswerkzeugen wurde ein schnellerer Vinculinumsatz von vordere aufkommenden Adhäsionen identifiziert, verglichen mit einem langsameren Umsatz von reifen Adhäsionen im Zellkörper. Interessanterweise wurden die langsam drehenden, reifen hinteren Fokusanhaftungen beobachtet, um ihre Austauschkinetik in einen schnelleren Rotationszustand zu versetzen, kurz vor der Demontage nahe der hinteren Zellenkante. Bei näherer Betrachtung zeigte die Demontage von Adhäsionskomplexen am hinteren Ende einen unterschiedlichen Umsatz an zwei gegenüberliegenden Enden. Das distale Ende, das dem äußeren Zellumfang zugewandt ist, zeigte einen höheren Umsatz als der Zellkörper, der dem proximalen Ende zugewandt ist.

Abstract

Cell migration is a fundamental process in development and maintenance of multicellular organisms. Harmonious cellular movement is coordinated by finely tuned assembly and release of cell-substrate attachment sites. Functional asymmetry at cell front and rear enables activation-deactivation of specific molecules that assists in formation of new attachment sites at front and release of old ones at rear. These cell attachment sites are discrete multi-protein complexes and are known as focal adhesions (FAs). Additionally, cytoskeletal microfilament network acts as cellular framework, which assists in forward protrusion of cell's leading edge and coordinates simultaneous retraction of cell's rear edge. Composed of actin and myosin, the microfilament network is arranged into thin filaments and thick stress fibers. Components of the microfilament network, work in accord with each other and with focal adhesion complex proteins, to facilitate the formation of discrete cell front and rear, thereby determining directional cellular movement. Efficient cell movement requires rapid rearrangement (assembly-disassembly cycles) of microfilament and focal adhesion network.

In this work, dynamic behavior of cytoskeletal and focal adhesion components was monitored, using migrating primary human epidermal keratinocytes (nHEKs) as model systems. In order to characterize transport of molecules as well as their exchange behavior in distinct sub-cellular structures during migration, green-to-red photoconversion property of dendra2 fluorophore was utilized. In combination with live cell imaging, localized light induced conversion of dendra2 tagged proteins enabled tracking down their redistribution and structural turnover. Using dendra2 fusion constructs of actin and myosin, dynamic properties of both proteins in different types of stress fiber structures were identified. Following actin distribution by cytosolic transfer, transverse arcs located in the cell body, demonstrated very low exchange for actin. However, higher actin turnover was observed in ventral stress fibers, located at cell rear. Unlike actin, myosin displayed no measurable cytosolic transfer. Instead, myosin propagation occurred exclusively along the existing actin stress fiber network. Myosin propagation speed along the rear ventral stress fiber, was further observed to correlate directly with overall speed of cell's movement.

Additionally, turnover dynamics of a focal adhesion resident protein, vinculin, in different focal adhesion types was monitored in this work. The analyzed adhesion types were nascent adhesions (at front), mature adhesions (in cell body) and disassembling adhesions (at rear). Using in-house image processing tools, faster vinculin turnover of frontal nascent adhesions was identified, compared to slower turnover of mature adhesions in the cell body. Interestingly, the slow turnover mature rear-end focal adhesions were

observed to switch their exchange kinetics to faster turnover state, shortly before disassembly close to the rear cell edge. Upon closer examination, the rear end disassembling adhesion complexes indicated differential turnover at two opposite ends. The distal FA end, facing the outer cell periphery, displayed higher turnover than the cell body facing proximal FA end.

Contents

CHAPTER 1

Introduction

Cell migration is known to play an essential role in many biological processes such as embryo development, cancer metastasis, skin renewal and wound repair. As an early response to migration stimuli, a stationary cell undergoes polarization [1] [2]. That is, in other words, in order to migrate most cell types undergo a spontaneous disruption of symmetry which causes cytoskeletal re-arrangement. In addition to cytoskeletal polarization, motile cells exhibit morphological polarization, making the cell front and the rear to be distinguished easily. Stationary fish keratocytes for example, were observed to have a circular morphology, with radially symmetric dense network of circular actin filaments around the cell body (figure 1.1-A). Motile keratocytes however display a crescent cell shape with an arched front and a flat rear (figure 1.1-B), along with a bilaterally symmetric actin filament network [3].

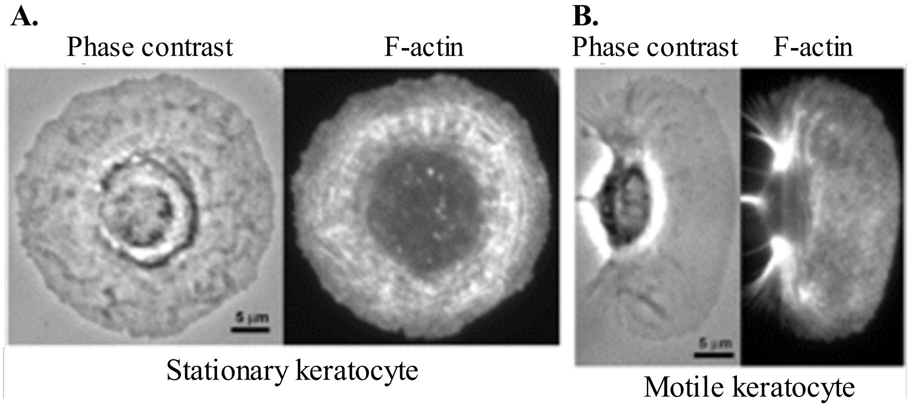

Figure 1.1: Fish keratocyte demonstrating morphological differences between (A) stationary and (B) motile states, with stationary state displaying a symmetrical actin cytoskeleton arrangement and motile state displaying asymmetrical actin arrangement. Scale bar = 5 μm. Modified from [3].

1.1 The migration cycle

Migration of cells is an integral process that requires functioning of several cellular processes. These processes operate together in a loop and can be divided into five major steps: (1) extension of the cell's leading (front) edge, (2) attachment of leading membrane to the underlying substrate, (3) contaction of the cell body, (4) release of attachment sites at cell rear and (5) transfer of membrane receptors from rear to the cell front [4] [5]. Factors initiating this cycle are mainly external cues, in form of chemical, mechanical and electrical stimuli which are sensed and communicated to cell interior by specific membrane receptors and downstream signalling molecules. In response to these signals, cells extend protrusions by rapid polymerization of a protein called actin, to form actin filaments [6]. This forms the cell front. Formation of new actin filaments pushes the membrane forward and provides the main driving force for advancing the cell's front edge [7] [8]. Once the direction for movement is established, the protruding edge then adheres to the surface on which it is moving via formation of new focal adhesion sites. In parallel to this, de-adhesion occurs at the cell's trailing edge. Finally, acto-myosin mediated contractions in the cell body and cell rear pulls the whole cell forward, completing the migration cycle [9]. Initial polarization, i.e. finely tuned actions of cell front and back is therefore needed for efficient directional progression.

1.1.1 Migration stimuli

Out of all known external cues that triggers migration, responses to chemical stimuli are the only ones that are known at the molecular level. Cell migration is known to be triggered by extracellular chemotactic agents, with a wide range of cytoplasmic signalling factors being activated either directly or indirectly following the activation of epidermal growth factor receptor (EGFR) [10] [11]. The extracellular growth factors of epidermal growth factor (EGF) family, activates specific receptor tyrosine kinases (RTKs) as a downstream response to EGFR activation [12]. The downstream signal transduction via RTKs is known to further regulate critical cellular processes including cell prolifiration and migration [13]. The direct or indirect effectors of EGFR signalling include phospholipase-Cγ (PLCγ), phosphatidylinositol-3-kinase (PI3K), extracellular signal regulated kinase (ERK) and protein kinase C (PKC) [14] [15] [16]. Actions of these soluble cytosolic factors include activation of transcription factors [17], polymerization of actin filaments at cell front [18], regulation of cytoskeletal contractility [19] and cell adhesion [20]. Activation of EGF receptor pathways is efficiently implicated in normal epidermal renewal, wound healing after injury, modulation of immune responses and carcinogenesis [21].

1.1.2 Polarization and moving forward

As a consequence of EGFR signalling, actin polymerization at the prospective cell front is established, leading to front-to-rear polarity on a molecular level. Following the internal polarization, two types of membrane structures are formed at cell front. The sheet like lamellipodium, which is a broad, flat plasma membrane extension and spike like filopodia [22], which are narrow, pointed protrusions. Together, both membrane protrusions mediate a random walk cell migration character. Extension of lamellipodia and filopodia in response to migration stimuli are coupled with the local actin polymerization. The rapid actin polymerization close to the membrane provides the pushing force for membrane extension and drives protrusions in the direction of migration. Organization of actin filaments differs for the two types of protrusions [23] (figure 1.2), where a branched 'dendritic' network of small actin filaments assists in lamellipodial extensions and long parallel actin filament bundles forms the filopodium [24].

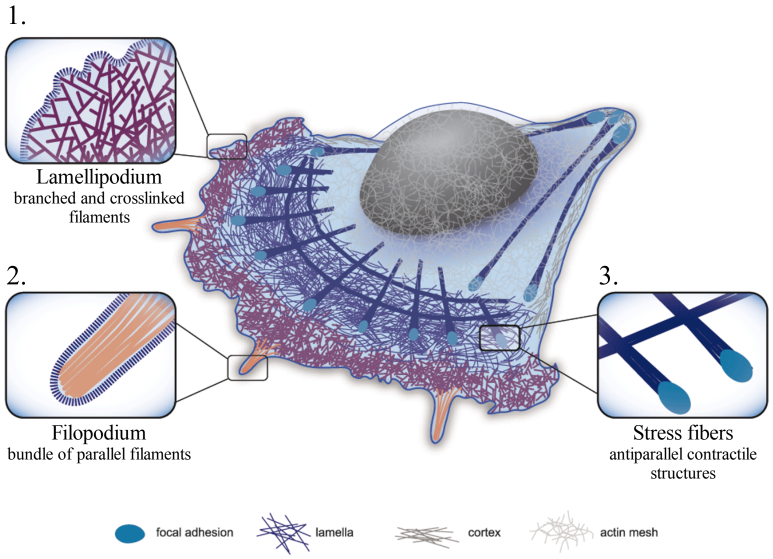

Figure 1.2: Cellular actin organization: (1) Lamellipodium- dense and branched network of short actin filaments involved in cell protrusion at front. (2) Filopodium- finger like membrane projection in cell protrusions consisting of bundled actin filaments. (3) Contractile filaments- myosin associated dynamic structures made up of anti-parallel actin filaments. Modified from [25].

For protrusions at leading edge to stabilize, they must form firm attachments with the underlying substrate. In migrating cells, new attachment points called focal adhesions (FAs) assemble at the protrusions [26] and adheres the protruding membrane to the extra-cellular matrix (ECM). New focal adhesion assembly occurs initially as small aggregates which gets attached to contractile actin filament arrays [27], through which the cell exerts forces at the substrate to facilitate its directional movement.In parallel to front protrusion, effective cell migration requires an efficient rear release. This release is mediated mainly by disassembling the rear adhesion complexes. Complete cell body translocation occurs due to myosin II mediated contractions in the cell body, especially at cell rear where it provides the push needed for forward movement and prevents formation of rear membrane protrusions [28] [29]. In addition, certain signaling molecules (members of Rho GTPase signaling pathway) [30] modulates depolymerization and severing of F-actin [31], which together with myosin II contraction contributes to the end detachment.

Overall, cell migration is envisioned to be a cyclic process of coordinated front protrusion and rear retraction, with clear functional and morphologic differences between the cell front and rear. Following morphological polarization, actin polymerization mediates front protrusions where the focal adhesion complexes are assembled. Myosin mediated cell body contractions and rear retraction further contributes to the forward propulsion and final displacement. Additional control of cell motility comes from FA complexes which are born as small complexes in the filopodial region and undergo stabilization and maturation. These FAs themselves remain stationary, functioning as anchors to the cell as it continues to glide over them. In this process, the stationary FAs are displaced towards the cell interior and undergo final disassembly on finding themselves at the cell rear. In parallel to migration itself, several molecule transport mechanisms operates to feed the ongoing actin filament and FA assembly-disassembly cycles. The determined modes of actin and FA component mobility include: (1) **Assisted transport**, where specific binding proteins recruit monomeric actin (G-actin) to the cell front [32]. (2) **Endocytic recycling**, where small vesicles assists in mobilizing the FA components [33] [34] [35]. (3) **Passive transport** where diffusion aids in intracellular actin [36] [37] and focal adhesion component [38] transport.

1.2 Cytoskeleton in non-muscle cells

Cell cytoskeleton is an organized cytosolic network of fibers, which is critical for cell migration. It helps support the cell membrane and maintains the inner organelle organization. There are three major classes of cytoskeletal fibers, namely: microfilaments, intermediate filaments and microtubules. Different cytoskeletal assemblies are built from non-covalent polymerization of monomeric protein subunits, to form primary filaments. These primary filaments are then arranged into discrete secondary structures like filament bundles, dome-like structures and gel like lattices.

Microfilaments: Monomeric actin subunits polymerizes to form spiral microfilament structures [39], which then spontaneously assembles into a dense meshwork that extends throughout the cell. The massive network of actin cytoskeleton lies beneath the cell cortex and can regulate cell shape changes just by assembling and disassembling itself. Actin filaments are the smallest among all cytoskeletal classes, with a filament diameter of about 6 nm.

Microtubules: Just like microfilaments, microtubules take part in cellular movement and molecular transport. In addition to this, they play a major role in organization of the cell through a microtubule organizing center (MTOC), which directs the orientation of organelles and decides the direction of vesicle trafficking. Microtubules are polymers of globular tubulin subunits, arranged in a tube-like structure and are thickest of all cytoskeletal filaments with a diameter of about 25 nm [40].

Intermediate filaments (IFs): Found in all animal cells, IFs are associated with nuclear and plasma membrane with their principal function in cell structure maintenance. In epithelial cells for instance, they are strong rope-like structures that provide mechanical support to the plasma membrane where it comes into contact with other cells or the ECM. A thick IF filament is approximately 16 nm in diameter. Unlike microfilaments, IFs do not contribute to cell motility or serving as tracks for motor protein mediated molecular transport [41].

Out of the three cytoskeletal arrangements, the microfilament network exclusively provides internal mechanical support to the cell, formulates contractions to mediate cell shape changes by modulating the cortical tension [42] and provides the force needed to drive cellular movement. Additionally, actin microfilament network is primarily responsible for establishing directed cellular movement [43] and is therefore the major focus in this study.

1.2.1 Microfilament assembly dynamics

Monomeric actin unit has a globular structure, hence it is named as globular actin or G-actin. X-ray crystallography studies revealed each of the globular units consists of two lobes separated by a cleft [44] (figure 1.3). This cleft holds an 'ATPase fold' that binds ATP and Mg^{2+}, where an autocatalysis hydrolyzes ATP into ADP and phosphate (P_i). Bound ATP or ADP states are known to affect the conformation of the G-actin molecule and plays crucial role in the polymerization process. G-actin end at which the ATP binding cleft is exposed to the surrounding environment is designated as the minus (-) or pointed end. The opposite, positive (+) or barbed end contacts the neighboring subunit and is not exposed to the surroundings. The asymmetric G-actin units undergoes reversible non-covalent polymerization to form filamentous actin (F-actin), which is a left-handed double helix [39]. The constituent G-actin subunits in the filament are oriented in the same direction, giving the final actin filament an intrinsic polarity with a '+' and a '-' end (figure 1.3).

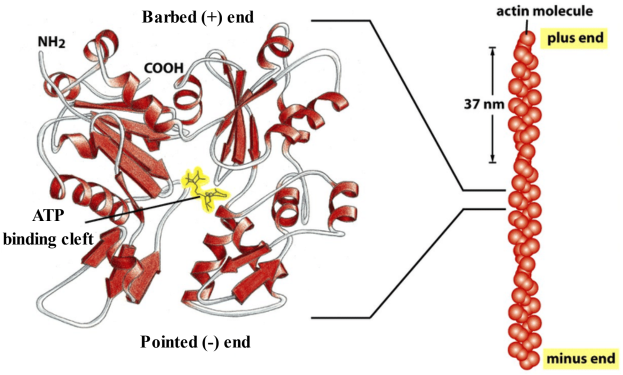

Figure 1.3: Crystal structure of globular G-actin monomer, with a central ATP binding cleft. The lower part of the cleft functions like a hinge, allowing the loops to undergo rearrangement. G-actin monomers are arranged into filament. A filament consists of two protofilaments held together by lateral contacts. Individual protofilament winds around each other as two parallel strands of a helix, with a twist repeating every 37 nm. All subunits within the filament have the same orientation. Modified from [45].

On a functional level, the two filament ends are known to grow at different rates, i.e. the rates of monomer addition at the two ends were found to be different [46]. Microinjection of rhodamine labelled actin to permeabilized cells demonstrated relatively faster incorporation of new actin units at barbed filament ends as compared to the pointed ends [47]. This functional polarity of actin filaments is especially significant at cell front, where the fast growing barbed end faces the cell membrane and provides the pushing force for forward protrusion [47] [18]. Actin polymerization factors such as filment severing cofilin proteins, produces free barbed ends for subunit addition, are found in large amounts at lamellipodial tips [18].

Nucleation and polymerization

Actin polymerization at cell front is controlled by availability of filament barbed ends [48], either by severing filaments [49] or by *de novo* nucleation [50]. Nucleating factors outsets the foundation for new filament synthesis. One such nucleating factor is the Arp2/3 (actin related protein) complex, which is a multi-protein complex of seven subunits and is concentrated in the lamellipodial region [51]. Arp2/3 along with other associated nucleation factors consists of WASP-homology 2 domain (WH2), which is a small actin binding motif that occurs in tandem repeats and binds three to four actin subunits to form a nucleus [52]. Arp2/3 complex therefore mimics an actin dimer (G-actin dimer) in the first nucleation step of *de novo* actin polymerization, forming a probe to which incoming monomeric units are added during filament elongation. In addition to its nucleation role, Arp2/3 complex occupies or caps the pointed ends of actin filaments and generates new barbed ends available for subunit addition. Thus, a single Arp2/3 complex binds simultaneously at pointed end of one filament and on side of another (figure 1.4), crosslinking the filaments into a branched network [53]. Figure 1.4 presents the proposed modes of Arp2/3 activation and its role in branched actin filament network formation.

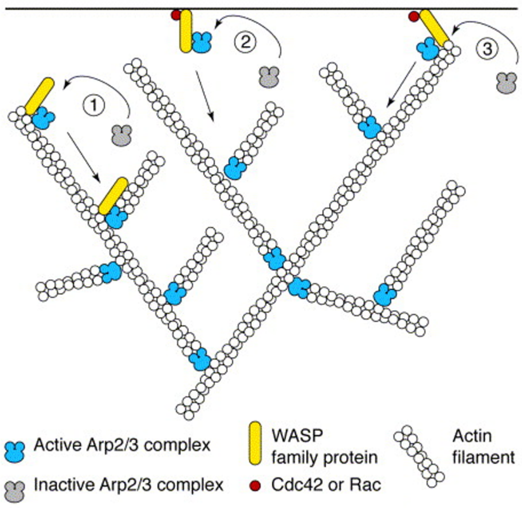

Figure 1.4: Proposed models for regulation of actin polymerization by Arp2/3 complex at cell's leading edge. (1) Activation of Arp2/3 complex by binding to Wiscott-Aldrich syndrome protein (WASP) and actin filaments. (2) Arp2/3 recruitment and activation at cell membrane by N-WASP, Cdc42 and phosphatidylinositol-(4,5)-bisphosphate. (3) Hybrid mechanism where Arp2/3 is activated at the membrane by simultaneous binding to WASP-family protein, Cdc42 and actin filament. Nucleation and filament branching then occur simultaneously. Adopted from [54].

Inactive Arp2/3 associates with the Scar/WASP family of proteins at the side of an existing actin filament. Once attached, Arp2/3 initiates nucleation of a new actin filament at this site, which is capped at its pointed end by Arp2/3 complex. The new filament grows in the barbed end direction, creating a branch from the old filament (figure 1.4-1). This model for the formation of actin filament network was named as 'dendritic nucleation model' [51]. Additionally, Arp2/3 activation takes place in response to migration stimuli at the membrane by the action of small GTPases like Cdc42 and Rac. Arp2/3 complex is activated at the membrane by WASP, Cdc42 and membrane lipid component phosphatidylinositol-(4,5)-bisphosphate. Upon initiation of nucleation, Arp2/3 complex and its associated actin filaments integrates into the branched filament network (figure 1.4-2) in the lamellipodium [55]. Together, activation of Arp2/3 nucleation at the membrane and formation of branched actin filament network provides structural basis for polymerization driven protrusions in the direction of migration.

Role of nucleotide binding in polymerization process

Actin filaments are dynamic structures which undergo cycles of G-actin subunit addition and removal. The globular G-actin structure explained previously (figure1.3), plays a crutial role in this filament cycling process. The large central nucleotide binding cleft (NBC) binds one nucleotide at a time such as adenosine-5$'$-triphosphate (ATP) or adenosine-5$'$-diphosphate (ADP) and a divalent cation (Mg^{2+} under physiological conditions). Although ATP is not required for polymerization process, actin monomers bound to ATP tend to polymerize much faster than those bound to ADP. ATP is rapidly hydrolysed to ADP and phosphate molecule (P_i) just upon polymerization by intrinsic ATPase activity of G-actin [56]. The resulting P_i is not released immediately, but rather remains non-covalently bound to the ADP in the NBC. Consequently, the rate of ATP hydrolysis is faster than the rate of P_i release and therefore the newly assembled parts of the filament contains mostly ADP-P_i protomers with a cap of ATP subunits at tips. Older filaments on the other hand have ADP protomers. Proteins of ADF/cofilin family then binds specifically to the ADP-F-actin [57] and enhances depolymerisation by increasing the rate constant of actin depolymerization at pointed ends and severes the actin filaments [58] (figure1.5).

Stability of filaments is described by actin's critical concentration (C_c), which is the concentration of free actin monomers in equillibrium with filaments, i.e. less stable filaments have higher C_c. As a consequence of spontaneous ATP hydrolysis, actin filaments are functionally polar, where ADP-actin end (pointed end) disassembles more readily (C_c ~0.7 μM). The depolymerized subunits supplies G-actin, which then adds to the opposite barbed end (C_c ~0.1 μM), after ADP in the NBC is exchanged to ATP. Once the steady state is reached, shortening of pointed ends is balanced by elongation of barbed end. At this state, the G-actin monomers still exchange with the filament subunits, but there is no net change in the total mass of the filament due to the parallel subunit disassembly. This ATP hydrolysis driven turnover is called 'treadmilling'. During steady state, length of the filament stays constant and newly added subunits travel through the filament, like on a treadmill until they reach the (-) end, where they dissociate. Turnover of actin filaments at the leading edge of moving cells occurs through treadmilling mechanism, where the growing barbed end faces the cell leading edge and the disassembling pointed end towards the rear of the cell.

Towards the interface region of cell lamellipodium and lamella, the branched actin meshwork is disrupted. Debranching involves dissociation of Arp2/3 created daughter filament from the parent filament. Biochemical studies indicate that debranching is related to ATP hydrolysis

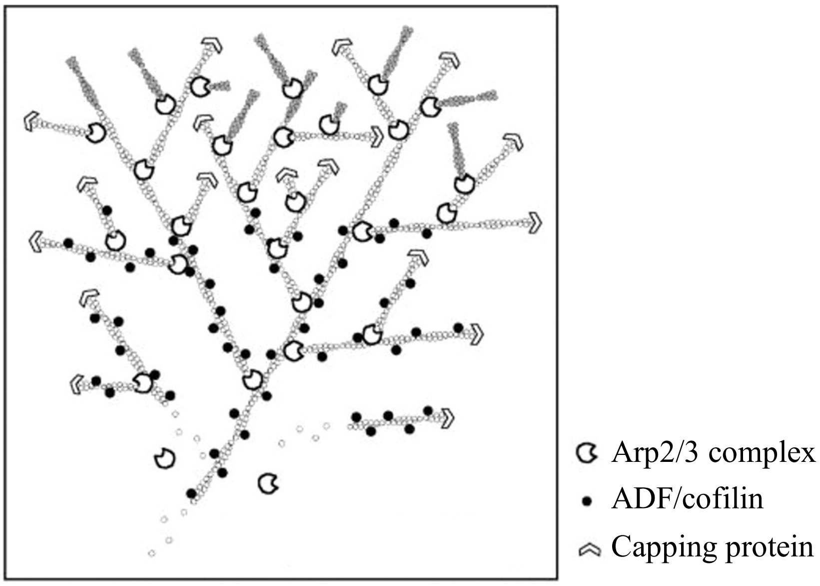

Figure 1.5: Treadmilling of dendritic actin array at leading edge. Newly formed filaments (dark gray) get incorporated into the existing array (light gray). Nucleation, cross-linking and pointed end capping is mediated by Arp2/3. Capping proteins (CAP) binds to the barbed ends to control their indefinite polymerization. Behind the actin brush, ADF/cofilin binds to the filaments and mediates pointed end depolymerization. Modified from [59].

on Arp2, leaving ADP-Arp2 bound to the parent filament [60], but activators of Arp2 ATP hydrolysis have not yet been identified. The debranched filament network is then stabilized at the lamellipodium-lamella interface region by association of actin binding myosin motor proteins. Myosin binding then organizes actin filaments to form thicker and stronger stacks, called stress fibers (SFs).

1.2.2 Stress fiber assembly

In addition to its role in providing the pushing force in cell protrusions, actin filaments mediates also the contractile forces to regulate rapid cell shape changes during migration. Similar to myofibrils of muscle cell, together with crosslinking α-actinin and myosin motor proteins, actin filaments assembles into contractile arrays called stress fibers (SFs) in non-muscle cells. Backward (retrograde) flow of pre-formed actin filaments from leading edge seeds the formation of contractile actomyosin bundles in the lamella region [61]. SFs are typically formed from clustering of 10-30 individual filaments [62]. SFs in non-motile cells are usually stable and thick, whereas those in motile cells are thinner and more dynamic. Unlike in muscle sarcomere, where each block of actin bundle must have opposite polarity to its successive block, in non-muscle cells actin stress fiber bundles show random orientation with respect to each other. In motile cells, SFs show graded polarity with uniform polarity at fiber ends, barbed ends facing outwards. Distribution of filament polarities however remains mixed at he center of the bundle [62]. Actin filaments alone are incapable of causing contractions. The force needed to execute such events, therefore comes from ATP driven movement of actin associated myosin motor protein (myosin II isoform in non-muscle cells) along the actin cables.

Three SF types were identified for the first time in fibroblasts and are classified on the basis of their subcellular localization [64]. Ventral stress fibers (VSF) are most abundant and were found to lie on the base of the cell, attched to integrin rich focal adhesions on both their ends. Dorsal stress fibers (DSF) are tethered at one end only to focal adhesions. Remaining part of this SF, rises towards the dorsal cell area and merges into a loose matrix of actin filaments. The third SF type are transverse arcs (TAs). These are bundles of actin filaments, formed behind the protrusive lamella, just beneath the dorsal cell surface. Assembly of each of the SF types occurs by different mechanisms [63]. (1) Transverse arcs are formed at the lamellipodium lamella interface region by end-to-end joining of short bundles of actin (nucleated and crosslinked by α-actinin in lamellipodium) to bundles of myosin (figure 1.6-A). Yet another mechanism of transverse arc assembly was proposed by Verkhosky et al., 1995 [65]. Aggregates of myosin at leading edge travels backwards in lamella by retrograde flow, to finally merge into the loose actin filaments at the base of protrusions. Transverse arcs remains as loose actin bundles with free ends on both sides. (2) Dorsal stress fibers are formed by formin (actin polymerization associated proteins) driven actin polymerization and elongate from focal adhesions as short actin filament bundles, crosslinked by α-actinin (figure 1.6-B). These bundles of actin donot contain myosin II and are therefore unable to contract. They however are attached on their proximal ends to contractile transverse arcs and link them to focal adhesions. (3) Ventral stress fibers are formed by end-to-end joining of two dorsal stress fibers, to form actin filament bundle which is anchored to focal adhesions at both ends (figure 1.6-C). Dorsal SF ends either find each other and joins to form VSF or they meet at transverse arcs, which disassembles as resulting bundle is pulled into the cell [63].

1.2.3 Arrangement of myosin II in stress fibers

Actin filaments in stress fibers, along with non-muscle myosin II (NMMII) are assembled into contractile assemblies. NMMII is a molecular motor, that converts chemical energy in the form of ATP to mechanical energy for filament sliding. It is localized to actin stress fibers in a repeating pattern that alternates with the actin cross-linker protein, α-actinin [66], resembling the sarcomere structure. NMII is a hexamer (two heavy chains: MHC, two regulatory light chains: RLC and two essential light chains: ELC) assembled into bipolar filaments, with fila-

A. Transverse arc assembly

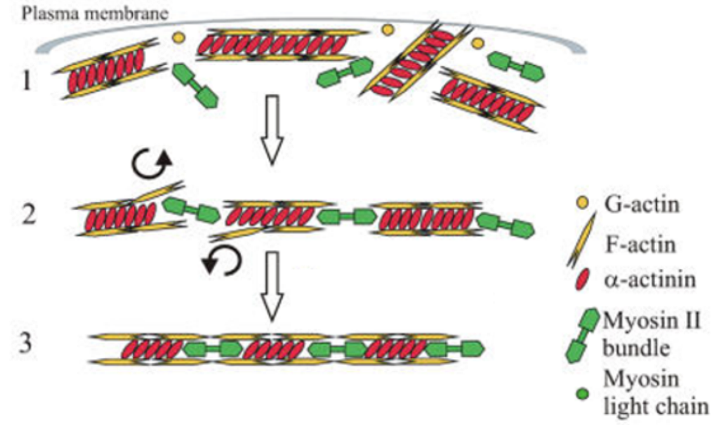

B. Dorsal stress fiber assembly

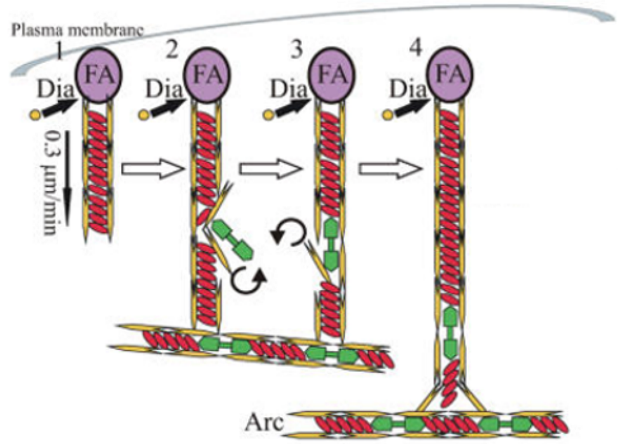

C. Ventral stress fiber assembly

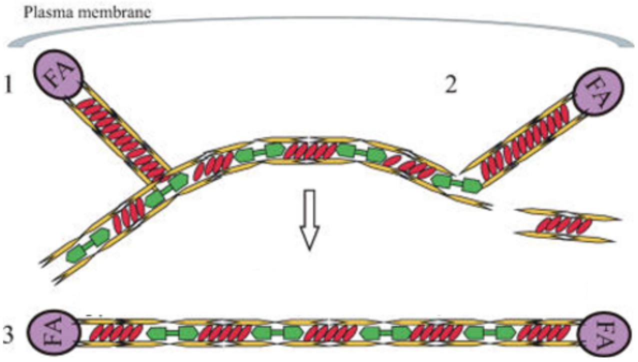

Figure 1.6: Schematic representation of stress fiber assembly. (A) Mini actin filaments built at cell front are stacked end-to-end at lamellipodium-lamella interface into transverse arcs, creating an alternating myosin and α-actinin pattern. (B) Formin (mDia) assisted polymerization of dorsal stress fibers which extend at their proximal end to contact transverse arcs. (C) Dorsal SF and transverse arc align together to evolve into ventral stress fiber. Modified from [63].

ment forming C-terminal tails localized to the center and N-terminal motor domains at the ends of the filament. This organized contractile assembly is responsible for exerting a pulling force on adjacent actin filaments [67] [68] (figure 1.7).

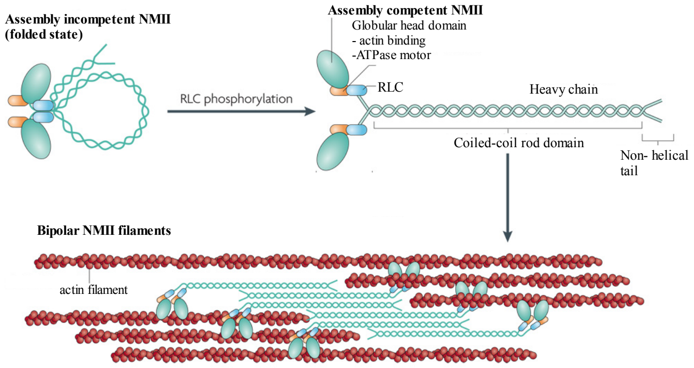

Figure 1.7: Bipolar NMII filament assembly: inactive NMII monomer is activated by regulatory light chain (RLC) phosphorylation. Heavy chains of open monomers interacts with each other and aligns on adjacent actin filaments, where myosin head binds to the actin filament. Modified from [68].

Actin filaments in contractile assemblies are interlocked with bipolar myosin II filaments, consisting of 15 to 20 individual myosin II molecules. The bipolar nature of NMII filaments allows it to exert a pulling force on actin filaments with anti-parallel orientation, leading to contraction. NMII attains a folded state in its unphosphorylated form, where one head blocks the second head of the same molecule [69] (figure 1.7-A). Phosphorylation by specific kinases at Ser^{19} and Thr^{18} of RLC, disrupts the head-head and head-tail interaction and causes the compact form to elongate (figure 1.7-B). Individual myosin II molecule is a dimer, containing two globular head domains with binding sites for ATP and actin. The neck regions consists of myosin light chains (MLC), which acts as a lever arm to support head rotation while energy from ATP is utilized in mechanical movement of the head domain. The extended rod domain is a long helical coiled domain, dimerizes two heavy chains (MHC) and terminates in a short non-helical tail. The rod domains of individual NMII dimer, self-associates in anti-parallel arrays between thin actin filaments to finally form a thick, bipolar actomyosin bundle.

Every myosin motor molecule is an ATPase and functions in a cyclical manner coupling ATP binding and hydrolysis to a conformational change in the protein. One round of ATP hydrolysis produces a single step of myosin on actin filament. The cycle of ATP binding to myosin molecule, its hydrolysis and single step movement occurs in a cyclical process called the ’power stroke cycle’ (reviewed in [71]). Steps involved in the cycle are as follows (figure 1.8):

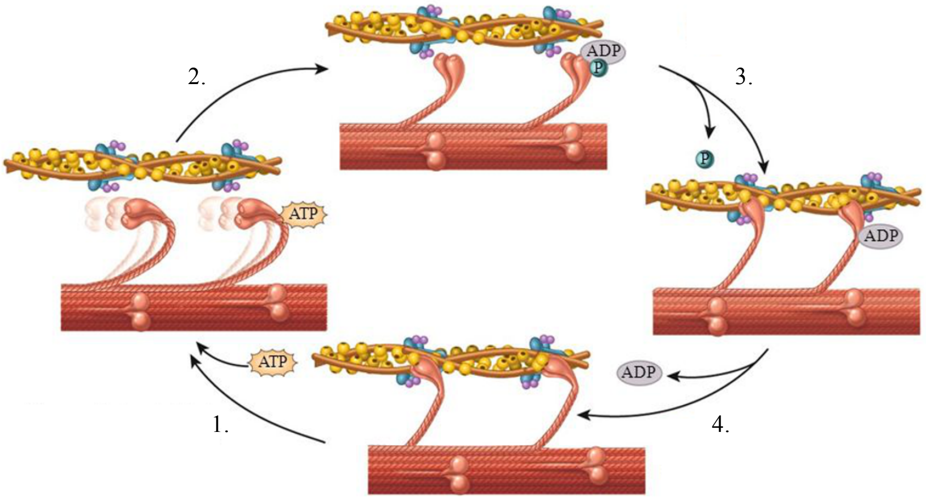

Figure 1.8: Power stroke cycle of myosin II head displacement on actin filament. The conformational changes involved in myosin head displacement on actin filaments depends upon ATP binding, its hydrolysis and subsequent ADP, P_i release. Image adopted from [70].

Step 1: At the end of one cycle, myosin molecule has an empty ATP binding site and is attached to the actin filament. This is a short-lived conformation, the 'rigor conformation'. ATP binding to myosin triggers a conformational change in the myosin's head domain. A shift in the actin binding site is induced, which reduces myosin's affinity for actin and the filament is released. ATP binding causes an additional conformational shift in the lever arm, which bends the myosin head to a cocked position.

Step 2: ATP is then hydrolysed by intrinsic ATPase activity of myosin. ADP and P_i remains bound to the myosin molecule.

Step 3: A weak contact between myosin and actin filament is then established and P_i molecule is released. Release of P_i makes the attachment of myosin and actin stronger and triggers the 'power stroke' state. This is the key force generating step in filament sliding. Myosin head then reverts back to its initial conformation, generating a pulling force on actin filament.

Step 4: As original conformation is achieved, myosin head releases ADP. Empty myosin holds on to the new position on actin filament, bringing the cycle back to the beginning.

The amount of time an individual NMII head spends attached to an actin filament is known as its ’duty ratio’. A single NMII motor (monomer) translocates towards the barbed end of an actin filament, with a low duty ratio of 0.1, spending only a small time in the bound state. Therefore, single motor itself is non-processive and does not move along the actin filaments over long distances. Bipolar myosin assemblies containing 10-30 individual myosin filaments however have larger duty ratios and function over long distances on actin filaments.

1.2.4 Stress fibers in tail retraction and actin retrograde flow

Non-muscle myosin plays substantial role in cell rear retraction during migration. Contractile forces generated by myosin II assists in rear detachment from the substrate. High phosphorylation of myosin light chain (MLC) was observed at rear areas in fibroblast cells, compared to low phosphorylation at leading edge [72]. This indicates high myosin contractile activity at cell rear. Inhibition of ROCK, a myosin II activating signalling molecule, caused migrating cells to leave a long tail behind them [73]. Additionally, mutants of myosin II were observed to show retarted motion compared to wild type cells [73]. Recent studies indicate that this function is particularly carried out by myosin IIa isoform [74]. Also, role of ventral stess fibers in maintaining cell migration directionality and persistence has been established [75], where they act as rudders in determining the long axis of the cell. Hence, in addition to maintainance of cell body contractions, stress fiber associated myosin II has been recognized to play critical roles in rear end retraction, regulating cell migration speed, migration directionality and persistence.

In migrating cells, actin dynamics varies with respect to spatial location in the same cell [62]. In the lamellipodium and filopodium, F-actin flows backwards or retrograde. In the cell lamella, F-actin remains stationary and at cell rear both inward flowing actin and stationary F-actin populations are found. Additional to assembly of dense actin network at leading cell edge, retrograde flow of the network away from the leading edge was observed in migrating fish keratocytes and the anterograde motion of actin at cell rear was also observed. This anterograde flow converged at cell body region with the retrograde flow, forming a tight zone of convergence at the lamellipodium-lamella interface [76]. Retrograde actin flow is thought to be a consequence of forces involved in forward propulsion of the cell: the polymerizing force at leading edge and actomyosin generated contractile forces for cell body contractions [77].

1.3 Focal adhesions

Stress fibers transmit contractile forces from inside of the cell to the underlying substrate through focal adhesion complexes. Focal adhesions (FAs) are multimolecular assemblies found at ventral cell surface, acting as feet of the cells aiding in their attachment to the underlying substrate. FAs are composed of more than 100 different proteins [78], arranged in a large cluster. They are integrin (trans-membrane dimers) containing assemblies, that form mechanical links between intracellular actin bundles and the extracellular matrix [79]. The versatile protein composition of FAs enables their mechanosensing and signalling functions. Some of the key FA proteins are shown in figure 1.9. Integrins are trans-membrane receptors consisting of external and internal domains. Upon their activation by specific ECM molecules like fibronectin, laminin and collagen outside the cell [80], integrins triggers signalling cascades on the cytoplasmic side, which involves activation of specific kinases (mainly tyrosine kinases). These kinases are focal adhesion kinases (FAK) and Src family of kinases. Phosphorylation of inactive FA proteins such as vinculin, paxilin, talin and VASP, leads to their activation and recruitment to the cytosolic integrin domains, forming a multi-molecular cluster. Some of the recruited focal complex proteins like vinculin and talin acts as adaptor molecules [81] to establish the attachment of FAs with actin cytoskeleton [82]. These discrete connection points relay forces across the cell membrane [83], which is essential for regulation of cell motility.

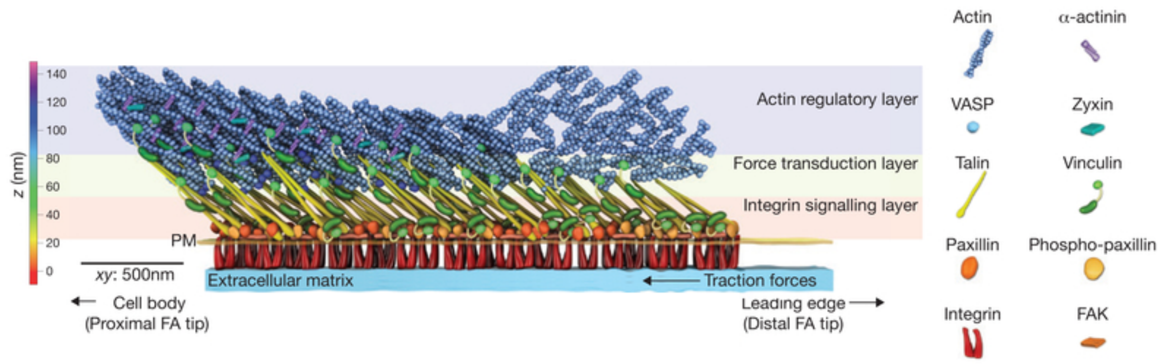

Figure 1.9: Architecture of the focal adhesion nano domains, linking the internal actin bundles to the cell extracellular matrix. These 3D clusters connects to lamellipodial denritic actin at their distal tips and with stress fibers at proximal tips. Focal adhesion residents like vinculin, paxilin, focal adhesion kinase and talin co-localize at cytoplasmic tails of trans-membrane integrin proteins. Image modified from [84].

The constituent FA proteins are organized in specific layers that corresponds to functions like receptor-matrix binding, linkage to actin cytoskeleton and force transduction, intracellular signal transdunction and regulation of actin polymerization. In sessile cells, FAs are stable complexes while in migrating cells, a coordinated formation and release of FAs is needed to maintain a directional migratory behavior. New focal complexes mechanically couples the lamellipodial actin network [79] to extracellular matrix at cell front. Simultaneously, adhesion sites at the trailing edge are disassembled as myosin-driven pulling forces moves the cell forward [85].

1.3.1 Vinculin as an adapter molecule

Vinculin is a 116 kD protein, which is a key regulator of FAs [78] [86]. Cells depleted of vinculin display reduced adhesion points, increased migration rates and fewer or smaller FAs [87] [88]. It is one of the first actin binding proteins recruited to FAs and functions in transducing forces across the cell membrane [89], thus controlling cell adhesion and mobility [88] [90]. Vinculin molecule is a three domain structure with a large 95 kDa N-terminal head domain, a flexible proline-rich hinge region and a 30 kDa C-terminal tail domain [14]. These three domains serve as binding sites for other FA proteins. The head and tail domains mainly interact with other focal adhesion proteins such as talin, paxilin, alpha-actinin and actin, whereas the proline linker mainly interacts with signaling molecules. Structural studies reveal that vinculin exists in two different conformations which depend upon interactions between its head and tail domains [91] [92] [93]. Intra-molecular binding of head to tail keeps the molecule in a closed conformation, limiting the accessibility of its docking sites. Phosphorylation by Src kinase mediates structural unfolding and subsequent activation of vinculin [94].

1.3.2 From nascent to mature

During cell migration, assembly of focal adhesions in the frontal lamellipodial region is highly regulated with protein recruitment occuring in a sequential manner. The early FA complexes assemble as a result of integrin-matrix binding at the leading edge are reffered as 'nascent adhesions'. Initially, small (0.25 μm^2) focal adhesions called focal complexes (FXs) are formed at the leading edge of the cell in the lamellipodium. While many FXs disappear during incomplete adhesion, others grow and develop into more stable nascent FAs. Once stable, nascent adhesions attaches to lamellipodial actin filaments via adapter proteins like vinculin and talin, and undergo centripetal elongation in the direction of actin retrograde flow (inward flow of actin). Growing adhesions increases the tractions on underlying substrate, slows down the retrograde flow [95] and reinforces attachment to actin filaments by recruitment of additional scaffolding FA proteins [78]. At the lamellipodium-lamella interface, due to contractile properties of actin filament associated myosin II, nascent adhesions experiences a continuous pulling force. Myosin II pulling force is hypothesized to bundle the associated actin filaments and as a consequence clusters the adhesion proteins attached to the filament end. This increases internal interactions among the adhesion proteins and results in increased integrin avidity [81]. Another hypothesis suggests that myosin generated forces on nascent FAs causes conformational changes in adhesion components, assisting their structural unfolding, exposing additional binding sites and therefore increases molecular clustering [96] [97]. FA formation and growth is dependent on myosin motor activity, particularly myosin IIa isoform, since the transformation of nascent contacts to mature and elongated FAs was observed to be compromised upon myosin

IIA knockout [98]. As a result, in response to myosin IIa contractility, mature FAs become larger in size and complexity during their growth.

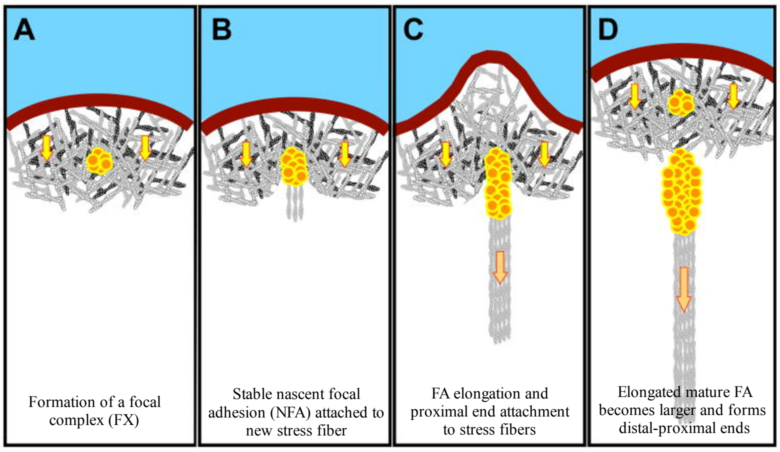

Figure 1.10: Stages of FA formation and maturation in the cell lamellipodium. The substrate is illustrated in blue and brown thick line is the leading cell edge. Yellow arrows symbolizes the retrograde actin flow. (A) Formation of a focal complex at the lamellipodial dendritic actin meshwork. (B) FA stabilization and connection to stress fiber precurson leads to the formation of nascent adhesion (NFA). (C) Elongation of attached stress fiber at proximal FA end and force-dependent growth of FA. (D) The larger mature FA and the attached stress fiber continues to grow in the lamella. Image modified from [99].

Simulation work from Golji *et al.* [100] suggests that vinculin in FAs promotes linkage to the F-actin filaments when stresses are present. The stress around vinculin activates the molecule and intensifies its linkage with actin filaments, strengthening the adhesion complex. Once a stable adhesion has been established in the lamelipodia, they then undergo further maturation into larger and more stable focal adhesions, along with recruitment of additional proteins such as zyxin, α-actinin and focal adhesion kinase (FAK). Figure 1.10 shows the sequence of formation of a new adhesion site in the leading lamellipodium and its overtime maturation. During transition from nascent to mature, focal adhesion morphology changes not only in terms of molecular complexity but also in functional symmetry. FA maturation process creates a symmetry break in the FA structure, forming a polar elongated complex with a distal tip (toe) and a proximal end (heel). Mature FAs attach at their proximal ends to contractile actomyosin bundles [63]. The changes in protein configuration underlying the distal-proximal compositional reorganization still remains to be elucidated.

Phosphorylation is another event associated with FA maturation. It is triggered by tension applied to the FA anchored adhesion complexes by the attached actin bundles [101] [102]. Kinases like FAK or c-Src are characterized kinases involved in phosphorylation of specific FA proteins such as vinculin [103]. Specific phosphorylation at Y100 and Y1065 of vinculin have been shown to play an important role in its activation, stabilization and ligand binding [103]. Such phosphorylation events stabilizes the open conformation of vinculin, exposing its ligand binding sites and enhancing binding affinities to other molecules of young FAs. Once in place, a focal adhesion remains stationary with respect to the extracellular matrix, and the cell uses this as an anchor on which it can push or pull itself over the ECM. As the cell progresses along its chosen path, a given focal adhesion moves closer and closer to the trailing edge of the cell [104]. The phosphorylation levels decreases again with FA aging [102], followed by their final disassembly at cell rear.

1.3.3 Polarized disassembly of adhesions at cell rear

Adhesions at the trailing edge of a migrating cell functions to restrain the cell body and maintain cell spreading. However, in process of moving forward, there is a need for rear attachments to be released for successful cell body translocation [85].

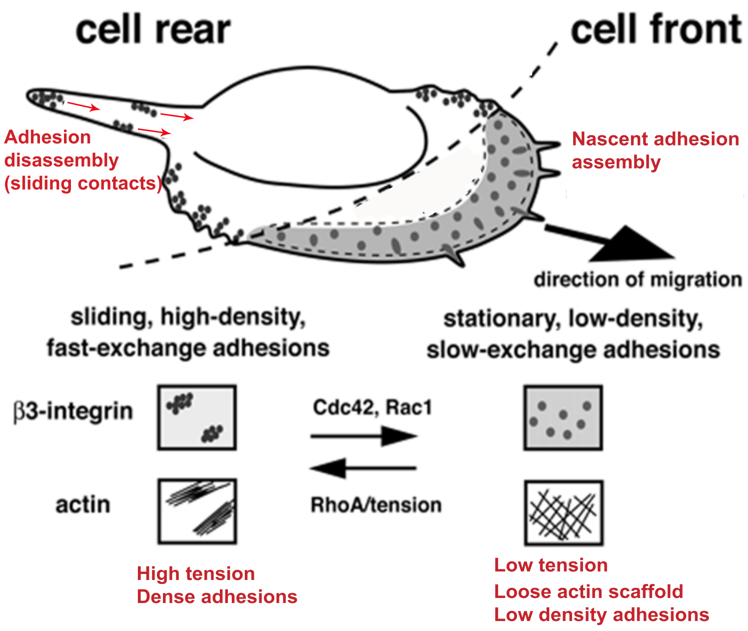

Figure 1.11: The overall migration of a cell is mediated by assembly of stationary, low density FAs at front, which upon finding themselves at cell rear become unfixed, undergoes sliding and finally disassemble to support rear retraction. Image modified from [107].

Breakage of cell-substrate linkage is thought to occur in several ways, including by intracellular disruption of cytoskeleton-integrin linkage, which is regulated mainly by the action of specific kinases or proteases that alters the affinity of integrins for their ECM ligands or by release of integrin-matrix linkage, which is usually a consequence of intracellular pulling forces exerted by the connected actomyosin bundles [105] [106]. Traction force measurements indicate vectorial contractile forces on FAs at cell rear, that pulls the adhesions centripetally inwards [62].

Fast migrating cells recover their integrin receptors from the detached cell rear by endocytic recycling [108]. Fast integrin turnover was observed in focal adhesions at cell's trailing edge [107]. Continuous loss of integrins from the distal FA edge and subsequent recruitment at proximal edge was observed. This gives an illusion of FA sliding in the proximal end direction (inwards: figure 1.11). Continuous inward sliding of FAs prior to their disassembly is a frequent event, which occurs in parallel with the trailing cell edge retraction [107].

1.4 Fluorescent proteins

Some special chemical compounds called fluorophores, have a unique ability of emitting light. These compounds have found extreme utility in cell biology research, where they are used to specifically tag sub-cellular components, which can then be visualized using a fluorescence microscope. Upon excitation by specific light energy, electrons from the ground state orbital gets excited to a higher energy orbital such that the electron in the excited state orbital is paired (with opposite spin) to a second electron in the ground state orbital. The consequent return of this excited state electron to its ground level is spin allowed and therefore occurs rapidly by emission of a photon. This phenomenon of rapid photon emission is called fluorescence, with typical emission rates of 10^8 sec^{-1}. Lifetime of a fluorophore is the time between its excitation and return to its ground state and is typically in the order of 10 ns (10 x 10^{-9} sec).

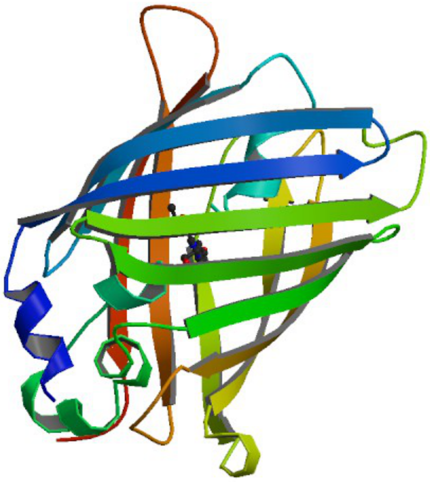

Figure 1.12: Representation of folded GFP polypeptide into a 11 stranded β-barrel structure, where the chromophore element lies flat in the central core of the barrel structure. Adopted from [109].

The fluorochrome element within fluorophores results from autocatalytic cyclization of the polypeptide backbone between residues Ser^{65} and Gly^{67} and oxidation of α-β bond of Tyr^{66} [110]. A combination of aminoacid side chains aligned on the inner side of the folded fluorophore (indicated in figure 1.12 for GFP), contributes to the fluorescent behavior. The chromophore element is also a highly conserved combination of a tripeptide R-Tyr-Gly, where R varies for different fluorophores and is responsible for specific fluorescence properties.

1.4.1 Photo-transformable fluorescent proteins (PTFPs)

Revolutions in recombinant DNA techniques has enabled scientists to introduce varieties of fluorescent molecules having unique abilities to undergo light induced modifications such as photoactivation, photoconversion, photoswitching and blinking. In 2003, the first efficient photo-transformable, kindling fluorescent protein (KFP) was discovered and tested for efficient tracking of the protein movement in living systems [111]. In the following years numerous light transformable fluorescent proteins emerged, which transformed the way molecular tracking was studied. These new members were further tuned to display different switching speed, efficient localization, better contrast, faster *in-vivo* folding times and high stability which reinforced their demand in research.

PTFPs belong to a characteristic group of fluorescent proteins that are capable of undergoing reversible or irreversible light induced transformations, forming spectrally distinguishable forms whose signal can be utilized with much more versatility than the conventional fluorescent proteins.PTFPs are capable of undergoing structural, chemical or physical changes in response to light. Such changes alter the fluorescence spectra of these fluorophores in a way that the modified form has different excitation/emission properties than the native form.

PTFPs can be classified into different categories on the basis of their response to light [112]:

1. **Photoactivable fluorescent proteins (PAFPs)**, which are irreversibly transformed from a non-fluorescent to a light emitting fluorescent state.
2. **Reversibly switchable fluorescent proteins (RSFPs)**, which can be switched reversibly between a non-fluorescent 'off' state and a fluorescent 'on'.
3. **Photoconvertable fluorescent proteins (PCFPs)**, which undergo a light induced chemical reaction resulting in an irreversible shifting of their emission spectrum.

In this study, we have exploited the ability of the photoconvertable fluorescent proteins (PCFPs) to irreversibly convert from one fluorescent form into another and therefore, will be the main focus for all further discussions.

1.4.2 Structure and photochemical conversion mechanism of dendra2

By offering an external control over their intensity and color of fluorescence, PCFPs allow a subset of molecules to be tagged and followed in real time within a cell. One of the many members of PCFP family known today is Dendra2, which is an engineered, monomeric GFP-like protein that undergoes light induced irreversible transformation from green to red fluorescent state upon induction with 405 nm light.

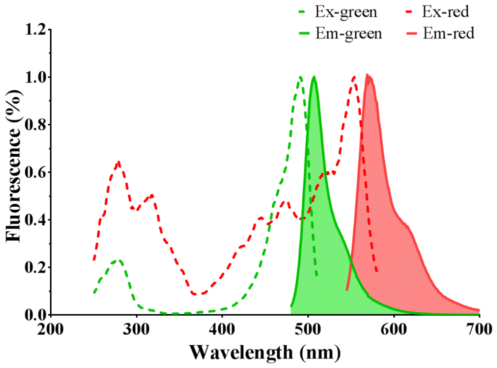

Figure 1.13: Fluorescence spectra of dendra2 native (green) and converted states (red). Dotted lines represents the excitation spectra and solid lines show their respective emission spectra. Modified from [115].

Dendra is a variant of dendGFP (tetrameric protein from Dendronephthyla sp. [113]), which was engineered to a smaller, monomeric form [114] to enable its utilization in protein labelling. Tyr188Ala, Asn121Lys and Met123Thr point mutations were introduced in dendGFP sequence to destabilize the dimer interface and thereby prevent dimer formation. Dendra2 comprises of a single Ala224Val substitution to enable better fluorophore folding and brighter fluorescence before and after photoconversion. Dendra2 chromophore element is His^{62}-Tyr^{63}-Gly^{64} tripeptide, which upon irradiation with 405 nm light, gets irreversibly photoconverted from its primary

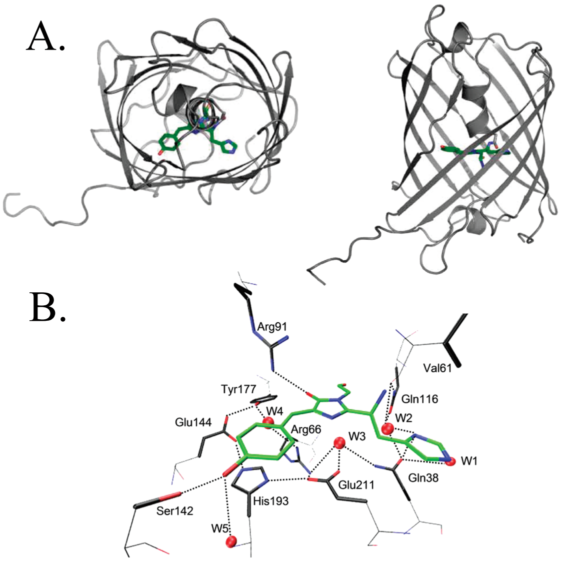

Figure 1.14: (A) Top and side view of folded dendra2 monomer with the embedded chromophore in the center shown in green. (B) Detailed overview of chromophore (shown by green carbon atoms) environment in dendra2. Red spheres represents the surrounding water molecules. H-bonds are indicated by dotted lines. Modified from [116].

green state (excitation and emission maxima at 486 nm and 505 nm, respectively) to a red (excitation and emission maxima at 558 nm and 575 nm, respectively) fluorescent state.

Dendra2 is a 230 amino acid polypeptide with molecular weight of 28 kDa. Its crystal structure has been observed to have a typical GFP-like β-barrel structure with a nearly planar chromophore (with imidazolinone and phenyl ring), rigidly held in the center by multiple hydrogen bonds and van der Waals interactions (figure 1.14), which provides protection from the bulk solvent by the β-barrel and its interconnecting loops [116]. The cis conformation of the chromophore is stabilized by hydrogen bonds from the tyrosine oxygen atom to the Ser^{142} oxygen (2.7Å) and to a water molecule (W5, 2.8Å). The carbonyl oxygen of the imidazolinone ring hydrogen-bonds with the side chain of Arg^{91} (2.9Å).

Mechanism of light induced dendra2 conversion

Proposed mechanisms to describe the photochemical green-to-red conversion of PCFPs were studied by analyzing crystal structures of intermediates formed during the chemical reaction in dendra2-like fluorophores, EosFP and Kaede. The imidazole side chain of His^{62} in the chromophore triad together with a neighboring Glu^{212} residue have been found to be essential for conversion, since mutations for His^{62} were seen to completely abolish the photoconversion ability [117]. Also, replacement of Glu^{212} by Gln resulted in complete loss of photoconversion [118] [119], implying the role of Glu^{212} anionic form in the fluorochrome conversion process.

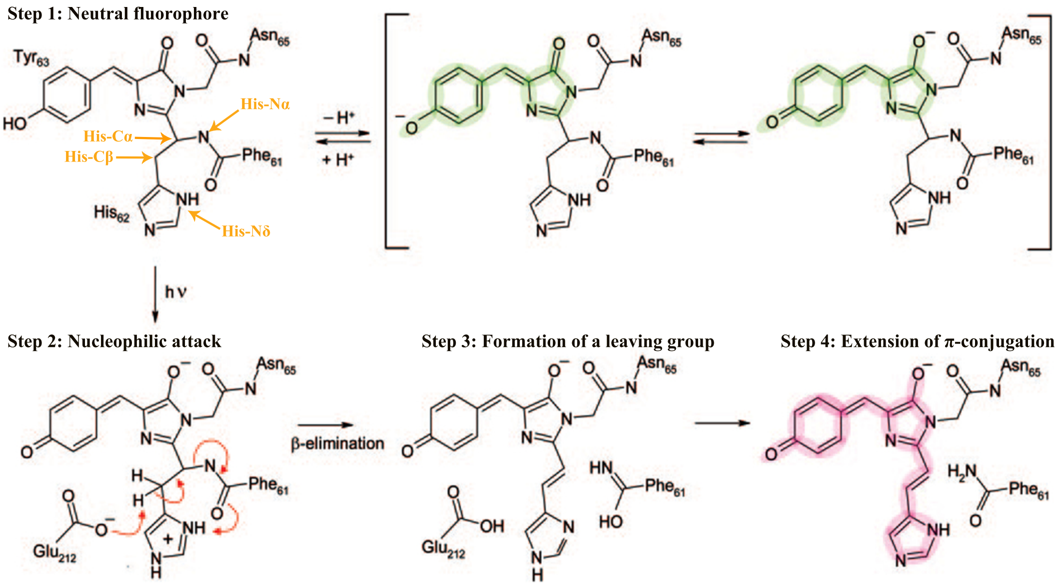

Figure 1.15: Reaction mechanism of light induced green-to-red photoconversion by chromophore extension and backbone cleavage. Modified from [117].

Dendra2 green state (neutral chromophore) upon excitation with 405 nm light, triggers an internal charge redistribution which assists in an elimination reaction [120], to facilitate ultimate cleavage of the backbone between the Nα and Cα atoms of His^{62}. The neutral form of the green chromophore, having a protonated Tyr^{63} phenyl side chain (step 1 in figure 1.15) is the gateway structure for initialization of electronic re-arrangement [117]. Glu^{212} in its anionic form functions as a base to attack one of the two His^{62}-Cβ protons, leaving one unstable proton on the His^{62}-Cβ. This available proton is then transferred to the His^{62} imidazole ring, which is further hydrogen-bonded via its Nδ-H to Phe^{61} carbonyl in both green and red forms. An additional proton on Nϵ increases the tendency of Nδ to donate its proton to the Phe^{61} carbonyl, leading to the formation of a carboximide leaving group in the elimination reaction. Following backbone cleavage, the imidazole tautomerizes to reform H-bond between its Nδ and carbonyl group of Phe^{61}. Concomitantly, a double bond forms between its His^{62}-Cα and C-β atoms, so that the chromophore π-conjugation is extended to the histidine imidazole ring via an all-trans ethenylene moiety. The new chromophore, 2-[(1E)-2-(5-imidazolyl) ethenyl]-4-(p-hydroxybenzylidene)-5-imi-dazolinone, emits fluorescence in the orange-to-red region of the visible light spectrum.

1.5 Motivation and aim of this work

Cell migration is a cyclical process, fundamental to several biological processes. Some are regular events such as skin renewal, embryo development and wound healing. Others are migration abnormalities such as cancer metastasis. It is therefore of interest to understand the underlying mechanisms that directly or indirectly regulates cellular motility. Rapid cell migration requires fast responses to migration stimuli, which means speedy cytoskeletal and focal adhesion reorganization. This demands quick assembly and release of stress fiber and focal adhesion components. In addition, turnover of components is essential to maintain a steady cytoskeletal fiber length and constant focal adhesion integrity. Considering the importance of continous formation and distruction of microfilamens and focal adhesion network in cell migration, dynamics of their constituent molecules was studied in this work. Also, directional cell motility requires presence of a streering mechanism and functional asymmetry between cell's front and rear. One out of many involved asymmetries are the spatially separated different actomyosin stress fiber types, with dorsal fibers located mainly at cell front, transverse arcs in the lamella region and ventral stress fibers at cell rear. Recent studies have identified stress fibers as unstable structures, which are under constant turnover. Fluorescence recovery after photobleaching (FRAP) analysis in motile cell models have shown continuous actin and myosin turnover in these structures [63].

Although the mechanisms of stress fiber assembly and underlying regulatory processes are relatively well understood, little is known about what follows after actomyosin network assembly. Dynamic nature of actomyosin stress fibers has been identified in some cell types by photobleaching only small SF areas, however the overall working of microfilament turnover still remains unknown. In this work, localized fluorescence labelling of stress fibers using dendra2 photoconversion signal as a tracking probe, a global view over stress fiber component turnover was obtained. Main idea was to explore the following:

- Identifying the modes of actin turnover in stress fibers.
- Characterizing turnover differences of spatially separated SFs in migrating cell model. Here, the main concern was to identify different SF types for ongoing actin turnover.

Additionally, myosin motors are known to regulate cell stress fiber contractions in migrating cells, especially at rear. Stress fiber contractions occur as a consequence of myosin displacement on actin filaments. Mechanisms of myosin assembly into stress fiber bundles and its role in mediating contractions is well established, however the intra-bundle myosin movements are not yet explored. Also, rear edge retraction has been found to be the migration speed limiting factor [121], but the role of force generating myosins in regulating cell migration rate remains unidentified. Considering these questions, following ideas were framed:

- Identifying intra-SF myosin dynamics in stress fibers.
- Establishing the role of stress fiber myosin dynamics in controlling cell migration.

Further, attachment of actin fibers to focal adhesions via vinculin adaptor molecule is known to be crutial for mechanotransduction, i.e. to transmit internal forces to the underlying substrate. Similar to stress fibers, multi-protein focal adhesion complexes have also been identified to undergo constant remodelling, where the bound FA contents are under continuous exchange with unbound counterparts [38]. Unlike majority of adhesions, those at cell rear are not stationary. Inward sliding of disassembling adhesions at cell rear is thought to occur due to rapid disassembly of trans-membrane integrins at distal FA tips, followed by re-assembly at proximal tips [107]. However, what happens to FA plaque proteins during the sliding process is not known. In this work, nascent (at cell front), mature (in lamella) and disassembling (at cell rear) adhesions were analyzed to accomplish the following goals:

- Characterizing turnover of focal adhesion plaque components (intra-cellular side) during adhesion formation-maturation-disassembly cycle.

CHAPTER 2

Materials and methods

2.1 List of materials

List of basic laboratory materials and instruments used in this work are presented in the following tables. The details of other specific reagents used will be mentioned in consequent sections.

2.1.1 Disposable materials

Materials	**Supplier**
Aspiration pipettes (5 ml , 10 ml)	VWR
Cell culture dishes with 18 mm hole (diameter: 35 mm)	Cell EG
Cell culture flasks (25 cm^2, 75 cm^2)	VWR
Cryogenic freezing vials	VWR
Eppendorf tubes (0.2 ml, 0.5 ml, 1.5 ml, 2.0 ml)	Eppendorf
Falcon tubes (15 ml, 50 ml)	BD Biosciences
Glass coverslips (thickness: 170 μm)	Menzel Gläser
Glass Pasteur pipettes	VWR
Latex Gloves	Meditrade
Pipette tips (1-10 μl, 2-200 μl, 50-1000 μl)	Eppendorf
Sylgard-184 silicon elastomer kit	Dow Corning

Table 2.1: List of disposable materials used with supplier details.

2.1.2 Instruments

Instrument	Supplier
Centrifuge 5415R	Eppendorf
FluoArc fluorescent lamp	Carl Zeiss
Microscope Incubator XL 2	Carl Zeiss
Laser scanning microscope, LSM 880 with AiryScan detector system	Carl Zeiss
Sterile work bench Hera Safe	Heraeus/Kendro
Thermo-Forma Steri-Cycle CO_2 incubator	ThermoFisher Scientific
Vacuum desiccator	DURAN Group GmbH, Wertheim
Vortex REAX top	Heidolph
Waterbath WB22	Memmert

Table 2.2: List of instruments utilized with supplier details.

2.2 Cell culture and motility induction

Primary human epidermal keratinocytes (nHEKs) from neonatal foreskin were purchased from Cellsystems and cultured in complete keratinocytes growth medium containing 5% Penstrep at 37°C and 5% CO_2. For subculturing and subsequent experiments cells were harvested using 0.02 mL/cm^2 Tryp Kit (0.05% /0.02% Trypsin/EDTA) and 0.02 mL/cm^2 Trypsin Neutralizing Solution.

Preparation of glass bottom culture dishes

For keratinocyte cultivation on glass substrates which would permit microscopy, hollow plastic culture dishes having an outer diameter of 35 mm and inner diameter of 18 mm were glued to microscopy precision cover glasses (thickness: 170 ± 5 μm) using Sylgard-184 silicone elastomer kit, with base to curing agent mass ratio of 10:1. The elastomeric compound was mixed thoroughly and degassed for several minutes using a vacuum pump prior to its application to the glass cover slips. After application of degassed mixture to coverslips, they were glued to the outside of plastic dishes and were heated at 60°C for at least three hours.

Morphology and motility characteristics of these cells varied with increasing passage number, with P0 to P4 displaying a perfectly polarized cell shape and prominent differences between its front and rear. In P5 and higher passage cells, the morphology observed was more symmetrical and rounded and displayed a reduced motility. Therefore, cells between passage 2 to 4 were used for experiments. For all experiments 20,000-30,000 keratinocytes were plated into 170 μm thin-glass bottom petri dishes made in-house, 1-2 days before transfection. Before use, petri dishes were coated with 2.5 μg/cm^2 human plasma fibronectin, in Ca^{2+} - Mg^{2+} free PBS for 30 min at 37°C. To induce cell motility keratinocytes were incubated with 50 nM human epidermal growth factor (EGF, Sigma) at least for 1 h before microscopy.

Materials	**Supplier**
Primary human epidermal keratinocytes	Cell Systems, Germany
DermaLife Medium K complete kit	Cell Systems, Germany
Penstrep	Sigma
TrypKit and Trypsin Neutralization Solution (Ca^{2+} - Mg^{2+} free PBS)	Cell Systems, Germany
Fibronectin (human derived)	BD, Biosciences, USA
Human epidermal growth factor	Sigma

Table 2.3: List of materials used in cell culture and maintenance with supplier details.

2.3 Transient transfections

Transient transfections were performed using ’Transit’ Keratinocyte Transfection Reagent (Mirus, VWR, Darmstadt, Germany). Transit reagent was stored at 4°C and was vortexed well before every use. A mixture of 45 μl culture medium + 1 μg plasmid DNA + 3 μl Transit was prepared in a 1.5 ml Eppendorf tube and incubated for 25-30 minutes at room temperature. Additional 450 μl of culture medium was added to the tube and entire volume of mixture was added to the cell culture dish, followed by an incubation of 2 hours at normal growth conditions. Finally, 1 ml of culture medium was added to the dish, without discarding its contents and was left overnight at 37°C. The next day, cells were stimulated for motility after gentle washing with Ca^{2+} - Mg^{2+} free PBS.

Plasmid	Vector	Provider
Dendra2-vinculin-N-21	Dendra2-N1	Gift from Dr. Michael Davidson, Florida, USA
Dendra2-myosinIIa-C-18	Dendra2-C1	Gift from Dr. Michael Davidson, Florida, USA
Dendra2-C-β-actin	p-Dendra2-C	Gift from Dr. Thomas Friedman, Maryland, USA

Table 2.4: List of plasmids used for transient transfections with provider details.

2.4 Fluorescence light microscopy

The revolution in the field of cell biology came with development and advancements to the light microscopy techniques. It was in early 1900s, when the concept of fluorescence microscopy was brought into practice, with a possibility of specifically labelling different sub-cellular components with fluorophores. Upon illumination of a fluorophore with specific light energy (λ_{ex}), electrons from ground state orbital gets excited to a higher energy orbital. The consequent return of this excited state electron to its ground level occurs rapidly by emission of a lower energy (λ_{em}) photon. These emitted photons can be detected, providing information about localization of the fluorophore within the sample. This phenomenon of rapid photon emission is called fluorescence, with typical emission rates of 108 sec^{-1} and typical lifetime values of 10 ns.

Fluorescence microscopes are designed with an epifluorescence illumination, where light of excitation wavelength passes through the objective lens and illuminates the sample. Most of this excitation light is transmitted through the specimen and only some of the reflected excitatory light and emitted fluorescent light reaches back to the objective. A dichroic mirror is then used to separate the two light waves, by reflecting away the excitation light and transmitting only the emitted fluorescent light to the eyepiece or detector. During epifluorescence illumination, a large portion of specimen is illuminated and thus, increases loss of fluorescence by photobleaching. Additionally, susceptibility to phototoxicity is another risk associated with epifluorescence illumination, which arises due to the free radicals produced during imaging of live specimens.

2.4.1 Laser scanning confocal microscopy

Confocal laser scanning microscopy (CLSM) offers several advantages over conventional wide-field microscopy systems. These includes the ability to control the depth of focus, reduction of background information away from the focal plane (which usually causes image degradation) and possibility to gather optical sections in thick samples. The depth of focus in a confocal microscope is controlled by the geometry of specimen illumination. Figure 2.1 shows a schematic representation of the geometries of specimen illumination in a widefield and a confocal microscope. Compared to a wide cone of illumination over a larger sample volume in a widefield microscope (figure 2.1-A), a confocal system uses a laser illumination focused by a lens system to a very small spot at the focal plane (figure 2.1-B). The tightly focused excitation light spot is used to illuminate an optical section (0.5 to 1.5 μm) in a thick specimen. In laser scanning confocal microscope, the image of an extended specimen is generated by scanning this focused beam across the field of view in a raster pattern controlled by two oscillating mirrors (for x-y movement of the focused beam).

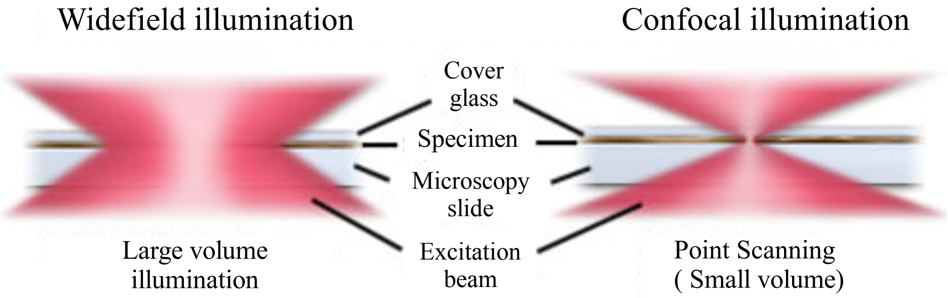

Figure 2.1: Widefield versus confocal illumination of specimen through an objective lens of same numerical aperture. Modified from [122].

The key principle behind confocal microscopy lies in the use of a spatial pinhole, which blocks any out-of-focus emission light. Only the emission light from the specimen focal plane is fed to the detection system through a tiny aperture, called the detection pinhole. The pinhole therefore acts as a physical barrier to the emission light coming from the out of focus planes. Figure 2.2 displays a typical confocal laser scanning system. As the excitation laser beam illuminates the defined focal plane of the specimen, emitted light then collected by the objective lens and gets transmitted via a beam splitter towards the detector. First object in the detection system is the pinhole, which allows light rays only from the conjugated focal spot (hence the term 'confocal') to proceed to the detector. The image information collected is therefore restricted to a defined plane, eliminating the complications arising from other remote areas of the specimen. Compared to a widefield microscope, image contrast and definitions are therefore improved in a confocal system, due to the reduction of background fluorescence and improved signal-to-noise ratio.

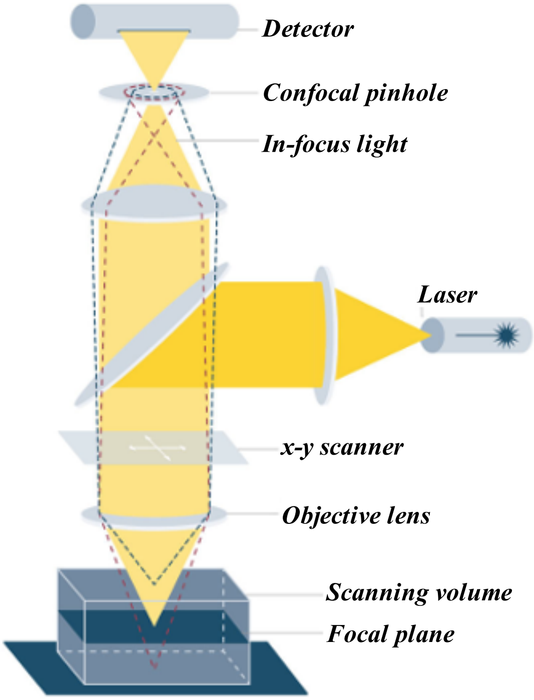

Figure 2.2: A schematic representation of a confocal laser scanning microscope setup. Modified from [123].

2.4.2 AiryScan imaging

In a standard confocal microscope, the out-of-focus light is rejected by the pinhole, the size of which determines the amount of light that will ultimately reach the detector. Theoretically, in order to obtain a sharper image, the confocal pinhole needs to be increasingly closed. In practice, if the detection pinhole gets too small, the light rays passing through it undergoes bending (diffraction) and this unwanted bending of light in turn degrades the resolution of resulting image. Minimizing the detection pinhole size in a confocal microscope therefore costs an irreversible loss of resolution, sensitivity and scanning speed. AiryScan is an enhanced spatial resolution device (available from Carl Zeiss), which deals with this compromise between spatial resolution and the amount of light being collected from the specimen. AiryScan images the specimen onto a concentrically arranged array of 32 individual hexagonal detectors.

These 32 detector elements are small Gallium Arsenide Phosphide (GaAsP) elements, arranged in a compound eye fashion. Each of these detector arrays acts as a small independent pinhole. Emitted light from the specimen passes through an open confocal pinhole onto the AiryScan detectors, enabling the detection of all emitted photons. Signal is captured by individual detector element, each scanning the specimen from different angles and the final image is

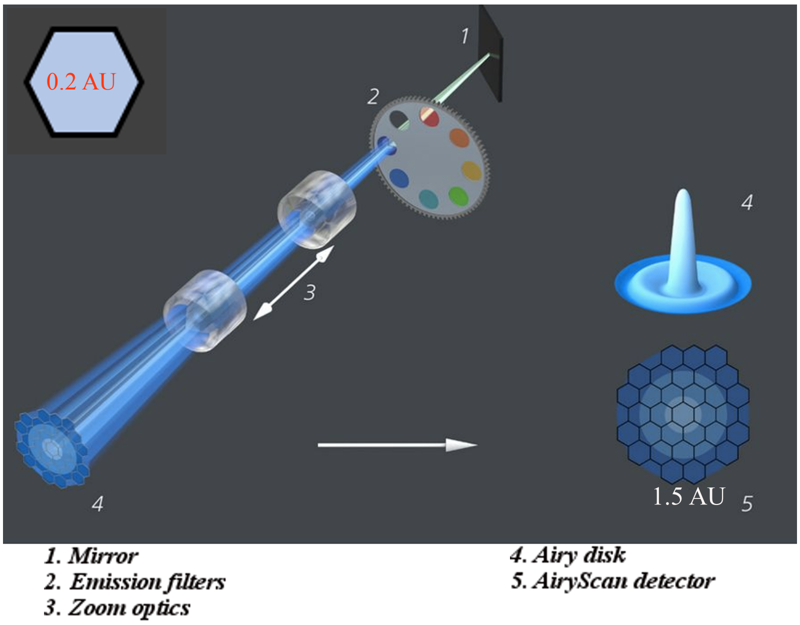

Figure 2.3: Beam path in AiryScan imaging system. The 32 hexagonal sub-airy detector elements are arranged onto a concentric array and acts as a 1.5 AU pinhole. The individual detector element is a 0.2 AU pinhole. Modified from [124].

reconstructed by reassigning detector signals to their correct position. Since image acquisition takes place with constantly open pinholes, no photons are lost in the detection process. Individual sub-airy detector element is a pinhole of 0.2 AU and collectively (32 elements together) they collect emission the light as a 1.5 AU pinhole, thus providing a larger signal-to-noise ratio.

Additional Fast AiryScan mode uses the area detectors to image with a high speed. The light beam is elongated in y, such that four sub-airy units are illuminated together (figure 2.4). The AiryScan detector array is then scanned with a horizontal scanner movement. At a given point of time, four detector elements are scanned instead of one. This parallelization of therefore gives a high scanning speed and sensitivity.

AiryScan processing

Once images are acquired using AiryScan, a processing routine is used to reconstruct the output image. AiryScan processing is based on compiling raw images collected by 32 individual GaAsP detector elements and performing deconvolution to refine the final image. The central detector element lies on the optical axis and creates a confocal pinhole of its own. The other small detector elements are displaced against the optical axis. The point emitter (in the specimen) being imaged, is therefore be imaged from different phases. As a consequence, single recorded images are spatially displaced against each other. Since, the amount of displacement

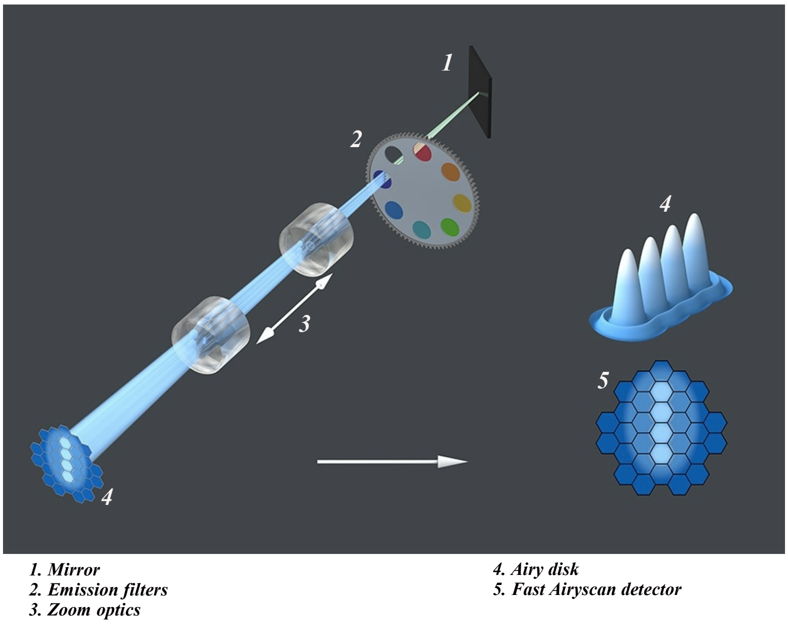

Figure 2.4: Beam path in a AiryScan imaging system in the Fast AiryScan mode. Four vertical detector elements indicated in 5, are scanned in parallel. Modified from [124].

of each detector element is already known, the measured detection points are then reassigned to their correct position by an appropriate shift, summing up all individual images to obtain an image with improved signal-to-noise ratio (SNR) and resolution in the lateral plane. Since each detector element works as a separate pinhole with its own point spread function (PSF), the detected images or PSFs are treated individually. The detection PSF from each detector element is multiplied individually with the illumination PSF to obtain an effective PSF of each element. By properly compiling the contribution of each detector element and combining their different PSFs using linear deconvolution, the contribution of each element becomes significant to the overall image signal.

2.5 Imaging and photoconversion parameters

Live-cell confocal imaging was performed on transiently transfected single migrating keratinocytes using LSM 880 Indimo, Axio observer (Carl Zeiss), equipped with an incubator to maintain physiological conditions during imaging of cultured cell samples at 37°C and 5% CO_2. Time lapse images were acquired using a 40x/1.3 NA DIC Plan-Neofluar oil objective (Carl Zeiss) and Zen 2.1 SP2 (Black) 64-bit Software. Detection of dendra2 primary and photoconverted states was done using the Gallium Arsenide Phosphide (GaAsP) photo-detector. For dendra2 primary state excitation, argon ion laser of 488 nm wavelength was used and for photoconverted dendra2 excitation, the 561 nm HeNe laser was used. Dendra2 photoconversion was carried out using a combination of time series, regions and bleaching tabs available in the LSM software. Regions tab was used to specify the photoconversion region of interest (ROI), using the available rectangle tool and bleaching tab settings enabled specific near UV (405 nm) exposure within the specified ROI. Table 2.5 lists the acquisition parameters used to image native and photoconverted dendra2 forms.

Parameter	**Details**
Scaling per pixel	0.16 μm x 0.16 μm
Scan mode	Frame
Pixel dwell	1.54 μs
Frame time	9.28 sec
Scan direction	Unidirectional
Averaging	2
Pinhole size	1 AU
Beam Splitters	MBS: 488/561 MBS: 405 (for invisible light)
Excitation lasers	488 nm: 1.0 % (for native Dendra2) 561 nm: 1.6-1.9 % (for photo-converted Dendra2)
Detection wavelength bandpass filters	495-550 nm (native Dendra2) 570-695 nm (photo-converted Dendra2)

Table 2.5: Confocal acquisition parameters used for imaging native and photo-converted dendra2 fusion proteins.

Dendra2 photoconversion was performed within the pre-defined region of interest in the cell, by exposing specific cell area to 405 nm light. A rectangle shape was selected from the available regions tab in the Zen 2.1 software. A rectangular region of interest (ROI) was then manually placed onto one half of the cell area. Using the bleaching tab available in the software, UV exposure parameters were adjusted. After 5 pre-conversion scans (using parameters listed in table 2.6), 8% exposure of 405 nm light was used to photo-convert dendra2 within the ROI. Post-conversion frames were then acquired in a time-lapse sequence with parameters same as pre-conversion imaging.

High resolution imaging for focal adhesions was performed using the Fast AiryScan mode on Zeiss LSM 880. Using the 0.2 AU AiryScan detector elements, an improved spatial resolution of focal adhesion dynamics was obtained. And the feature of simultaneous faster scanning in the fast mode enabled a scan time of 1 sec per frame and a pixel dwell time of 0.90 μs.

Parameter	**Details**
Scaling per pixel	0.09 μm x 0.09 μm
Scan mode	Line sequential
Pixel dwell	0.09 μs
Frame time	1.09 s
Scan direction	Unidirectional
Averaging	2
Excitation lasers	488 nm: 0.60 % (for native Dendra2) 561 nm: 0.95 % (for photo-converted Dendra2)

Table 2.6: AiryScan acquisition parameters used for imaging native and photo-converted dendra2 fusion proteins.

Advantages of using photoconversion over other methods to study real-time dynamics With increasing understanding in the field of cell biology research, more attention has been given to the study of sub-cellular structural dynamics and molecular transport. Attempts have been made to study the molecular dynamics of cell cytoskeleton including actin filaments and microtubules as well as focal adhesions, employing the widely used method of fluorescence recovery after photo-bleaching (FRAP) to examine structural turnover and molecular mobility. FRAP uses a high intensity laser beam on living samples, to erase fluorescence in a specified region of interest. Fluorescence recovery of this region then provides information on intra-cellular mobility of the target molecule. However, only a restricted sub-cellular region is analyzed using this technique with an involved risk of phototoxicity due to high intensity light exposure. Speckle microscopy [125] is yet another method used in molecular dynamics studies, where substantially lower concentration of fluorescently labelled target molecules are expressed, such that small number of labelled molecules gets randomly incorporated with large number of unlabeled ones into a macromolecular structure. The fluorescent molecule incorporation therefore creates non-uniform intensity patterns, which enables visualization of their mobility and turnover against a low background fluorescence. Favorable application of speckle microscopy is however dependent upon reliability to appropriately image small fluorescence patterns, which usually exhibits weak emission signals and therefore yields low signal-to-noise ratios. Unlike these methods, our setup holds an advantage of localized molecular labelling, which enables location specific tagging of molecules on a sub-cellular level, followed by easy chasing of newly tagged molecules against a dark background. This offers a better contrast, improved signal-to-noise ratio and ultimately an enhanced overall ability to trace molecular movement in time-resolved imaging. Moreover, since both native and photoconverted forms of dendra2 are spectrally separated and are visualized using different channel settings under a microscope using two commonly available excitation laser beams of 488 nm and 561 nm respectively, it holds greater practical advantages. Additionally, the post-conversion red fluorescent form appears against a dark background providing a global overview of the fate of target molecules, which is not possible with standard FRAP or speckle methods.

2.6 Fiber tracking for stress fiber analysis

Stress fibers in motile keratinocytes undergo continuous remodeling and shape alterations in accordance to cell translocation. This complicates their real time identification and analysis. There is therefore a need to reliably detect discrete stress fiber structures in an image sequence and track their displacements and changes in shape. In order to analyze stress fibers in migrating cells, an automated python based fiber tracking software was designed by our collaborating partners, Dmytro Kotsur and Dr. Julian Mattes at *Software Competence Center Hagenberg (SCCH), Austria* [126]. The input image at each time step was subjected to a series of modification steps (figure 2.5) in order to minimize the noise and enhance image details. Table 2.7 presents the details of image processing steps involved in the de-noising step.

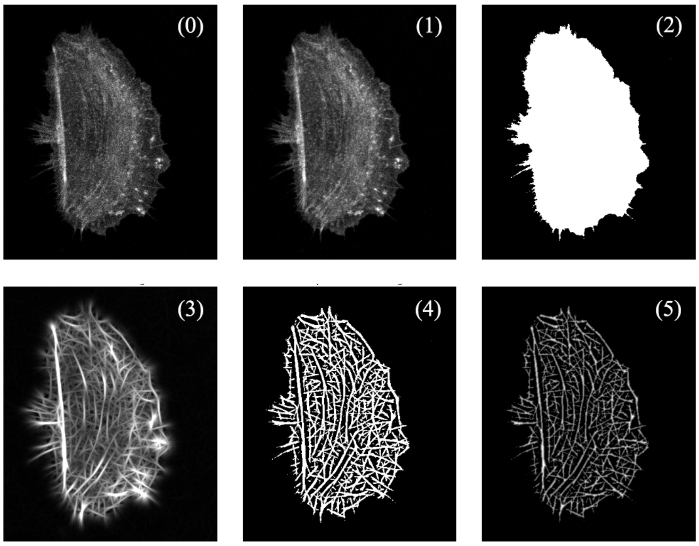

Figure 2.5: Image processing steps employed for de-noising and enhancement of image details: (0) Input image, (1) Bilateral filtering, (2) Gabor filtering, (3) Otsu's thresholding, (4) Adaptive thersholding and (5) Distance transform. Figure contribution by Dmytro Kotsur, SCCH.

Step	Modification filter	Description
1	Bilateral filtering	Image noise reduction/suppression (figure 2.5, Step 1) using bilateral filter [127].
2	Otsu's threshold	Global Otsu's threshold [128] based on the de-noised image from the previous step was computed. This threshold value was used to produce the binary image. Some artifacts of the binary image (holes and segments with small-area, which might correspond to the remaining noise) were removed using morphological opening and closing ([129], page 657). The binary region with the largest area was assigned to be the mask of the whole cell (figure 2.5, Step 2).
3	Gabor filter	The contrast of the de-noised image from step (1) was enhanced using the maximum response of a Gabor filter bank (with the scale parameters: $\sigma \epsilon$ 8,10,12,15; angle parameter: $\alpha = \pi i/16$, i= 0,..,15). Then the dynamic range of the image was extended by the factor of 3.0 (figure 2.5, Step 3).
4	Adaptive thresholding	At this step, a binary image based on the enhanced image from Step (2) was computed using local adaptive threshold ([129], page 780) with the parameter 'block size' of 25 pixels. The resulting binary mask was restricted according to the cell mask from Step (1).
5	Distance transform	The distance transform [130] based on the binary mask from Step (3) was computed. The result of this step was used to compute the gradient vector flow in the snake algorithm described in [131].

Table 2.7: Steps employed in image modification for minimizing the noise and enhancing image details.

Tracking of individual fiber is based on a mathematical algorithm which needs manual initialization of target stress fiber on an initial time frame of the image sequence. Target stress fiber is labelled with a contour which automatically finds and transfers the labelled fiber to the next frame of the sequence using optical flow. The steps of de-noising and sharpening are then re-applied on subsequent frames. Figure 2.6 represents workflow of the algorithm which is applied one-by-one to each image in the time lapse sequence.

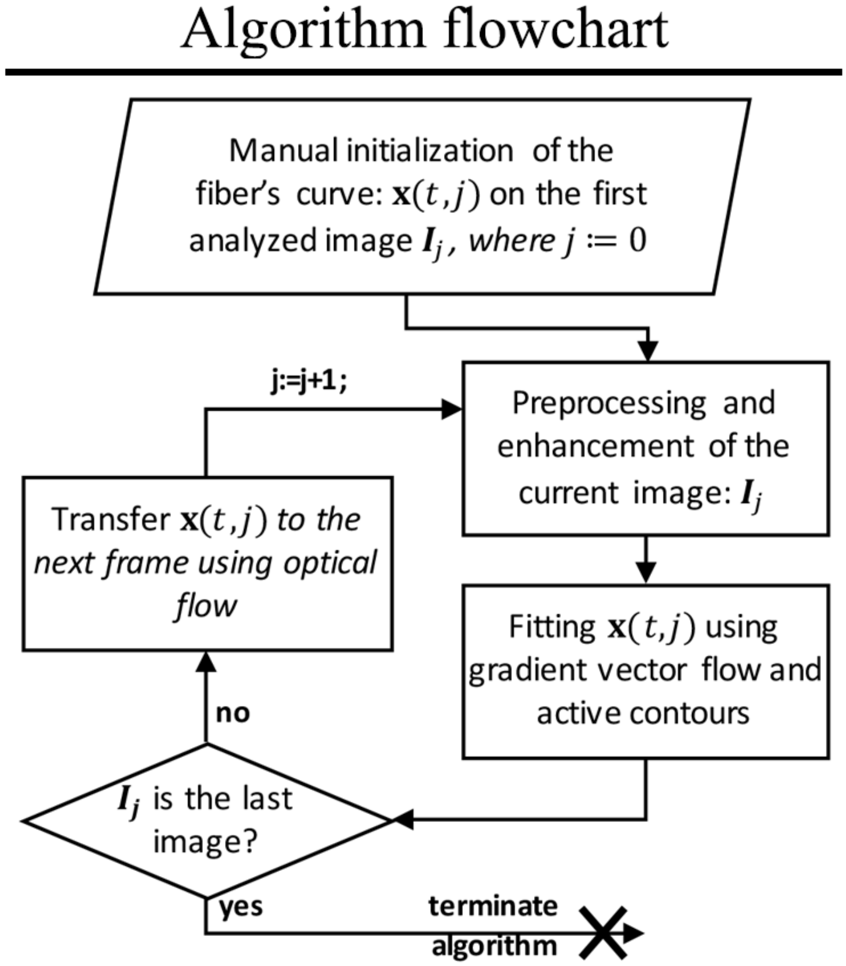

Figure 2.6: Schematic representation of overall flow of the contour tracking algorithm. Figure contribution by Dmytro Kotsur, SCCH [126].

Once all image modification steps and tracking algorithm are applied to every frame, the trajectory of overtime displacements of labelled contour is obtained. An example of tracked transverse arcs in migrating keratinocytes (nHEK) is presented in figure 2.7, by a red contour.

Along with image-to-image tracking of stress fibers, the labelled fiber contour quantifies also the real-time fiber intensity values. In order to determine the turnover dynamics of actin and myosin in stress fibers, tracking tool was implemented to first track different stress fibers in migrating keratinocytes and finally quantify over time intensity changes in post-photoconversion time frames.

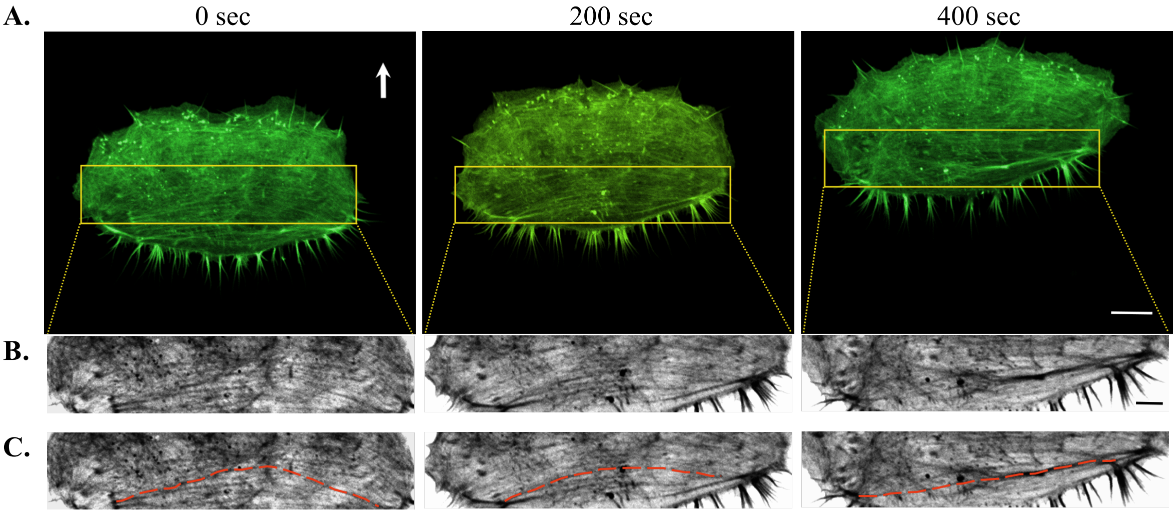

Figure 2.7: Representation of stress fiber tracking in migrating keratinocytes, using fiber tracking tool. (A) GFP-Lifeact transfected nHEK, displaying the actin cytoskeletal network. White arrow points in the direction of migration. Scale bar = 10 μm. (B) Magnified view of actin arcs in the central cell region. Scale bar = 5 μm. (C) Dashed red line represents the tracked stress fiber using fiber tracking tool.

2.6.1 Intensity normalization

The obtained intensity values from entire image sequence were normalized. Quantified original intensities were rescaled to the range [0,1]. Minimum (I_{min}) and maximum (I_{max}) intensity values were determined for entire image sequence (separately for green and red channels). Rescaling was performed for each image using the following formula:

$$I_{new}(x,y) = \frac{(I_{old} - I_{min})}{(I_{max} - I_{min})}$$

Where, I_{new}: new intensity value at pixel (x,y) and I_{old}: old intensity value at pixel (x,y).

Normalization example:

Calculate minimum and maximum intensity value for the entire image sequence in figure 2.8.

I_{min} = min (0,0,1,2) = 0

I_{max} = max (65000, 64500, 63400, 62000) = 65000

The rescaling formula will be :

$$I_{new}(x,y) = \frac{(I_{old}(x,y) - 0)}{(65000 - 0)} = \frac{(I_{old}(x,y) - 0)}{65000}$$

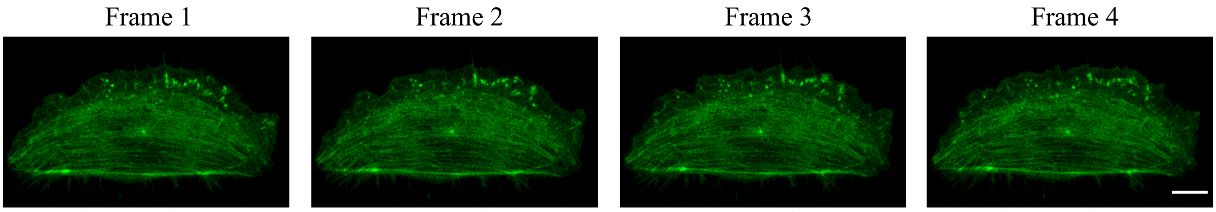

Frame 1 | Min Intensity: 0 | Max Intensity: 65000

Frame 2 | Min Intensity: 0 | Max Intensity: 64500

Frame 3 | Min Intensity: 1 | Max Intensity: 63400

Frame 4 | Min Intensity: 2 | Max Intensity: 62000

Figure 2.8: Min-max normalization implemented in the fiber tracking tool used to rescale intensities in the range [0,1]. Scale bar = 10 μm

2.6.2 Kymographic representation of stress fibers

To precisely compute actin and myosin molecular dynamics in stress fibers, another python based image processing routine (developed by *Software Competence Center Hagenberg, Austria*) was designed. This tool utilized the pre-tracked trajectories of the target stress fiber from fiber tracking tool to generate an intensity kymograph of the fiber itself, along with its local neighborhood areas. Since in most cases the fiber is not a perfectly straight structure but rather a bent curve, its shape was normalized to a straight line. The fiber curve itself and its neighborhood was transformed employing the following steps:

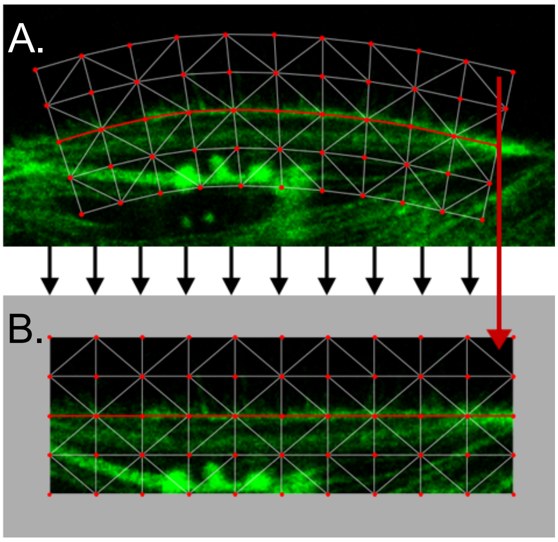

Figure 2.9: (A) The neighborhood of the tracked fiber is normalized to a rectangular shape (B). The red curve shows the position of the fiber before and after transformation, the red points are corresponding landmarks and the red arrow illustrates affine transformation of the corresponding triangles.

- Several equidistant offset curves of the main fiber's curve (Figure 2.9 A, red curve) were constructed in both directions.
- The landmark points were sampled along the fiber's curve and its offset curves. (Figure 2.9 A, red points).
- Corresponding landmark points for the normalized shape were computed, such that the fiber's curve and its offset curves are represented by parallel lines (see Figure 2.9 B, red points) preserving the original length of the fiber.
- The landmark points on the original image were triangulated and image regions inside the triangles were transformed to corresponding triangular regions based on the normalized landmark points.

Above steps were applied to every image of the time-lapse sequence in which the tracked stress fiber curve was present. Finally, the normalized images were vertically stacked in order to represent the fiber intensity profile in the form of a kymograph.

2.7 Linear regression analysis by least squares method

Linear regression is a linear approach to modelling the relationship between two variables by fitting a linear equation to the observed data. One out of two variables is considered to be an explanatory or independent variable and other as a dependent variable. A scatter plot is used as a pre-determining tool to test the strength of the relationship between the two variables. A linear regression line has an equation of the form Y = a + bX where, X is the independent variable and Y is the dependent variable. Slope of the line is b and a is the y-intercept. The most common method for fitting a regression line is the least-squares method, which calculates the best-fit line for the observed data by minimizing the sum of squares of the vertical deviations (S_T) from each data point to the line (if a point lies directly on the line, then the vertical deviation is 0). Since deviations are first squared, there are no cancellations between negative and positive values. To evaluate the fit of the regression line to observed data, computed regression line is plotted over the scatter plot. The coefficient of determination (R^2) is then calculated from previously estimated total sum of squares (S_T). R^2 is a measure of the amount of variability in the data accounted by the regression analysis. It can take values between 0 and 1, where 0 indicates failure to establish a linear relationship and 1 indicates a perfectly linear correlation between the two tested variables. Another calculated parameter is the standard error (S_E), which is the measure of accuracy of the linear fit prediction. It is the square root of averaged square deviation. Smaller S_E indicates a more accurate linear fit prediction. The statistical t-tests are used to conduct hypothesis test on the regression coefficient. The p-value for each independent variable tests the null hypothesis which states that the independent variable has no correlation with the dependent variable. If p-value < 0.05, the null hypothesis can be rejected, indicating a linear relationship and a non-zero R^2 value.

In this study, linear regression analysis was used to determine the relationship between myosin IIa dynamics in stress fibers (independent variable) and the speed of cell's migration (dependent variable).

2.8 Statistical analyses

2.8.1 t-test

A t-tests is a type of inferential statistic, that is based on a hypothesis to establish statistical differences between means of two population groups. It is often used to test if two samples are statistically different from each other and tests if the difference could have happened by chance. It is applied to data sets with normal distribution and compares the average values of two data sets. T-test requires three key data values, which include the difference between mean values from each data set, standard deviation of each group and number of data values of each group. T-test takes a sample from each of the two sets and establishes the problem statement by assuming a null hypothesis, that the two means are equal. Based on standard equations, certain values such as t-value are calculated and compared against pre-set standard values and the presumed null hypothesis is then accepted or rejected accordingly. If the null hypothesis is rejected, it indicates that the compared data sets are strong and are not by chance.

For the type of data used in this study, where replicates of measurements were used to build up a sample population and experimental groups being compared were measured under similar cellular conditions, paired two-tailed t-test was performed.
Significance levels are given as follows:

$$0.01 \leq p < 0.05 : *$$
$$0.001 \leq p < 0.01 : **$$
$$p < 0.001 : ***$$

2.8.2 ANOVA test

Analysis of variance (ANOVA) is a statistical method used to test differences between multiple means. Unlike t-tests, ANOVA uses comparisons of variances to make inferences about means.

It works on a non-specific null hypothesis that means of all compared groups are equal. When the null hypothesis is rejected, the conclusion is that atleast one of the means in the group is different from atleast one other mean. ANOVA signifies a difference among the compared groups but does not really identifies groups with differences. Therefore, a follow up ANOVA test called Tukey's multiple comparison approach was used to quantify the extent of differences between the compared groups. This test compares the mean of each test group with every other test group. The test takes into account the scatter of all groups. It compares the difference between the means to the amount of scatter quantified using information from all the groups. This gives a precise value for scatter and gives the test more power to detect differences. Tukey's test gives a q-ratio of comparison, calculated by the formula:

$$q = \frac{\sqrt{D}}{SED}$$

where, D is the difference between means and SED is the standard error of that difference. Standard tables are used to determine whether or not a q-value is large enough for a difference to be declared as statistically different. Calculation of q depends on several factors such as number of groups being compared and number of degrees of freedom.

2.9 Processing and tracking of focal adhesions

In order to quantify and analyze the intensity profiles of focal adhesion complexes, we designed a MATLAB based image processing tool to detect and track FAs in an image sequence. Images with dendra2-vinculin staining were analyzed using the green channel as reference to mask discrete adhesions in an image. Thereafter, adhesion tracking algorithm described in Hersch *et al.* [132] was applied to track the pre-masked FAs through the image sequence.

FA detection and analysis

Input images from the time lapse sequence were previously smoothed using a 3-D Gaussian filter with a standard deviation of 0.5. Then the local average filter and local standard deviation for each pixel was determined in a 51 pixel square (pixel size: 0.2 μm). All pixels with a z-score higher than 1.2 were defined as FAs. Detected FAs with a size of less than 20 pixel were discarded. The analysis was performed separately for each time point. Finally the average grey value of each FA at each time point was calculated. To track FAs over time, all FA masks that were connected to each other in consecutive images were labelled as one FA. The change in average grey value intensity was then used for further analysis.

Shown in figure 2.10 is the workflow of adhesion tracking and analysis tool. Every FA aggregate

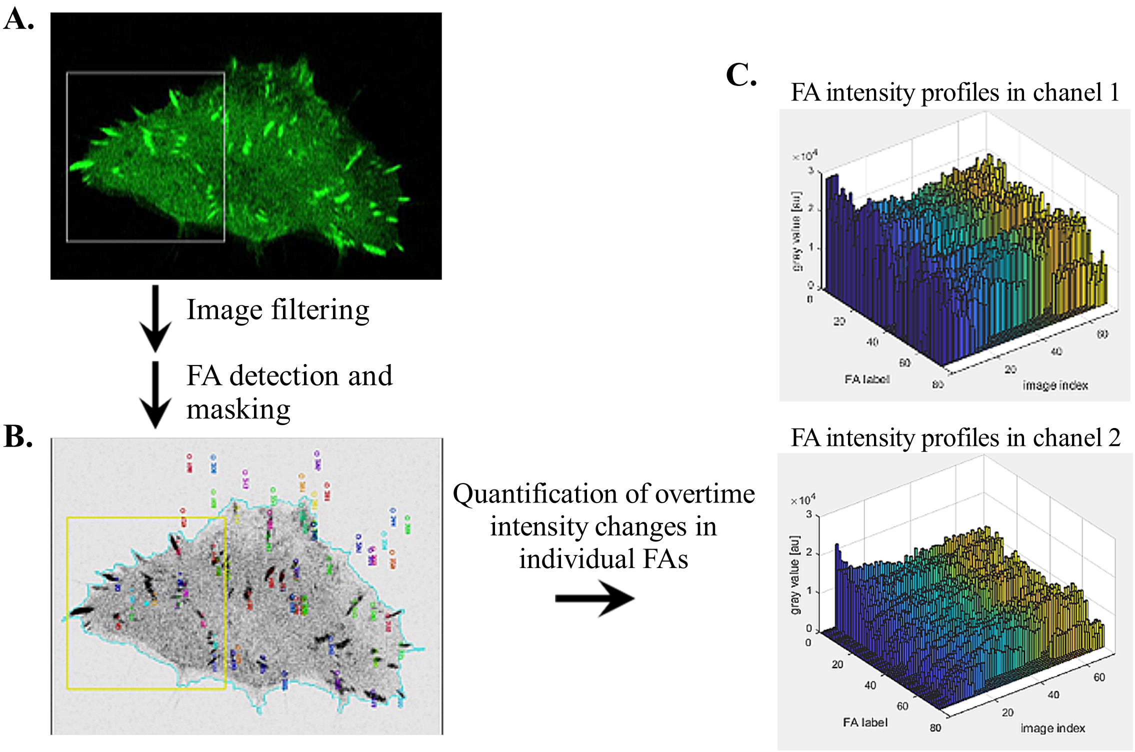

Figure 2.10: Schematic representation of image processing routine used for focal adhesion tracking and intensity quantification. The input image (A) is smoothened and masked for discrete focal adhesion sites (B), to quantify average gray values of individual FA. After applying steps A and B to all images in the image sequence, overtime intensity profiles for each FA site is obtained (C).

in the first input image (using green channel as the reference for FA detection) is named with a unique identity or FA label. The red boundary in sub-figure (B) marks the cell periphery defined from the input image (A) and every colorful spot represents single FA label. Each label is then tracked overtime for associated changes to their size and position. This is done to obtain individual FA masks in the input image of the time lapse sequence. Finally, frame-to-frame extraction of avarage gray values of masked FAs gives their overtime intensity profiles. Quantification of photoconverted vinculin signal within masked FAs is done using the extracted gray values in the red imaging channel.

CHAPTER 3

Results

In this chapter, detailed description of cell migration model systems used in this work, human epidermal keratinocytes (nHEKs) is presented. In order to understand the dynamic behavior of cell migration components, as a preliminary step the standardized cell migration conditions are outlined, with main focus on morphological features of keratinocyte migration. Thereafter, migration associated cytoskeletal and focal adhesion networks in polarized cell system are outlined. Finally, the experimental approach used to analyze real-time dynamics of actomyosin and focal adhesion networks is presented.

3.1 Morphology and traits of keratinocyte migration

In the interest of studying component dynamics in cell migration, primary human epidermal keratinocytes were used as model systems for cell motility analysis. These cells exhibit both, sessile and migratory states. Sessile keratinocytes possess a symmetric and circular morphology

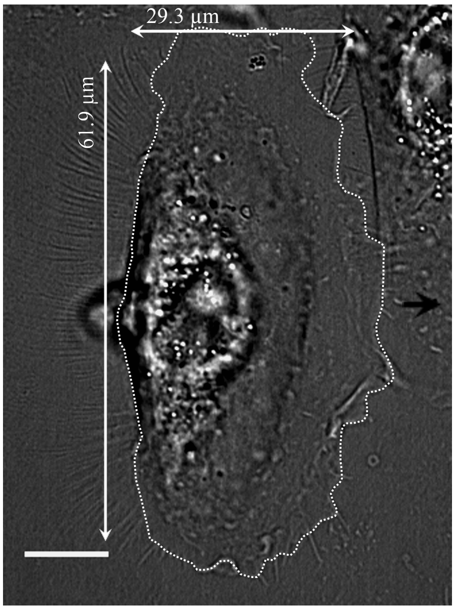

Figure 3.1: A polarized migrating human epidermal keratinocyte with a morphological aspect ratio of 2:1. Dotted line represents the cell boundary and the black arrow points in the direction of cell's migration. Scale bar = 10 μm.

with nucleus occupying the central position. Motile keratinocytes, however, manifests an asymmetric morphology with clear differences between front and rear. These cells showcase a prominently arched front and a flattened rear to acquire an overall crescent cell shape. Normally, a migrating keratinocyte displays a morphological aspect ratio of ~2:1, where the length of major axis is typically twice of that of the minor axis. Shown in figure 3.1 is a phase contrast image of a migrating keratinocyte exhibiting an arched front, which protrudes in the direction of cell's movement and a flat rear cell edge. Together, the long axis of the cell (61.9 μm) and the short axis (29.3 μm) gives an aspect ratio of ~2:1. Frontal part of the cell demonstrates dynamic membrane ruffling forming both, the filopodial as well as lamellipodial protrusions in the direction of migration (figure 3.2). The flat rear cell edge is however non-protrusive and is responsible for translocating the cell body forward. Similar to filopodial membrane spikes at cell front, retraction fibers are found at rear cell's edge as cytosol containing membranous extensions.

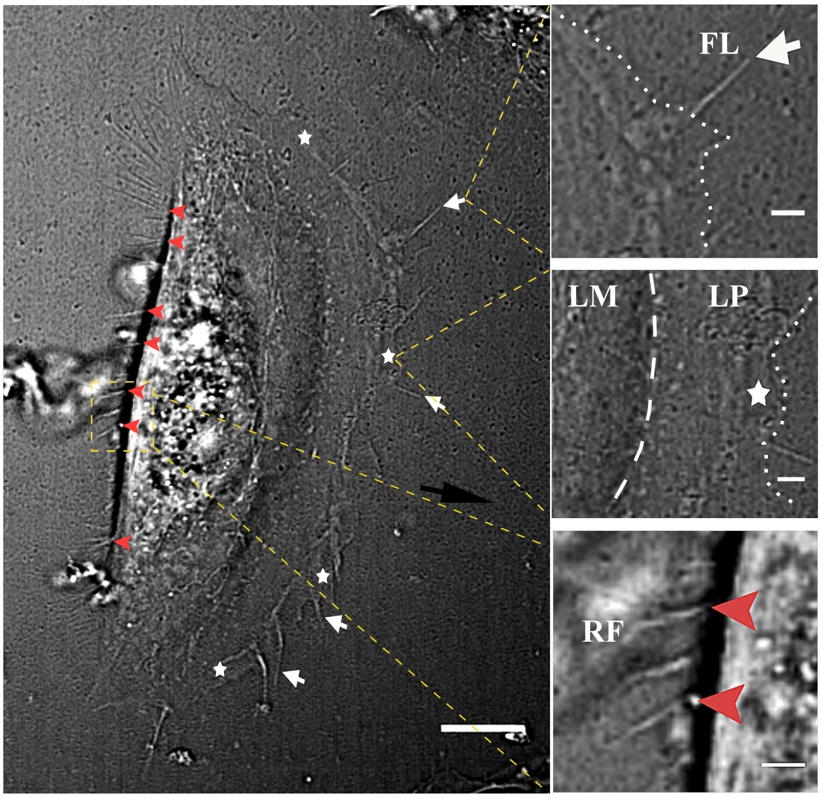

Figure 3.2: Phase contrast image of a locomoting human epidermal keratinocyte. Black arrow points in the direction of migration. White arrows at frontal tips indicates the fillopodial protrusions (FL). The finger-like projection is clearly shown in the magnified inset, where dotted line marks the cell's front boundary. White stars indicate the sheet-like lamellipodium (LP). As seen in the magnified inset, the membranous LP leads the lamella (LM). Retraction fibers (RF) at cell rear are shown by red arrow heads, connected to the rear cell margin. Scale bar of image= 10 μm. Scale bar of insets= 2 μm.

But unlike filopodia, retraction fibers remain attached to the underlying substrate as the cell body retracts. They are attached to the substrate at their distal ends, which are connected at almost right angles to the cell margin at their proximal ends (indicated by red arrow heads in figure 3.2). In motile cells, retraction fibers are known to leave small vesicles containing cellular material at the surface behind the cell, creating a migration trail or footprints and are therefore commonly referred as cellular tails.

Once sessile cells are triggered for migration, they undergo a series of structural and functional re-arrangements [3]. In migrating cells, regulatory factors controlling actin filament polymerization are all concentrated at the lamellipodial region, where they assist in the formation of short filaments and pushes the membrane forward. Keratinocytes when labelled for actin, displays short finger-like filopodial bundles at the protruding front (figure 3.3), followed by a mesh like actin network in the lamellipodial region.

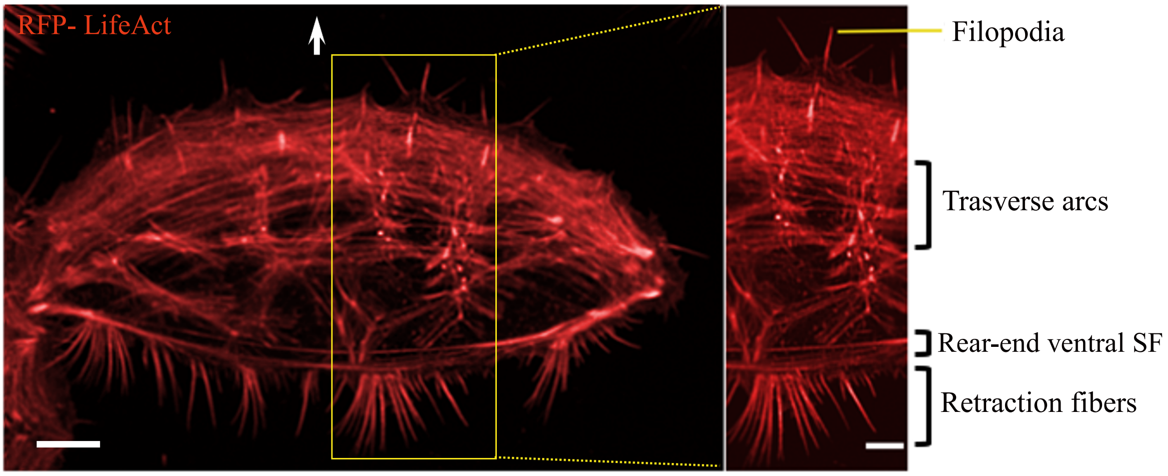

Figure 3.3: Human epidermal keratinocyte labelled for actin. White arrow indicates the direction of cellular movement. The magnified cell area emphasizes different types of actin bundles at different cell locations. Filopodial protrusions at frontal tips appear like pointed projections. Transversal actin arcs are located at cell center and the rear-end stress fiber bundle is aligned parallel to the rear cell edge. Attached to the rear edge are the membranous retraction fibers. Scale bar of image = 10 μm. Scale bar of magnified inset = 5 μm. Image contribution by Galia Sakaeva (ICS-7).

As shown in figure 3.3, out of the three types of stress fiber assemblies (explained in section 1.2.2), mainly two stress fiber types were observed in keratinocytes - (1) The circular transverse arcs (TA) which occurs in the lamella and occupy a central location in the cell body and (2) the elongated, linear rear-end ventral stress fiber (RSF) which is located close to the cell's rear edge. The RSF was always oriented perpendicular to the direction of cell's migration. Dorsal actin fibers are usually fine, short-lived structures and are not clearly visible in this cell type at 40X magnification. Plus, on a functional level, dorsal fibers are non-contractile structures (lacks myosin) and their involvement in mediating cell shape changes in a migrating cell system is minimum. Hence, in this study the analysis was restricted to transverse arcs and the rear-end ventral stress fiber. TAs and RSFs are contractile arrays of actin, cross-linked by myosin II motor proteins. Upon labelling for myosin II (figure 3.4), striated pattern on TAs and RSFs was observed, displaying an alternative bright-dark-bright pattern.

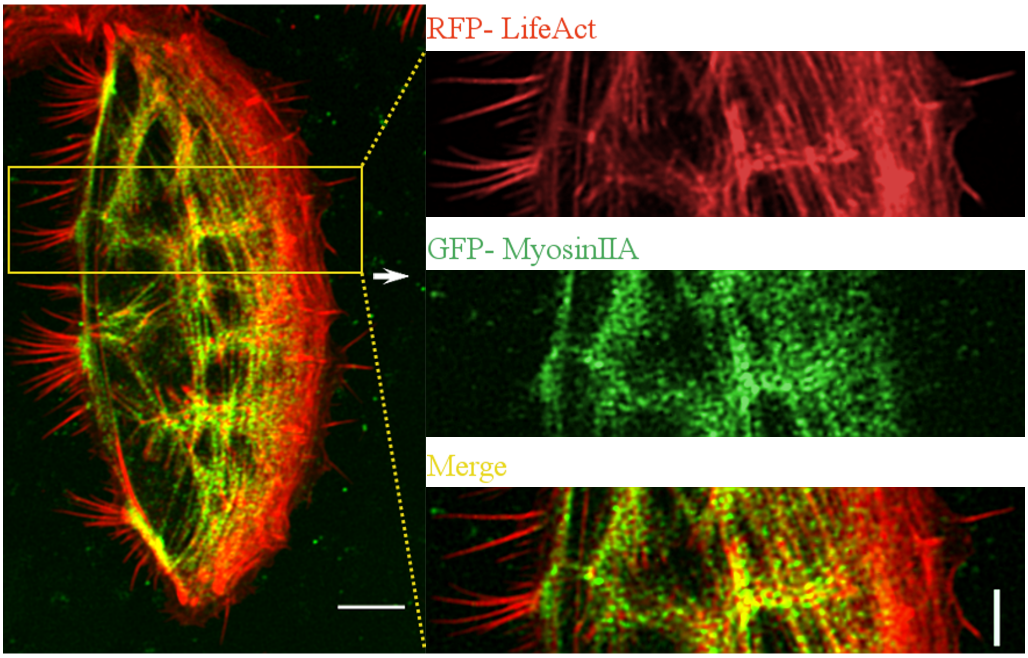

Figure 3.4: Localization of myosin IIA (green) on actin stress fibers (red) in polarized human epithelial keratinocytes. The magnified area (enclosed within the dashed line) highlights co-localization of the two cytoskeletal components in transverse arcs (TAs) and rear-end stress fiber (RSF). Scale bar of image = 10 μm. Scale bar of magnified area = 5 μm. Image contribution by Galia Sakaeva (ICS-7).

Short actin bundles in the anterior lamellipodial region, where fillopodial protrusions are formed, display no myosin II localization. In the posterior lamellipodial region, where short actin filaments are assembled into stress fibers (explained in section 1.2.2), myosin II is seen to decorate the newly formed long actin fibers.

In order to establish their attachment with the underlying substrate, motile keratinocytes assemble multi protein focal adhesion complexes (explained in section 1.3) at the cell-substrate interface. During 2D confocal imaging, FAs are mainly found at the ventral surface of the cell.

These complexes form discrete attachment sites of different sizes and are connected to the actin cytoskeletal network via vinculin adapter molecule. When labelled for vinculin, typically FAs appear as bright aggregates (figure 3.5).

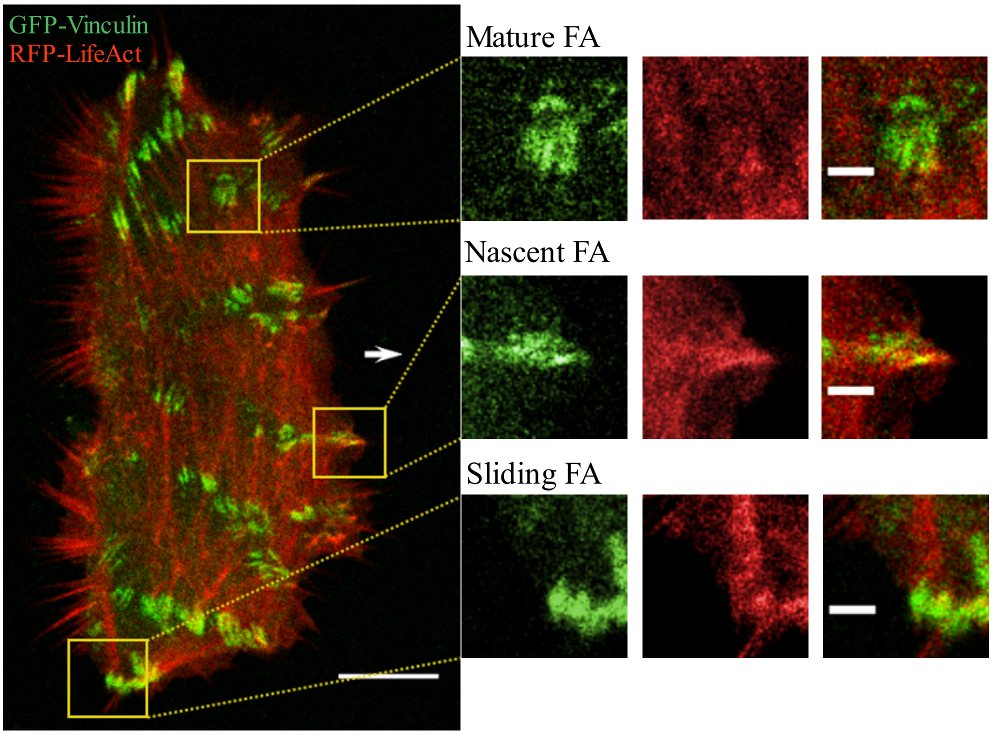

Figure 3.5: Motile keratinocyte labelled for its actin filament network (RFP-LifeAct) and focal adhesions (GFP-vinculin). Scale bar = 10 μm. Different types of focal adhesion complexes are represented in the magnified insets. Scale bar of insets = 2 μm.

Mainly three different types of focal adhesion complexes were observed in keratinocytes. Small and young adhesion complexes, called nascent FAs are located close to the cell periphery. They undergo an over-time increase in their size and are seen to be connected to thin actin filaments (shown in magnified inset in figure 3.5). Stable and larger focal adhesions called mature FAs, were located in the cell body. These FAs display no significant over-time alteration in their size. At the cell rear, sliding FAs were observed to be attached to thick actin filament bundles (figure 3.5). These FAs are seen to undergo inward sliding prior to their disassembly. No or sometimes tiny FAs were spotted in the perinuclear region.

3.2 Experimental approach used to study overtime protein dynamics

In order to study the dynamics of cell migration components, specifically those of microfilament network and focal adhesions, photoconversion properties of dendra2 fluorophore (explained in section 1.4.2) were used. As a first step, this section presents an introduction to standardized features of the experimental setup used to carry out dendra2 photoconversion and subsequent imaging parameters used to visualize the post-conversion form.

3.2.1 Optimizing experimental conditions for dendra2 photoconversion

In order to effectively photo-convert the native dendra2 (green) fluorophore into its transformed (red) fluorescent state, UV exposure conditions were standardized to achieve optimal level of fluorophore conversion. Cells transfected with dendra2 tagged proteins of interest were subjected to different strengths of UV light exposures (405 nm), to test for post-conversion red fluorescence detection and the subsequent effect of UV light on migratory behavior of cells. Presented in figure 3.6, are three photoconversion conditions for dendra2-β-actin transfected cells i.e. exposure to 2%, 8% and 20% strengths of 405 nm light.

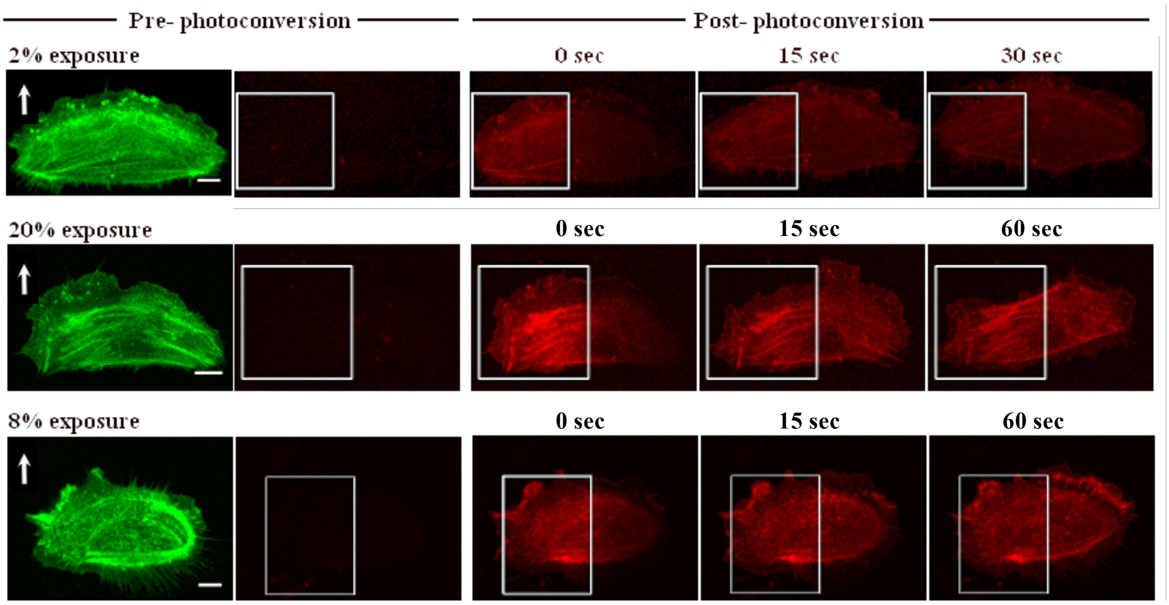

Figure 3.6: Optimizing the 405 nm exposure to achieve fluorophore photoconversion in dendra2-β-actin transfected keratinocytes. 2% UV exposure produces too less conversion for overtime detection. 20% UV exposure hinders the normal cell migration behavior. 8% UV exposure produced optimum photoconversion. Scale bar = 10 μm.

Pre-conversion (green), native fluorescent state of dendra2 was imaged using 488 nm excitation laser and a bandpass filter settings in the range 495 nm-550 nm for detection. The photoconverted (red) state of dendra2 was imaged using 561 nm excitation laser and bandpass filter of 570 nm-695 nm for detection. To optimize the strength of UV photoconversion, only a sub-region of the cell transfected with dendra2-β-actin was exposed to 405 nm light using a rectangular region of interest (white rectangle in figure 3.6). Upon exposure with 2% UV light, the intensity of post-conversion signal obtained was low and noisy. This can be seen in figure 3.6 as a faint red signal in post-conversion 0 sec inset. With time, as this low photoconverted signal begins to scatter out of the ROI, its becomes untraceable. 2% UV exposure was thus considered to be not enough for efficient conversion and detection of dendra2. Upon exposure with 20% UV light, the intensity of photo-converted signal achieved was much higher and with less noise. Although, during post-conversion imaging, dramatic changes in cell's migratory behavior were observed. Due to strong UV exposure, cells were observed to stall and lost their polarized morphology. This can be seen in figure 3.6 in 60 sec inset, where the polarized actin cytoskeletal network of the cell is completely lost after harsh UV exposure. Therefore, 20% exposure was considered to be too strong. In order to establish a good balance between efficiently detectable dendra2 photoconversion and unhindered cellular migration, 8% UV exposure was found to be optimum. As shown in figure 3.6, the post-conversion signal intensity was high enough to be detected and no significant hindrance to normal cell migration behavior was detected. Hence, a 8% 405 nm light exposure was used in all experiments to carry out dendra2 photo-conversion.

3.2.2 Post-conversion dendra2 imaging parameters

Dendra2 fusion proteins of actin, myosin IIa and vinculin were transiently transfected into human keratinocytes, to primarily label the cytoskeletal filament network and focal adhesions with native dendra2 form. To standardize the post-conversion imaging parameters, single cell photoconversion was performed to convert the entire dendra2 labelled pool into red fluorescent state. Post-conversion imaging was then tuned to make excitation laser adjustments in order to minimize the overtime signal loss by photo-bleaching. Presented in the figure 3.7-A, are the native and converted dendra2 states for β-actin. Approximately 49% (±5%) fluorophore was photoconverted from green to red state using the previously described standardized conversion exposure. The post-conversion dendra2 signal was then imaged for atleast 5 minutes, to observe for photo bleaching. Minimal bleaching effect was observed with 1.6% of excitation laser (561 nm) and was therefore used for all dendra2-ß-actin experiments. Figure 3.7-B presents the post-conversion dendra2-β-actin imaging for one cell, where the white dotted lines marks the cell boundary.

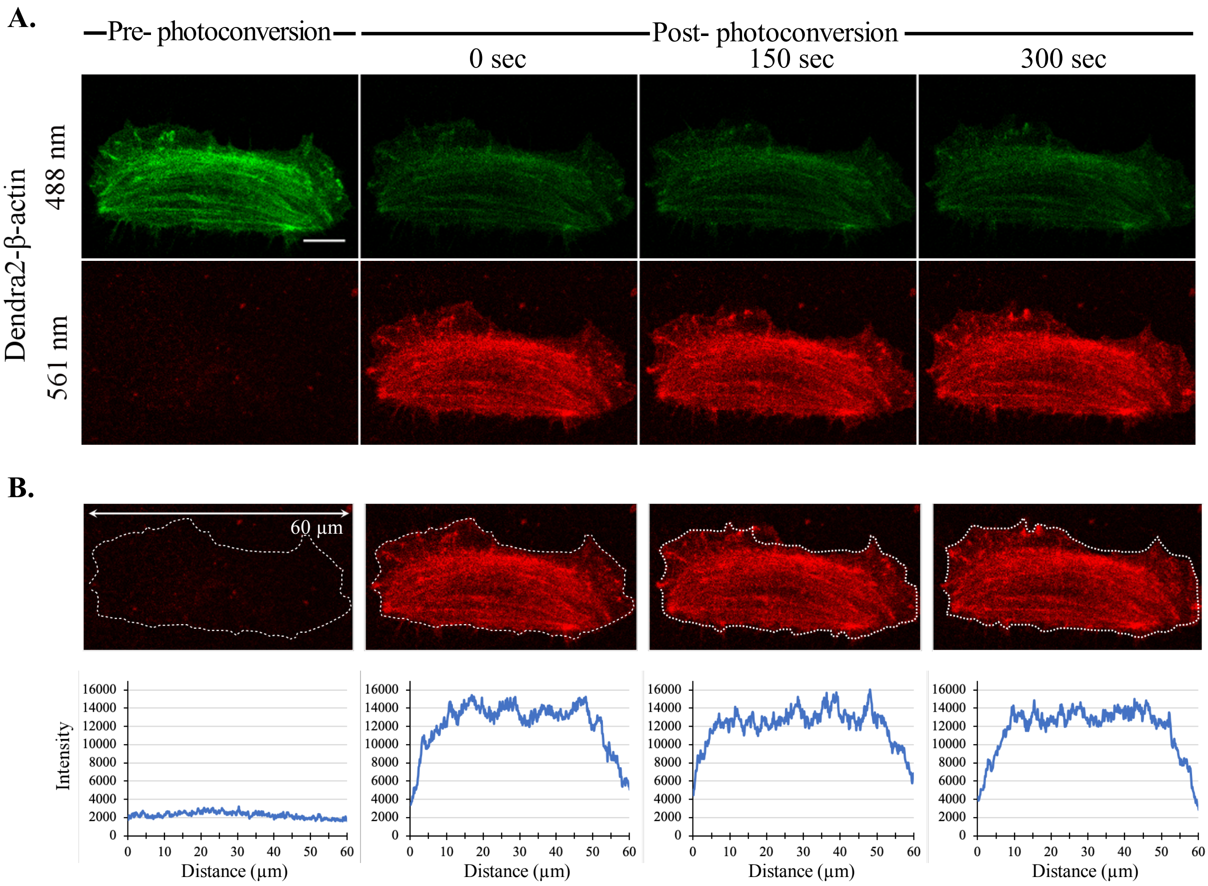

Figure 3.7: (A) Standardizing post-conversion imaging parameters for dendra2-β-actin, by photo-converting a single cell. Scale bar = 10 μm. (B) Post-conversion dendra2 imaging was performed using 1.6% of 561 nm excitation laser. Dotted line represents the cell boundary and the respective intensity curves represent the intensity profiles of the enclosed cell area.

Using ImageJ software, the intensity of area enclosed within the cell boundary with respect to its length, was measured and is shown in the form of respective time curves. The overtime intensity loss during post-conversion imaging due to bleaching was performed for 10 individual cells and was observed to be minimum.

Likewise, the imaging conditions for dendra2-myosinIIa and dendra2-vinculin were tuned for post-conversion imaging using single cell conversions (10 cells in each category). 1.7% and 1.9% of excitation laser (561 nm) was found to be optimum for post-conversion dendra2-myosin and dendra2-vinculin imaging, with minimal photobleaching. Keeping the conversion parameters constant, on average approximately 55% (±4%) for dendra2-myosinIIa and 45% (±5%) green to red conversion for dendra2-vinculin was obtained. Figure 3.8 and 3.9 presents the respective imaging conditions in one cell.

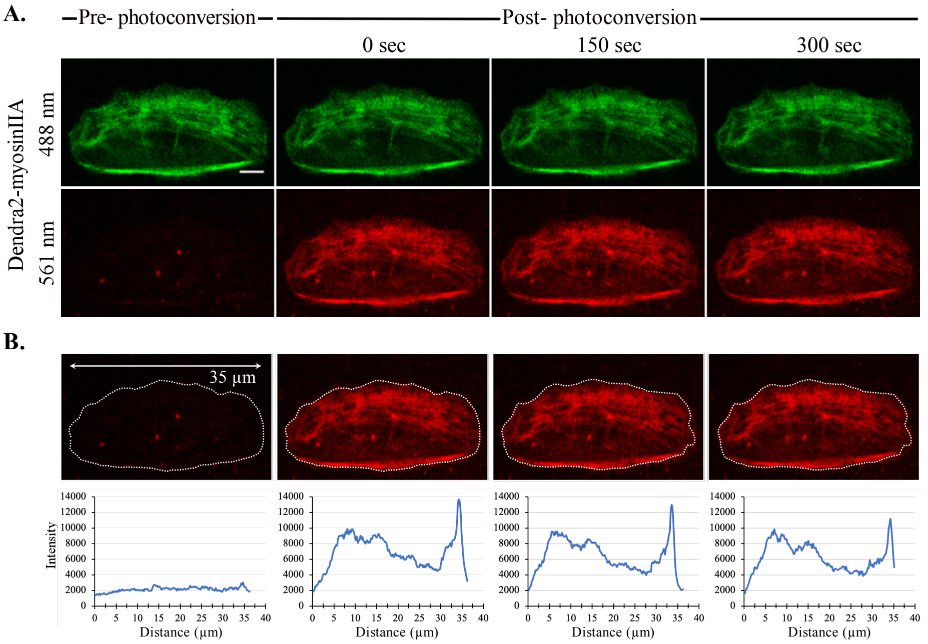

Figure 3.8: (A) Standardizing post-conversion imaging parameters for dendra2-myosinIIA, by photo-converting a single cell. Scale bar = 10 μm. (B) Post-conversion dendra2 imaging was performed using 1.7% of 561 nm excitation laser. Dotted line represents the cell boundary and the respective intensity curves represent the intensity profiles of the enclosed cell area.

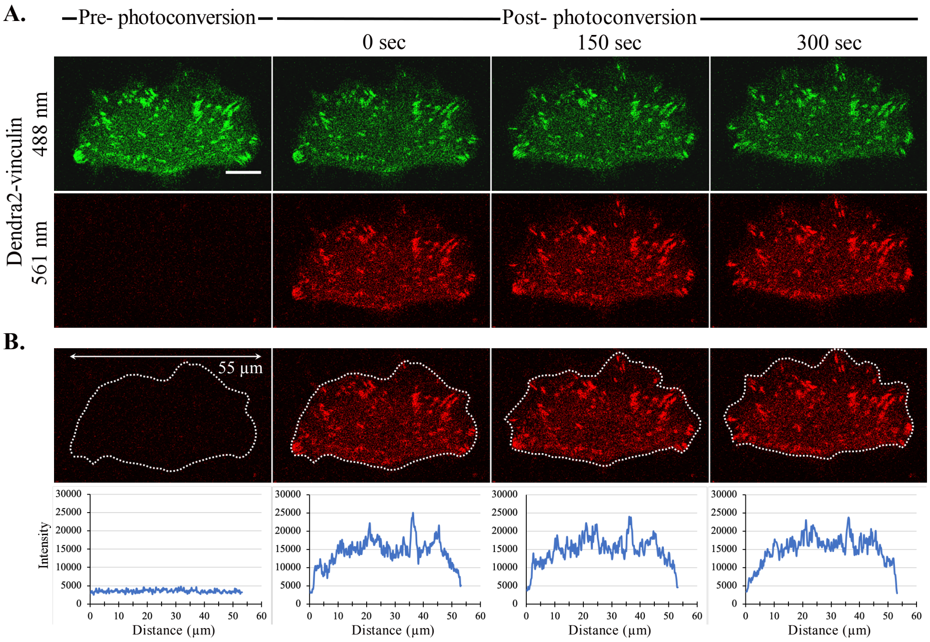

Figure 3.9: (A) Standardizing post-conversion imaging parameters for dendra2-vinculin, by photo-converting a single cell. Scale bar = 10 μm. (B) Post-conversion dendra2 imaging was performed using 1.9% of 561 nm excitation laser. Dotted line represents the cell boundary and the respective intensity curves represent the intensity profiles of the enclosed cell area.

CHAPTER 4

Results: Cytoskeletal filament dynamics

In this chapter, the observed dynamic behavior of primitive stress fiber components: actin and myosin is presented, with main focus on front-to-rear differences in migrating keratinocytes. β-actin and myosin IIa isoforms were used as target molecules, labelled with dendra2. Localized dendra2 photoconversion was performed in transfected keratinocytes (pre-stimulated with epidermal growth factor (EGF) for migration), to tag a partial molecular population. Subsequent re-location of photoconverted signal to the unlabeled parts of the cell was then analyzed. Distinct actin turnover behavior of circular transverse arcs, located in the cell body and rear-end SF, aligned flat at the cell's trailing edge is reported here. Finally, myosin IIa mobility in the two stress fiber bundles is presented, showing the dependence of myosin II mobility in stress fibers with overall cell migration speed.

4.1 Microfilament actin turnover dynamics

4.1.1 Actin distribution by cytosolic transfer

In order to explore the cytoskeletal actin dynamics in different stress fiber assemblies, a localized dendra2 photoconversion, in dendra2-β-actin transfected nHEKs was performed. Localized exposure to 405 nm light in one half of the cell (indicated by the white ROI in figure 4.1) led to green-to-red fluorescence conversion specifically in this sub-cellular area.

Overtime progression of photo-converted signal from ROI, into non converted parts of the cell was then traced. An immediate transfer of photoconverted actin signal to the non-converted parts of the cell was observed and the signal was found to travel in the cell body and ultimately reached till the opposite cell edge. To analyze this immediate actin transfer into the non-converted parts of the cell, an image processing routine was designed. The increase in post-conversion signal in the non-converted part of the cell, was analyzed along defined subregions. The over time intensities were measured as in definite color coded sub-regions in the cytoplasmic area (area of the cell where no SFs were present), at consecutive distances of 5, 10, 15 and 20 μm from the border of the photoconversion ROI (colored squares in figure 4.2-A).

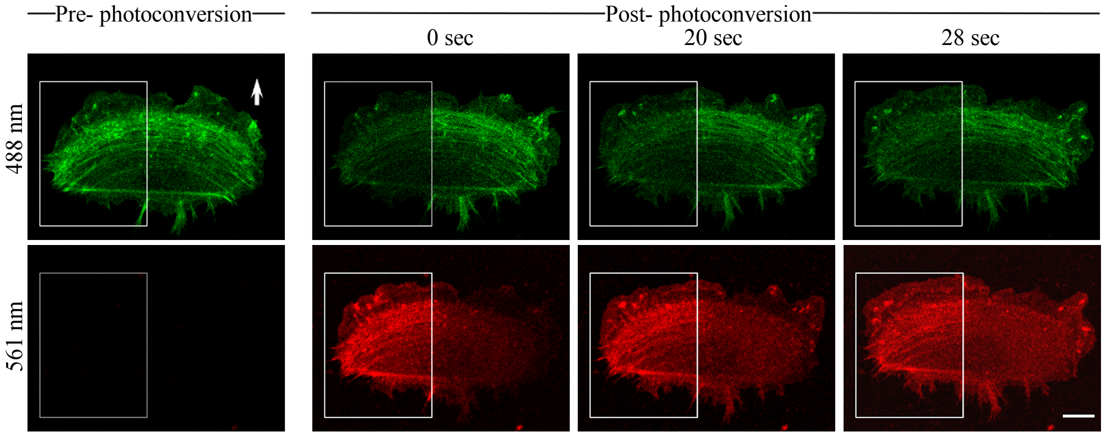

Figure 4.1: Photoconversion of dendra2-β-actin in a migrating keratinocyte, with half of the cell's lamellipodia and cytoplasmic compartment inside the photoconversion ROI. White arrow points in the direction of cell's migration. The post conversion time sequence represents the immediate transfer of actin out of the photoconversion ROI, into the non-converted part of the cell. Scale bar = 10 μm.

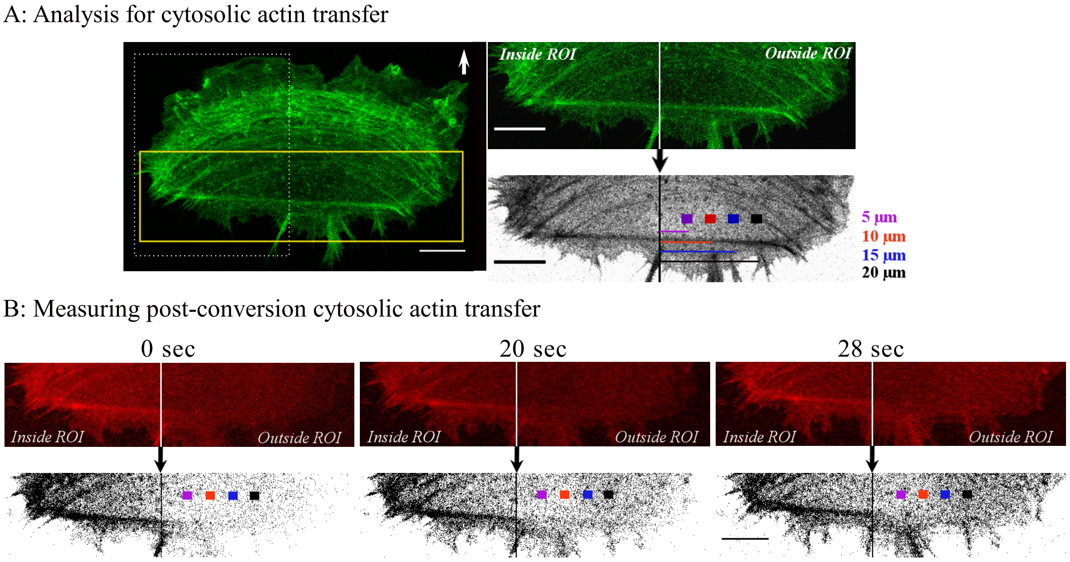
A: Analysis for cytosolic actin transfer

B: Measuring post-conversion cytosolic actin transfer

Figure 4.2: Analysis strategy used to analyze the cytosolic actin transfer in cytosolic cell areas, free of stress fibers. (A) Green channel was used as a reference to set the analysis parameters. The magnified area, marked with yellow borders, displays the stress fiber free region of the cell which was selected for analysis. Four color coded sub-regions at different distances (5 μm, 10 μm, 15 μm and 20 μm) from the ROI were chosen. (B) The selected sub-regions were used to quantify over time post-conversion intensity changes in the red imaging channel. Scale bar = 10 μm.

Upon quantifying overtime sub-regional intensities, fastest intensity increase was observed in the sub-region closest to the border of photoconversion ROI, at 5 μm distance (magenta curve in figure 4.3). Almost immediately after conversion, the average post-convertion signal in this sub-region was seen to increase to a higher value and remained constant thereafter. Subsequent increase and saturation of photoconverted signal was then seen in the cytosolic area at 10 μm (red), followed by 15 μm (blue) and 20 μm (black) sub-regions. The initial low average intensity values of red, blue and black regions increased constantly with time to ultimately reach maximum intensity, with no further increase. 20 μm (black) sub-region being farthest from the photoconversion ROI, was the last observed to approach the maximum intensity level. The sequential delay in acquisition of signal with respect to increasing distances from the photoconversion region, indicated transfer of actin units by cytoplasmic transfer. The ultimate intensity values reached in all the color coded regions was identical and once reached, no subsequent increase was observed. This implied rapid actin transfer by simple cytosolic diffusion.

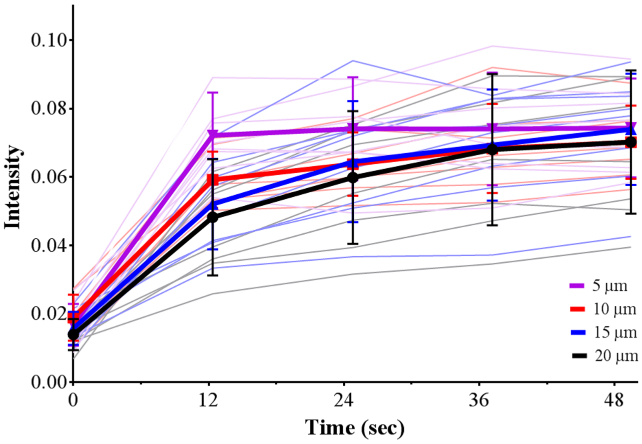

Figure 4.3: Intensity profile of photoconverted actin transfer in the cytosol. The analyzed sub-regions were at consecutive distances from the border of photoconversion ROI: 5 (magenta), 10 (red), 15 (blue) and 20 (black) μm. Thin lines represents individual cells and thick lines indicates respective averaged profiles. The error bars indicate the error in SD (n= 10 cells).

Within the limits of the confocal system employed in these experiments (scan time of ~9 sec), the photoconverted actin signal was already re-distributed to the non-converted part of the cell, by the time of first image acquisition after conversion (seen in 0 sec image in figure 4.1). The temporal delay in imaging can be seen as non-zero starting intensity value at 0 sec in figure 4.3. Nevertheless, the overtime intensity quantification in the defined sub-regions was still possible. To eliminate the effect of this primary re-distributed signal, minimum-maximum intensity normalization was performed for each sub-region. The minimum intensity value, i.e. in first frame after photo-conversion (0 sec time point) was scaled to zero and the maximum intensity value in each data set was set to 1. The obrained intensity profiles of each data set was therefore scaled to lie in the range of 0-1. The normalized mean intensity profiles of respective sub-regions from 10 individual cells is presented in figure 4.4, with error bars indicating the error as standard deviation (SD).

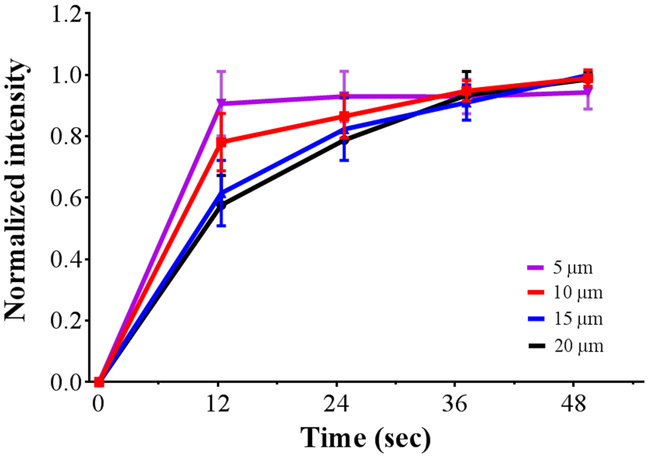

Figure 4.4: Min-max normalized mean intensity profiles of analyzed sub-regions to analyze cytosolic actin transfer in SF free region of the cell. Error bars indicate the error in SD for 10 cells.

The observed cytoslolic transfer of photoconverted actin in the cell areas free of actin fibers, correlates to the cytosolic actin diffusion in the cell body. The measured pool of actin is purely contributed by existing actin pools inside the photoconversion ROI, enabling exclusive focus on actin transport or exchange between cellular compartments and eliminates the possible interference from de-novo synthesis.

4.1.2 Actin turnover in stress fibers is manifested by cytosolic actin transfer

After identifying rapid cytosolic transfer in cell areas free of stress fibers, actin turnover in stress fibers was monitored. Unlike cytosolic space, stress fibers are discrete actin containing structures, which undergoes constant changes in position due to the overall displacement of the cell during migration. In parallel to this, the ongoing cycles of SF contraction-relaxation, causes constantly changing stress fiber geometry, especially for transverse arcs. These SFs undergo constant alterations in their curvature radius during the course of cell's migration. Such alterations in stress fiber position and geometry, complicates their detection in real time and makes quantitative analyses difficult. Considering all underlying analytical challenges, a 'stress fiber tracking' image processing tool was developed by our collaborating partners, Dmytro Kotsur and Dr. Julian Mattes from *Software Competence Center Hagenberg, Austria.* The tool enabled identification of discrete actin stress fibers and enabled tracing real time changes to their shape and position during cellular movement. The tracking software uses an artificial contour to find and track filament positions in a time lapse sequence. It efficiently sustains changes to fiber shapes and position during migration (detailed explanation in section 2.6). The fiber tracking tool was implemented to track actin stress fibers and quantify post-conversion actin transfer into transverse arcs and the rear-end SF areas. Figure 4.5 displays the target cell areas for transverse arcs and rear-end stress fiber analysis.

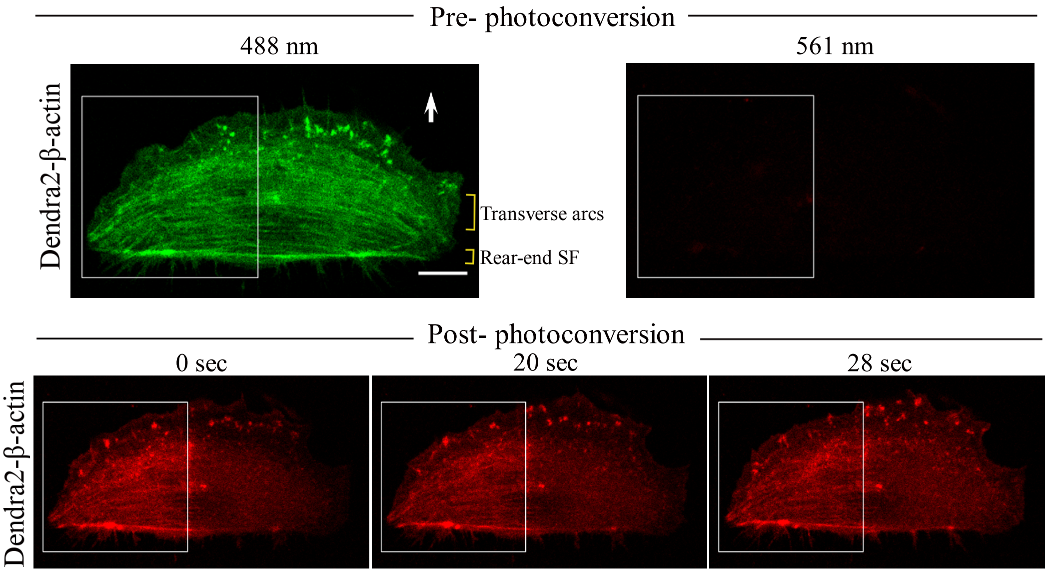

Figure 4.5: Photoconversion of dendra2-β-actin in one half of the cell, where the post-conversion signal undergoes redistribution into transverse arcs and rear-end SF areas on the non-converted part of the cell. White arrow points in the direction of cell's migration. Scale bar = 10 μm.

Transfer of photoconverted actin signal along actin arcs and rear-end SF areas was analyzed using the combination of tracked SF trajectories and the analysis method used previously for cytosolic actin transfer (in section 4.1.1). Color coded sub-regions, located at consecutive distances of 5, 10, 15 and 20 μm from the border of the photoconversion region of interest were defined and overtime intensity profiles of each sub-region were determined. Figure 4.6-A shows the analyzed arcs and rear-end stress fibers, along with labelled sub-regions.

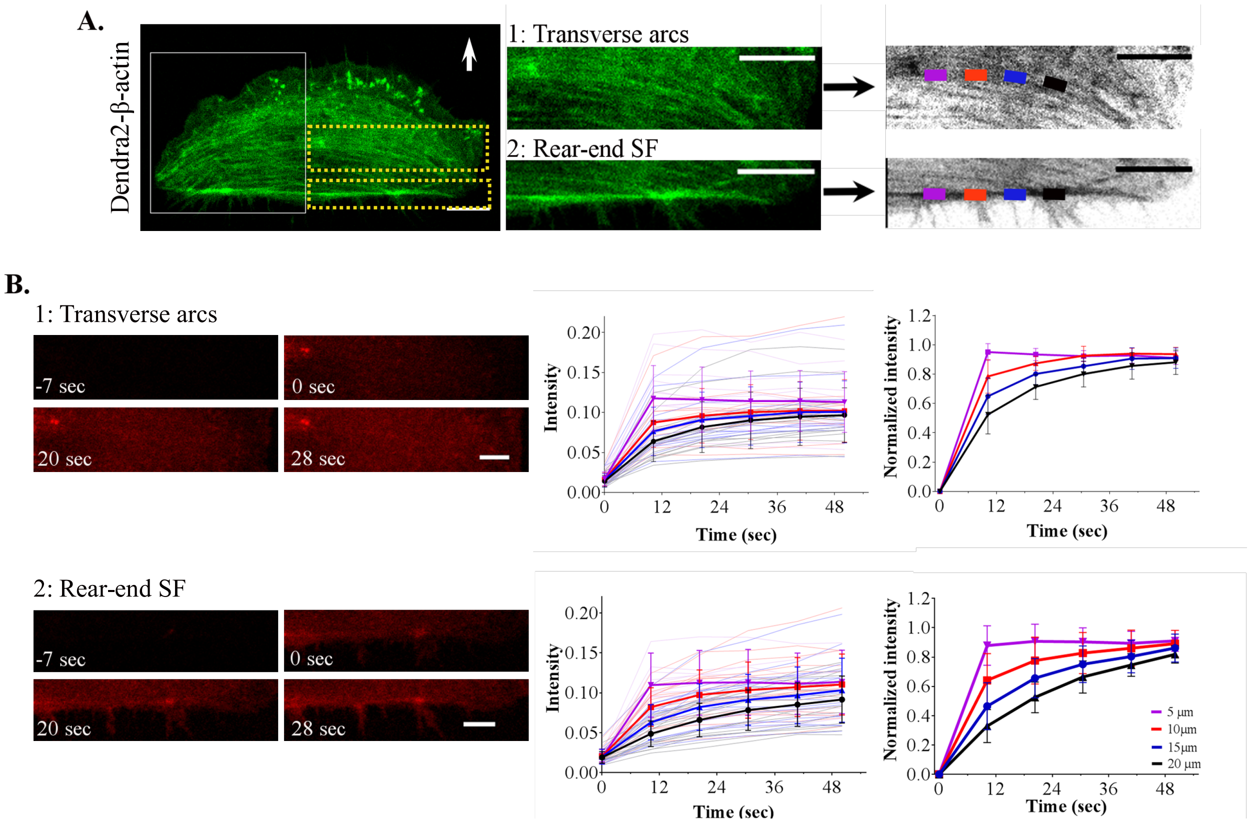

Figure 4.6: Post-conversion analysis of actin distribution in transverse arcs and rear-end SF areas, using color coded sub-regions. (A) Actin arcs and rear-end SF areas were analyzed in 5 μm (magenta), 10 μm (red), 15 μm (blue) and 20 μm (black) sub-regions. Scale bars = 10 μm. (B) Post-conversion actin distribution in areas of arcs and rear-end SF. Scale bar = 5 μm. The left intensity curve shows the mean of absolute intensity profiles and the right curve shows min-max normalized intensity profiles of respective stress fiber structures.

In both transverse arcs and rear-end SF areas, the 5 μm (magenta) sub-region, closest to the region of photoconversion acquired the signal first, followed by 10 μm (red), 15 μm (blue) and 20 μm (black) sub-regions. This can be seen on respective intensity curves (left) for transverse arcs and rear-end SF areas in figure 4.6 (B). The data sets presented in these curves were then normalized (right curve) with min-max normalization (explained previously in section 4.1.1), to scale all intensities in the range of 0-1. The intensity profiles for transverse arcs and rear-end SF sub-regions were found to be similar to previously described profiles for actin transfer in cytosol in figure 4.4. These observations indicated rapid actin transfer into transverse arcs and rear-end stress fiber areas by cytosolic transfer.

4.1.3 Actin turnover in transverse arcs and the rear-end stress fiber

After having analyzed the early actin transfer into transverse arcs and rear-end SF areas, actin turnover in the two stress fiber types was monitored over an extended period of time. Subsequent to the initial cytosolic actin transfer, cells were further imaged and localization of post-conversion actin was monitored.

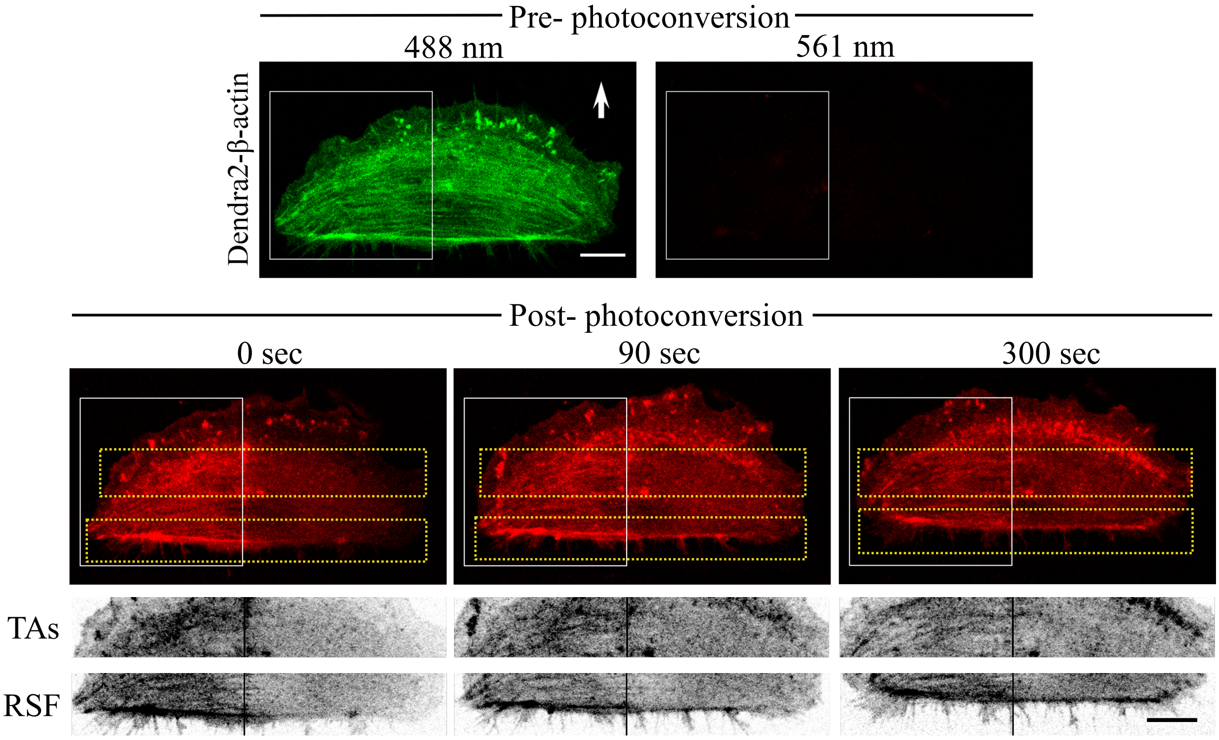

Figure 4.7: Post-conversion actin turnover in transverse arcs and rear-end stress fiber after early actin diffusion. Region enclosed within the rectangles with dotted edges indicate the transverse arcs (center) and the rear-end stress fiber (rear) regions. Scale bars = 10 μm.

The localization of postconversion actin into SFs, will occur only as a consequence of actin exchange in stress fibers, i.e. when SF resident actin is exchanged for available photoconverted actin. The two SF bundles, transverse arcs and the rear-end stress fibers demonstrated distinct turnover behaviors. The rear-end fiber displayed strong buildup of post-conversion actin signal, which can be seen on the SF bundle, in the non converted part of the cell during post-conversion imaging (RSF insets in figure 4.7). The buildup of photoconverted actin indicated an active exchange in the rear-end SF. Transverse actin arcs however displayed only a diffused photoconverted actin signal (TAs insets in figure 4.7), with no significant localization into discrete fiber structures. This indicated absence of active turnover of actin in this stress fiber type.

In order to visualize closely, the post-conversion actin assembly process into SFs, transverse arcs and rear-end SF were individually tracked using the active fiber tracking routine, explained earlier in section 2.6. Individual stress fibers, which are usually curved or arched, were then processed and normalized for their shape. Their arched morphology was modified into a straight line using image processing steps explained in section 2.6.2, to eliminate any curves or bends.

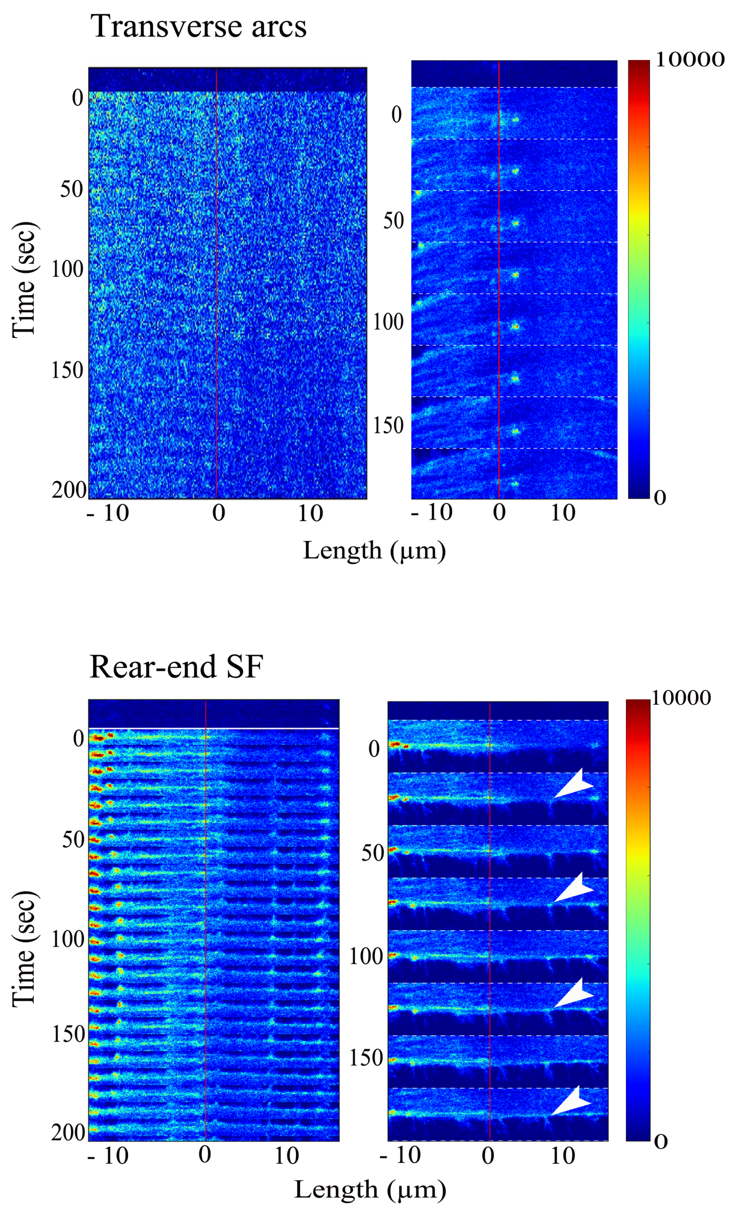

Figure 4.8: Kymographs representing the post-conversion actin incorporation into the transverse arc and the rear-end stress fiber. The red line indicates the border of the region of photoconversion.

Real time post-conversion intensity profiles of respective stress fibers were then quantified and were represented in the form of kymographs. The kymographic representation of each SF type can be seen in figure 4.8. The left kymograph depicts the incorporation of post-conversion actin in the tracked fiber and the right kymograph shows the intensity profile of the same fiber, along with the respective offsets areas. The color scale of kymographs indicates the range of pixel intensity. Overall kymograph intensity was scaled between 0-10000 pixel grey value, where the minimum pixel intensity is set to 0 and maximum pixel intensity to 10000. The y-axis represents imaging time points in seconds, where the first frame corresponds to pre-conversion dark state. 0 sec time point corresponds to the first image of the SF after photoconversion. The x-axis on the kymographs represents length of the fiber in microns. The red line at 0 μm mark represents the border of photoconversion region of interest. Area of fiber inside the photoconversion ROI is marked with negative (-) distance units and the stress fiber length lying outside the photoconversion ROI, in the non-converted area of the SF, is labelled with positive (+) distance units. The post-conversion actin turnover of respective SFs could then be monitored in the SF region lying in the non-converted area i.e. with positive distance units. As observed earlier, kymograph for transverse arcs displayed randomly diffused post-conversion actin signal in the non-converted area of the SF (indicated by '+' distance units). No significant actin incorporation into discrete arc structures was observed. Even after observing the arcs over a longer time period (upto 300 sec), no significant localization was observed. The random actin distribution was similar to that observed for cytosolic distribution, in the areas of the cell where no SFs are present (section 4.1.1). The rear-end SF however, displayed an accumulation of post-conversion actin in SF area lying in the non-converted part of the cell. This can be seen as bright spots on the positive (+) length side of the SF. Upon considering the surrounding offset areas of the rear-end stress fiber, a heterogeneous actin incorporation along the fiber length was observed at early time points, i.e. localization of new actin did not occur homogeneously along the SF length, but rather at discrete sites on the SF. The post-conversion actin spots appeared at an early time point (indicated by white arrow heads in figure 4.8) and were observed to increase in their intensity and size with time, before they finally dissolved into the stress fiber bundle. Non-homogeneous localization of post-conversion actin on the rear-end SF therefore indicates that either actin turnover sites are discretely located on the rear-end SF or some turnover sites undergo faster actin exchange than other turnover sites on the SF.

Furthermore, significant role of rear retraction fibers, which are usually attached to the rear cell edge, in actin turnover at RSF was established. The discrete bright localization spots of post-conversion actin on rear-end SF were observed to be localized at the position on the stress fiber bundle coinciding with proximal ends of membranous retraction fibers. Figure 4.9 presents a magnified view of the rear-end SF, along with offset areas showing the retraction fiber trails

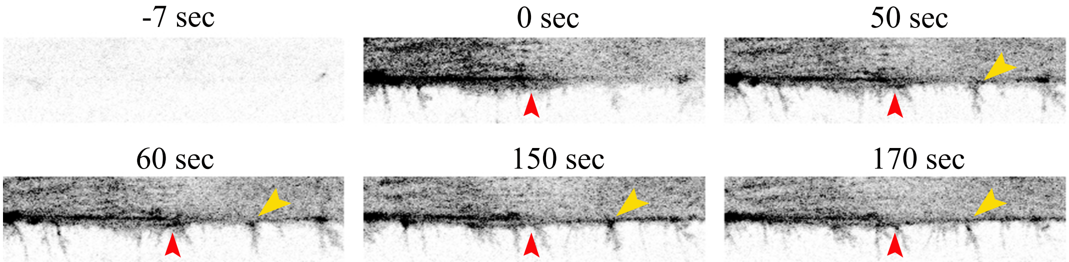

Figure 4.9: Incorporation of post-conversion actin into the rear-end SF through anterograde flow via retraction fibers at the rear cell edge. The red arrowhead defines the location of the border of photoconversion ROI and the yellow arrowhead emphasizes one of the discrete actin assembly points at the retraction fiber trails.

behind the cell. A stream of incoming post-conversion actin was seen to flow into this SF bundle by anterograde flow of actin aggregates through the retraction fiber trails. Here, the yellow arrow head marks the position of attached retraction fiber and the bright actin localization spot. Further, the overtime tracked trajectories of transverse arcs and rear-end SFs were used to quantify the post-conversion actin intensity changes in the two stress fiber bundles. The gray values along the length of transverse arcs and rear-end SF in the non-converted region of the cell, i.e. the SF area in the positive (+) length region on the kymographs in figure 4.8, was averaged at each time point. The obtained intensity profiles were min-max normalized and are presented in figure 4.10, with red curve representing the overtime intensity changes in transverse arcs and the violet curve representing the intensity changes in rear-end SF.

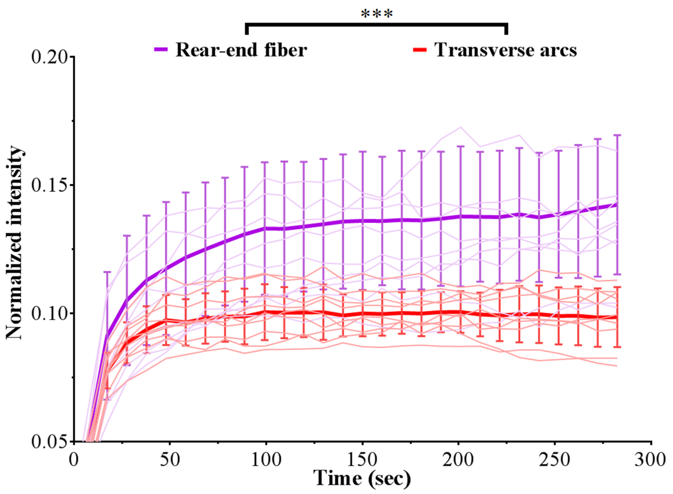

Figure 4.10: Plot showing the normalized post-conversion intensity profiles of transverse arcs (red) and the rear-end SF (violet), for 12 different cells. Thin lines represents individual cells and bold lines show the respective mean curves. Error bars indicate the error in SD. The two actin stress fiber types were found to be significantly different with p-value< 0.001, using parametric paired t-test.

Rapid initial increase in post-conversion actin observed at near 20 sec time point in both stress fiber types, was mainly due to rapid cytosolic actin transfer which was described earlier in section 4.1.2. Thereafter, the two stress fiber types displayed distinct post-conversion actin incorporation profiles. The transverse arcs demonstrate no significant further intensity increase after initial rapid actin transfer, indicated by the plateau curve. The rear-end SF intensity curve however, demonstrated a steady overtime increase, followed by saturation phase. Differences in intensity profiles of the two stress fiber types can be seen in figure 4.10, where the overtime profiles from 12 different cells are presented. The observed differences in intensity profiles of the two stress fiber bundles were also tested for their statistical significance, using two-tailed paired t-test. P-value of < 0.05 indicated that the observed turnover differences between the two SF types did not occur by chance.

Overall, combining together the observations from this section, rapid cytosolic actin transfer into stress fiber areas was observed. The transferred actin pools further contributed to the stress fiber turnover. Turnover differences between spatially separated transverse arcs and rear-end SF were characterized, where higher actin exchange kinetics was observed in rear-end SFs, compared to transverse arcs. Finally, the anterograde actin flow via rear retraction fibers was observed to feed in free actin pools for rear-end SF turnover, at discrete locations on the SF.

4.2 Non-muscle myosin II cytoskeletal dynamics

Another critical stress fiber component, myosin II, plays a crucial role in cell migration. Migrating cells maintain their flexibility and exerts high contractile forces on underlying substrates using myosin II, to carry out stress fiber contraction-relaxation cycles. After determining turnover characteristics of actin in different stress fibers, myosin II dynamics in transverse arcs and rear-end stress fibers is presented in this section. Due to the specifically known role of non-muscle myosin IIa (NMIIA) isoform in filament contraction and trailing edge retraction [133] [134], dendra2 coupled NMIIA was used to carry out photoconversion in one half of the cell and subsequent redistribution of converted signal was then analyzed.

4.2.1 NMIIA dynamics in transverse arcs and rear-end SF

Non-muscle myosin IIa turnover in transverse arcs and rear-end SF was studied, where photoconvesion of dendra2-NMIIA was used to specifically label (figure 4.11) and monitor myosin transfer into the non-converted part of the cell. Unlike the observation for actin, no rapid transfer of post-conversion myosin was detected. Rather, the transfer occured along the stress fibers.

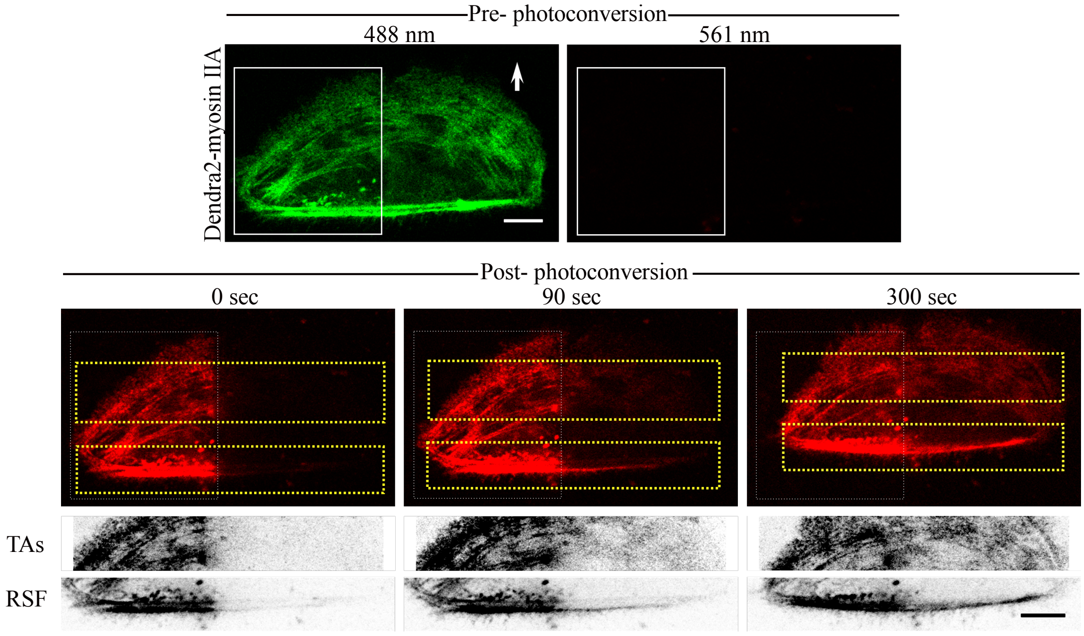

Figure 4.11: Photoconversion of dendra2-myosin IIA to monitor its motility in transverse arcs and rear-end SF. Analyzed regions for respective SFs are enclosed within red and violet rectangles. NMIIA displays a tight displacement along the actin stress fiber network. White rectangle and white arrow indicates the region of photoconversion and direction of cell's migration. Scale bar = 10 μm.

Post-conversion imaging in figure 4.11, demonstrates overall myosin II dynamics. Specific transfer along transverse arcs and rear-end SF can be seen in the magnified insets, where the transfer occured along the two stress fiber types. Further, both stress fiber types were tracked using the fiber tracking tool, in the same way as described previously for actin turnover analysis. Upon processing the transverse arcs and rear-end SFs individually, the myosin transfer patterns in two stress fiber types were represented in the form of following kymographs.

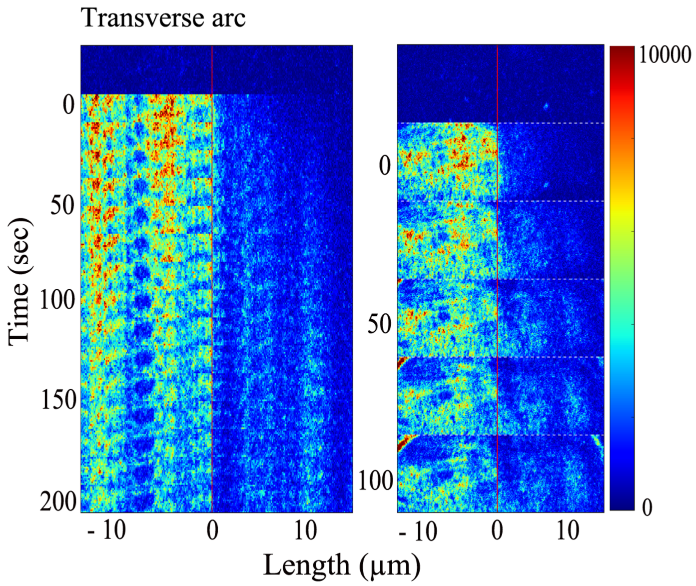

Figure 4.12: Kymographs showing post-conversion myosin IIa mobility along the transverse arcs. Red line at 0 μm indicates the border of the photoconversion region of interest.

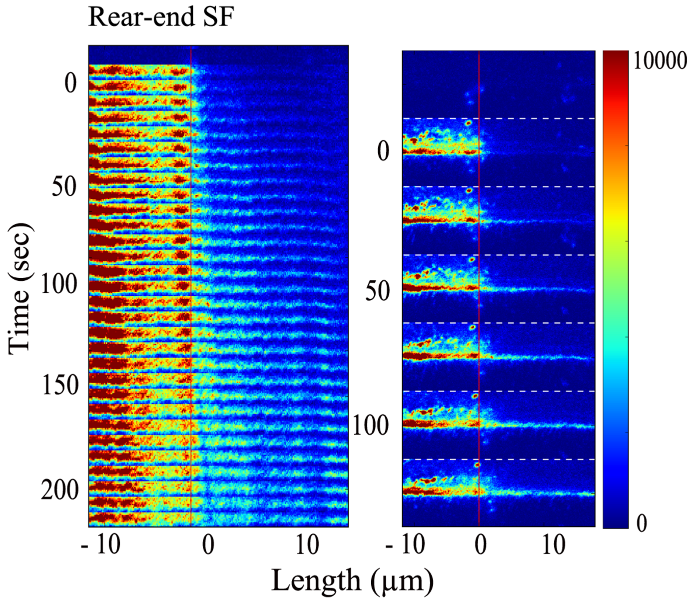

Figure 4.13: Kymographs showing post-conversion myosin IIa mobility along the rear-end SF. Red line at 0 μm indicates the border of the photoconversion region of interest.

The kymographs represents real time intensity profiles of the two stress fiber types, as post-conversion myosin signal begins to distribute out of the photoconversion ROI. The color scale bar of the kymographs indicate the range of computed gray values, which were scaled between 0-10000. The post-conversion myosin signal was observed to travel along the arched length of transverse arcs. This can be seen as signal points on the kymograph (figure 4.12), at the positive (+) length side. Similar to transverse arcs, the transfer of post-conversion myosin signal along the rear-end SF was observed to be stringent along its length. Starting from the border of photoconversion ROI, the overtime propagation of myosin signal was observed to occur in steps. Due to stress fibers being located very close to each other in the central region of the cell, the effect of stringent myosin mobility along discrete fiber bundles was less evident in transverse arc areas. However, in the rear-end SF, the stringent myosin mobility was more prominent (figure 4.13), clearly displaying steady overtime increments. Myosin transfer dynamics along the rear-end SF, with respect to overtime intensity profiles, is presented in the following figure.

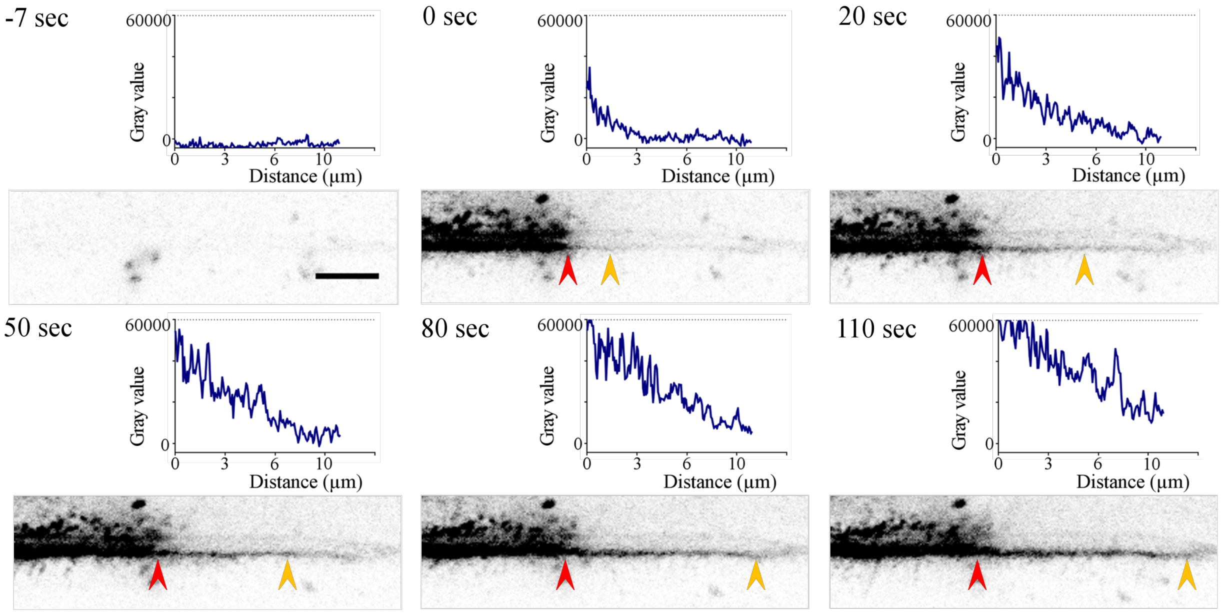

Figure 4.14: Post-conversion myosin IIa mobility along the rear-end SF. The red arrow head defines the position of photoconversion ROI and the yellow arrow head implies overtime stringent myosin IIa mobility along this SF. Respective curves indicates the overtime changes in myosin IIa signal with respect to rear-end SF length. Scale bar = 3 μm.

Myosin II dynamics along rear-end SF in figure 4.14, can be traced from the increasing distance between arrow heads marking the border of the region of photoconversion (red) and the myosin signal points (yellow). The signal points indicate the post-conversion myosin signal advancement at each time point. The overtime increasing distance between the red and yellow arrow heads indicates stringent dynamics of stress fiber resident myosin II.

4.2.2 NMIIA mobility in rear-end SF correlates with migration speed

After examining stress fiber associated myosin II dynamics, the dependence of overall cell's migration on the observed myosin dynamics in the SF bundle at cell rear was investigated. Since overall cell body translocation in direction of migration determines the rate of its migration [75], the tracked rear-end stress fiber trajectories (from section 4.2.1) were used to obtain the overall speed of migration. The rate of stress fiber displacement in the direction of migration was considered as overall cell migration speed. Additionally, information from myosin intensity kymographs of rear-end SFs (shown in figure 4.13) from a sample population were used to compute the speed of the post-conversion myosin signal transfer along the rear-end SF bundle. Using image processing, overtime myosin signal displacement points from kymographs were extracted to calculate the speed of myosin transfer along the SF. This was done in following steps:

- Myosin transfer kymograph was sampled and a signal threshold value was used to determine the distance travelled by post-conversion myosin signal. The lowest available pixel value in the entire kymograph was assigned as the background pixel value. This background pixel (yellow pixel point in figure 4.15) was identified mainly in the dark regions of the kymographs, i.e. the area representing pre-conversion time points. The background value was then used to set a threshold to determine a foreground value (single green pixel points in figure 4.15) at every time point.

  Foreground pixel = 2 x (background pixel value)

  The identified foreground pixel at one time point therefore defines the corresponding distance moved by post-conversion myosin at that time point.

- Foreground pixels from all time points of kymograph were collected and overtime myosin II mobility steps, from the border of photoconversion ROI were obtained in the form of foreground points at every time frame (shown as green pixel points in figure 4.15).
- Once all foreground pixels were identified, a straight line was fitted onto the detected foreground pixel points (indicated by the green dashed line in figure 4.15).
- Slope of the fitted line was then determined and was considered as the post-conversion myosin transfer speed in units of μm/sec.

After determining the overall cell migration speed and post-conversion myosin signal transfer speed along the rear-end SF, a correlation between the two measured parameters was established. Dependence of cell migration speed on myosin II mobility along the rear-end SF was

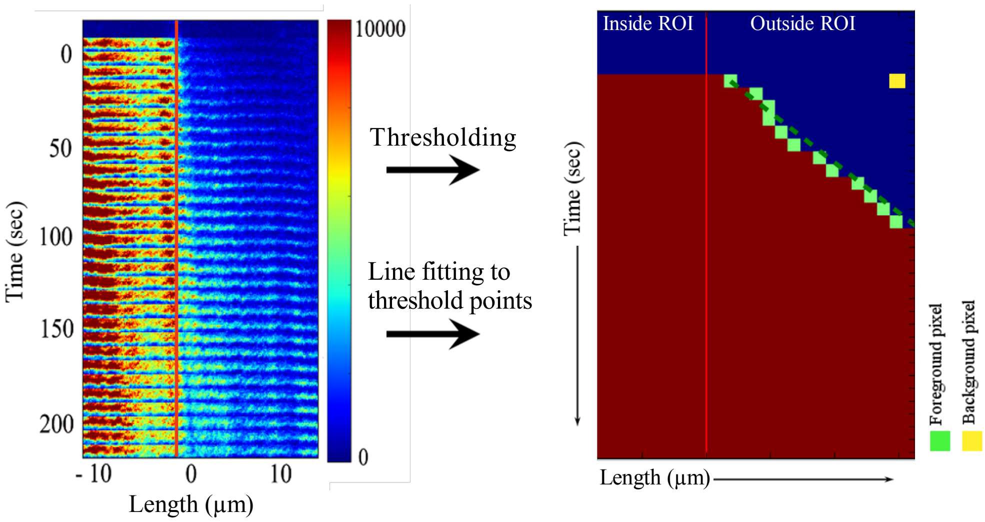

Figure 4.15: Image processing strategy to evaluate the speed of post-conversion myosin IIa propagation in the rear-end SF bundle, using foreground thresholding of 2x background.

tested, where the latter was considered as independent variable. The correlation was tested using linear regression analysis detailed in section 2.7. Individual quantifications of cell migration speed and the speed of myosin transfer along rear-end SF was performed for each cell. Taking myosin IIa transfer speed as independent variable (on x-axis) and cell's migration speed as the dependent variable (on y-axis), the calculated values from 13 different cells were put into a scatter plot (data points in figure 4.16).

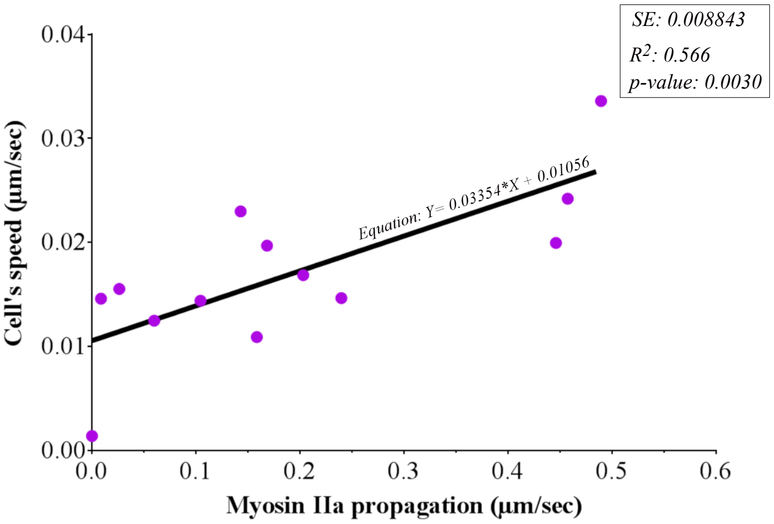

Figure 4.16: Correlation between cell migration speed and myosin IIa propagation along rear-end SF. x-axis represents the myosin IIa propagation and on y-axis is the cell's migration speed, both in μm/sec. Individual data point represents the analyzed myosin mobility per RSF.

In order to establish a relationship between the two analyzed parameters, a best-fit linear regression line of the form Y= a + b*X was fitted to the scatter plot (solid line in figure 4.16) with 95% confidence interval. The best-fit line was calculated using the least squares method (explained in section 2.7) available in GraphPad Prism software. The goodness of fit was then evaluated from the calculated values of coefficient of determination (R^2). The calculated R^2 value was 0.566 ± 0.008, which establishes ~56% linear relationship between myosin II transfer speed in stress fibers and overall cell migration speed.

4.3 Front-to-rear dynamics of retrograde actin and myosinIIa

After analyzing the cytosolic transfer of actin and stress fiber dynamics of myosin IIa in migrating cell system, front-to-rear dynamics of the two stress fiber components were examined.

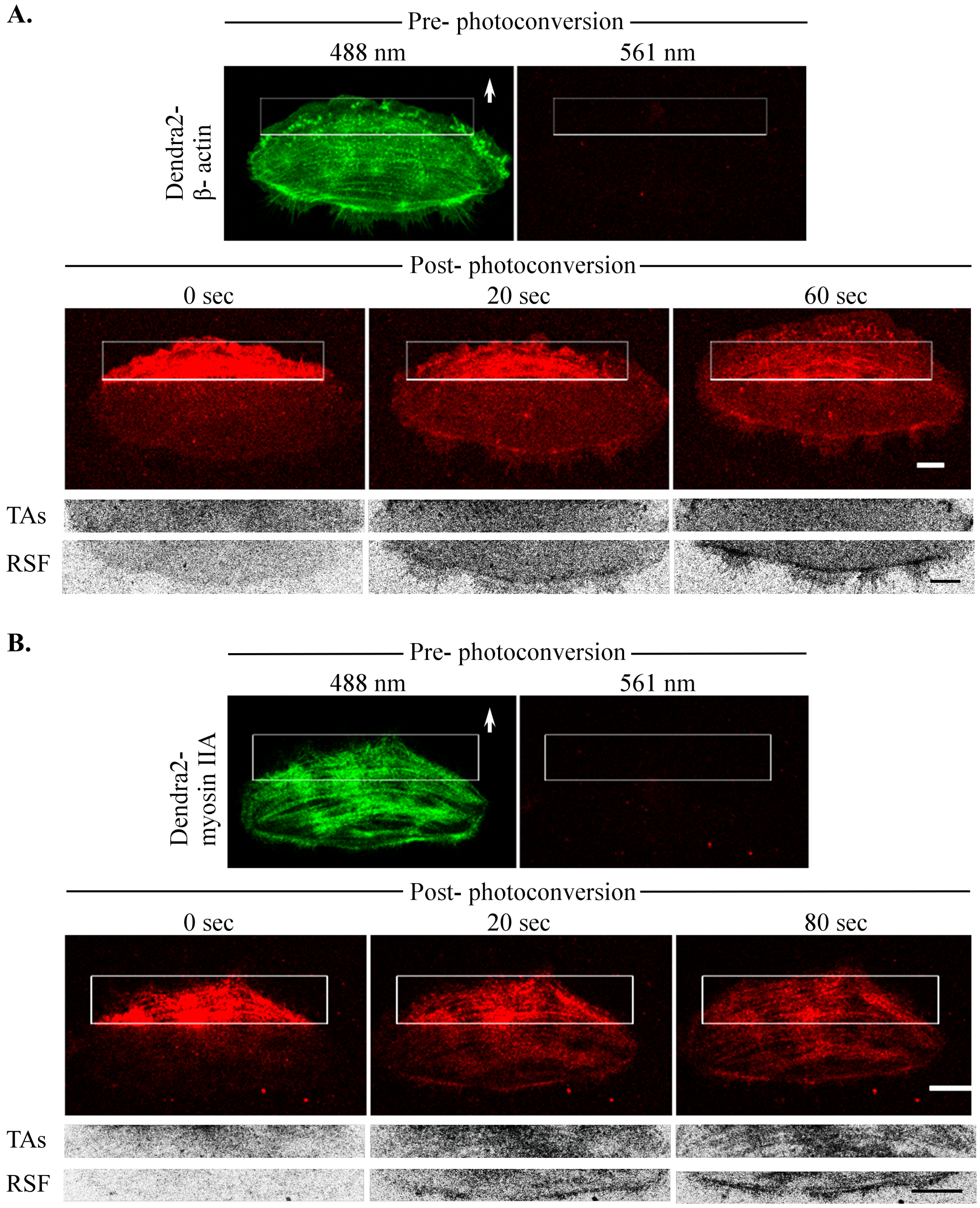

Figure 4.17: Examining the front-to-rear dynamics of retrograde actin and myosin. White rectangle indicates the area of photoconversion at frontal part of the cell. (A) Dynamics of retrograde actin in transverse arcs (TAs) and rear-end stress fiber (RSF). (B) Dynamics of retrograde myosin II in TAs and RSF. Scale bars = 10 μm.

Since high retrograde flow in the cell areas between lamellipodium and lamella is responsible for continuous inward transport of actin and myosin [95], molecular pools in the anterior and posterior lamellipodial regions were labelled by dendra2 photoconversion. Post-conversion molecular movement from lamella region to the cell rear were then analyzed. Actin and myosin pools at the frontal parts of the cell were photoconverted as indicated by white rectangle in figure 4.17.

Spontaneous transfer of post-converted actin and myosin molecules towards the cell rear was observed. To quantify post-conversion assembly of actin and myosin into the transverse arcs and rear-end stress fiber, overtime intensity profiles of respective stress fiber bundles were obtained using the fiber tracking tool described in an earlier section (section 2.6). Magnified cell areas in figure 4.17 were tracked and analyzed for transverse arcs and rear-end SFs. Gray values along the length of stress fibers were then averaged at each time point. Intensity curves in figure 4.18 represents the normalized overtime incorporation of actin and myosin II into transverse arcs and rear-end stress fiber by front-to-rear retrograde flow.

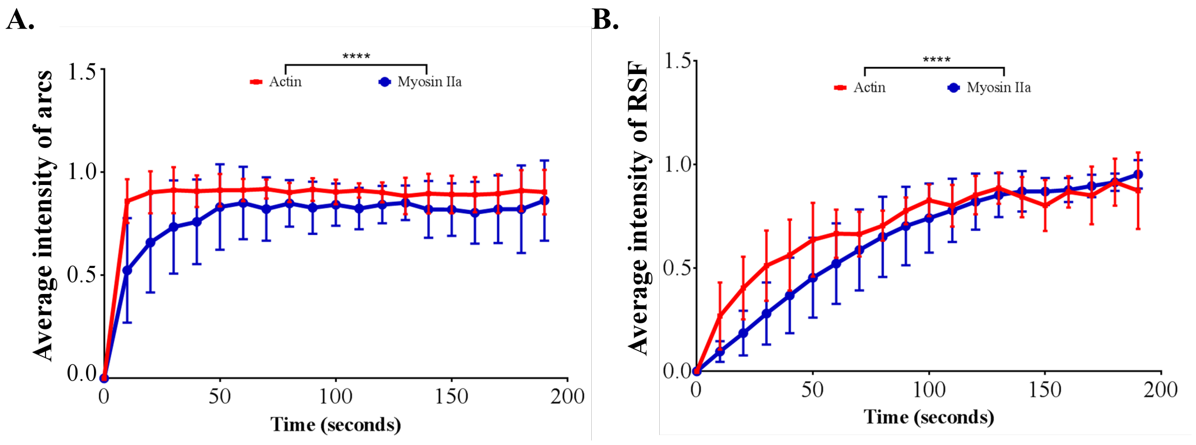

Figure 4.18: Average intensity profile of post-conversion retrograde actin (red curve) and myosin (blue curve) assembly in (A) transverse arcs and (B) rear-end SF bundle. Error bars indicates the spread of data points (SD). Average intensity changes for the two stress fiber elements were found to be statistically different with p-value < 0.0001, using paired t-test. N = 10 analyzed stress fibers in each category from 10 cells.

The retrograde actin assembly curve for transverse arcs displayed a rapid initial increase, with no further overtime increment. The observed rapid increase was due to the immediate post-conversion actin transfer seen at 20 sec time point in the transverse arc area (figure 4.17). The plateau region of the actin TA curve (figure 4.18-A) implies no subsequent actin incorporation into these stress fiber bundles. Myosin II on the other hand displayed a gradual incorporation into transverse arcs, which can be seen as increasing post-conversion intensity curve in figure 4.18 (A). Unlike arcs, retrograde actin assembly curve of rear-end stress fiber bundle however displayed a continuous overtime increment (figure 4.18-B), indicating their turnover for retrograde actin. Myosin II in the rear-end stress fiber displayed linearly increasing overtime intensity. The linear increase was mainly due to the gradual assembly of the retrograde myosin II into this SF bundle (also seen in the image sequence in figure 4.17). Additionally, statistical significance of actin and myosin II assembly into arcs and rear-end SF was tested using a two-tailed paired t-test (explained in section 2.8.1), where the obtained p-value of < 0.05 indicates that the two data sets were significantly different.

Similar to earlier observation with actin transfer, different actin turnover behaviors were also observed for retrograde actin exchange in transverse arcs and rear-end stress fiber, where the latter SF bundle was observed to be highly dynamic. Presented in figure 4.19 are kymographic representations of distinct retrograde actin turnover behaviors of TAs and RSF.

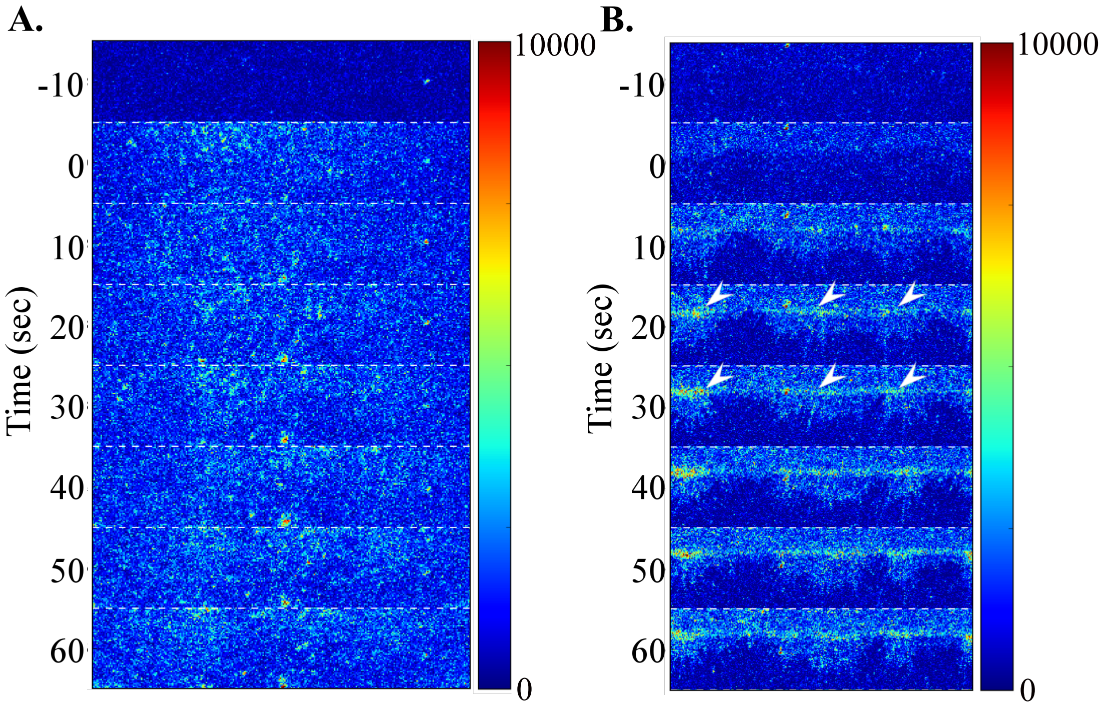

Figure 4.19: Kymographic representation of retrograde actin turnover in (A) transverse arcs and (B) rear-end stress fiber bundle. White arrow heads indicate specific actin incorporation locations at rear-end fiber, co-localizing with the rear retraction fiber trails (white arrow heads).

The front-to-rear actin assembly into the rear-end fiber can be seen as strong actin signal build up locations (indicated by white arrow head) observed at stress fiber locations co-localizing with attached retraction fibers (indicated by yellow arrows) at rear cell edge. Similar to previous observation (figure 4.19), inward flow through retraction trails were seen to transport actin molecules to the rear-end fiber. Transverse arcs on the other hand display no significant incorporation of retrograde actin molecules, as only a diffused actin signal was observed in post-conversion imaging with no specific localization at transverse arc areas (figure 4.19-A).

In compliance with previous observations in section 4.2.1, retrograde myosin IIa transfer was observed along the microfilament network, displaying front-to-rear movement against the stress fiber network. Both transverse arcs and the rear-end stress fiber outlined myosin II incorporation by front-to-rear retrograde movement of myosin units. Presented in figure 4.20 are kymographic representations of retrograde myosin II turnover in TAs and RSF.

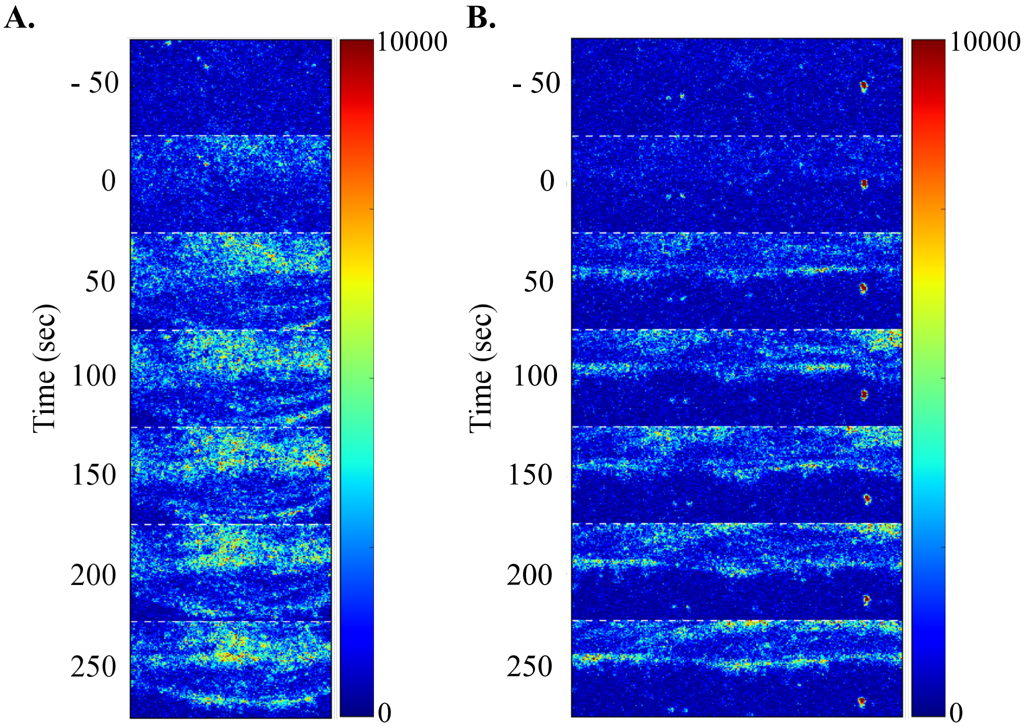

Figure 4.20: Kymographic representation of retrograde myosin II turnover in (A) transverse arcs and (B) rear-end stress fiber bundle.

The observed faster post-conversion myosin incorporation into TAs in comparison with RSF (seen at time point 50 sec in figure 4.20) was due to their relatively proximal residency to the front photo-labelled region of the cell.

Overall, results in this section revealed major turnover differences between the two stress fiber types. High actin turnover was observed in the rear-end SFs, whereas transverse arcs displayed no significant turnover. Actin filaments in transverse arcs might therefore be very stable. Turnover in rear-end ventral SFs was further observed to occur at discrete SF locations, indicating the involvement of distinctly (non-uniformly) available turnover sites. These observations are an indication of spacially separated turnover characteristics, i.e. differential stress fiber turnover at cell front (arcs) and rear (rear-end SF). Myosin II turnover was observed in both stress fiber types, indicating that myosin turnover activity is independent of stress fiber actin turnover. Moreover, myosin II transfer speed was found to correlate to the overall cell migration speed, where fast moving cells displayed faster myosin transfer along the SFs compared to slow migrating cells.

CHAPTER 5

Results: Focal adhesion dynamics

Migration involves formation of front protrusion and adhesion, in coordination with contraction and detachment of the rear. Myosin II mediated contractions of SFs causes maturation of associated focal adhesions (FAs) at cell front. Smaller focal complexes evolve into larger adhesions by stacking additional FA molecules (explained in section 1.3.2). Several times FA turnover, maturation and dissociation has been considered to be important for directional movement of a cell, but how the tendency of exchanging bound/unbound molecules is affected at different stages of their lifetime starting from young to mature till their disassembly stage, still remains unidentified. In this chapter, vinculin turnover behavior of different FAs is presented, where the dynamics of spatially separated nascent, mature and disassembling FAs are compared. Using dendra2 mediated photoconversion, vinculin turnover behavior of different FAs is reported here. Additionally, sub-regional FA turnover of resident vinculin is presented.

5.1 Exchange dynamics of rear end FAs changes prior to disassembly

Migrating keratinocytes display small sized nascent focal complexes at lamellipodial tips and larger mature adhesions in the lamella and cell body region. Figure 5.1 depicts a migrating keratinocyte labelled with GFP-vinculin, highlighting different types of focal adhesion complexes. Nascent focal adhesions (NFAs) are located at the lamellipodial tips of the cell. They are formed newly in cell protrusions and appear as small aggregates of vinculin (seen in 0 sec inset in figure 5.1). Nascent FAs are then observed to grow larger in size and intensity. Mature adhesions (MFAs) are found in the lamella region of the cell and appear as stable complexes. They do not show any significant overtime growth or changes in size. Disassembling or sliding focal adhesions (SFAs) on the other hand are found at the cell's rear edge. These adhesions are disassembled upon cellular contractions at rear, in order to mediate detachment of rear from the extracellular matrix. These FAs exclusively display an inward sliding prior to their disassembly. This sliding of adhesions at cell rear can be seen in the magnified insets in figure 5.1.

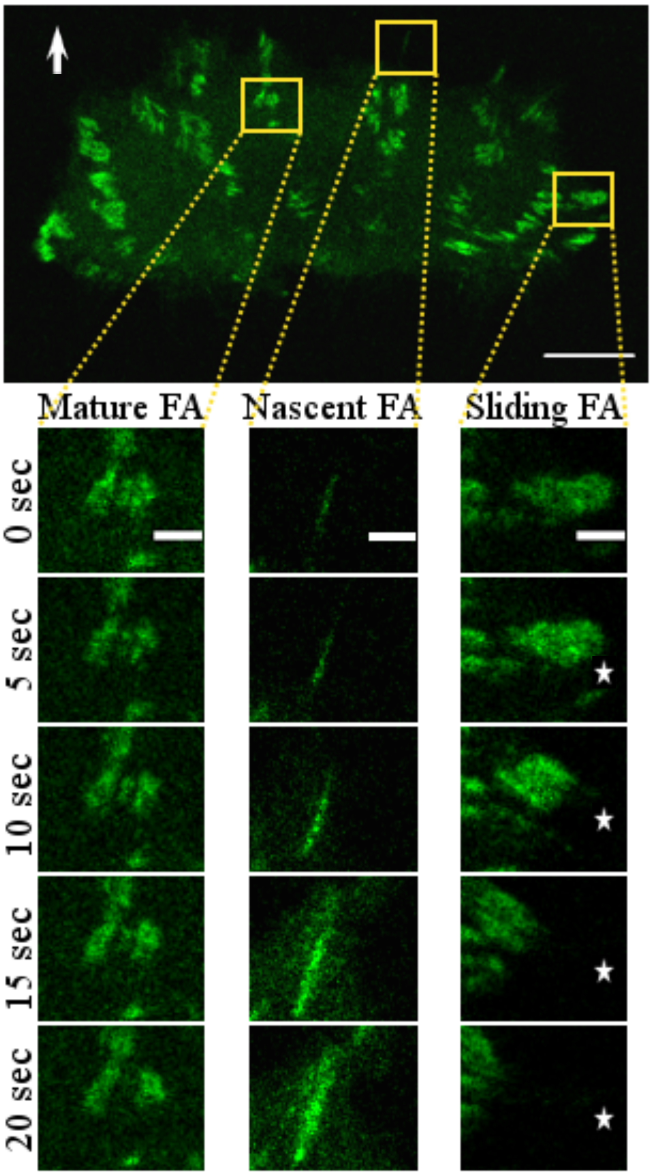

Figure 5.1: A migrating human keratinocyte labelled with GFP-vinculin. White arrow indicates the direction of migration. Nascent adhesions are located at lamellipodial tips and undergo overtime growth in their size and intensity. Mature adhesions are located in the lamella region and display no significant changes in size. FAs at cell rear undergoes disassembly by adhesion sliding as the rear cell end retracts. The magnified insets demonstrate the three types of FA complexes. White star in the sliding FA inset can be used as a reference point to comprehend the FA sliding motion. Scale bar of the cell is 10 μm and for insets is 2 μm.

Dynamic focal adhesions are needed for fast and efficient cell migration. They are unstable complexes that undergo continuous exchange of their bound constituents with unbound counterparts [38]. There is therefore a need for constant recycling and transport of unbound adhesion constituents, to constantly feed the FA turnover process. The recycling process is mainly coordinated by vesicle transport, for trans-membrane FA domains [33][34][135][35] or simple cytosolic diffusion transfer, for internal FA plaque components [38].

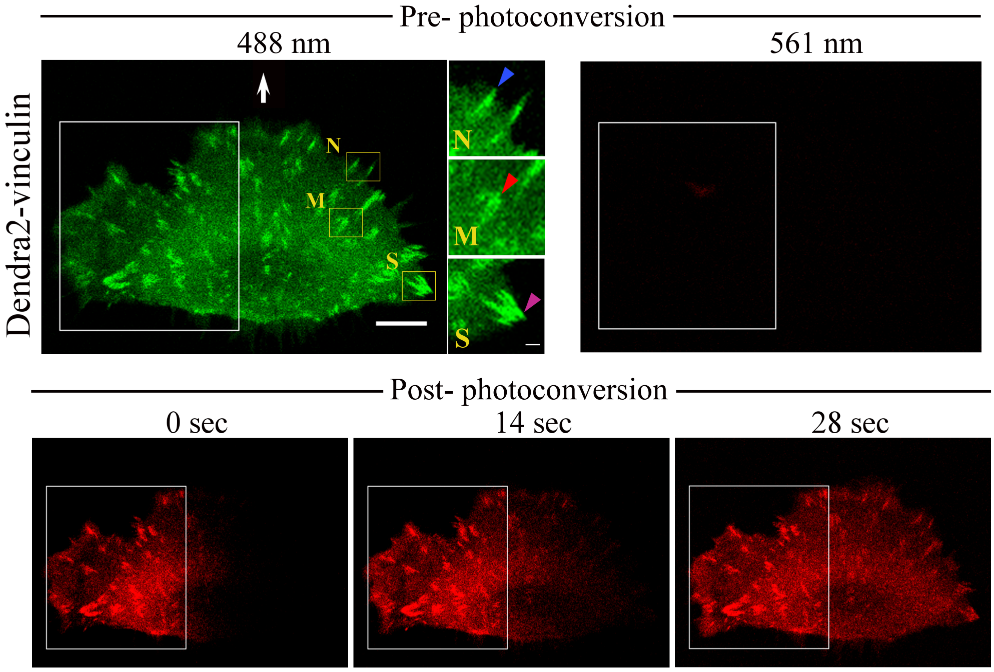

Figure 5.2: Photoconversion of vinculin to monitor FA turnover. The image sequence for photoconverted vinculin indicates its cytosolic re-distribution and subsequent incorporation into the FAs. Scale bar = 10 μm. The insets marked with yellow indicates nascent (N), mature (M) and sliding (S) FAs. Scale bars in insets = 2 μm.

In order to study the turnover of FA plaque components at different stages of their lifetime, photoconversion of dendra2 coupled to vinculin was used to label the bound and cytosolic vinculin counterparts in one half of the cell. Dendra2 photoconversion was performed in the cellular region enclosed by white rectangle in figure 5.2. Post-conversion vinculin was observed to re-distribute out of the photoconversion ROI, into the non-converted parts of the cell and was ultimately incorporated into adhesion complexes (figure 5.2). Newly formed nascent FAs at frontal tips were chosen for analysis, which were fully developed and stable in shape/size and fluorescence intensity. Mature FAs located in the cell body were chosen for analysis. All selected FAs were equidistant from the photoconversion ROI. The overtime assembly of post-conversion vinculin into discrete FAs was then quantified to measure real-time vinculin turnover rates in different FA complexes. The overtime vinculin incorporation into FAs was quantified using a segmentation routine developed by Georg Dreissen, ICS7-FZJ (detailed in section 2.9). This image processing tool enabled frame-to-frame identification of individual focal adhesion complexes in an image sequence, by tracking overtime changes to their sizes and overall position displacements (if any). Using this tool, the temporal increase in absolute intensity values of post-conversion vinculin into nascent, mature and disassembling FAs, located in the non-converted part of the cell were extracted and analyzed.

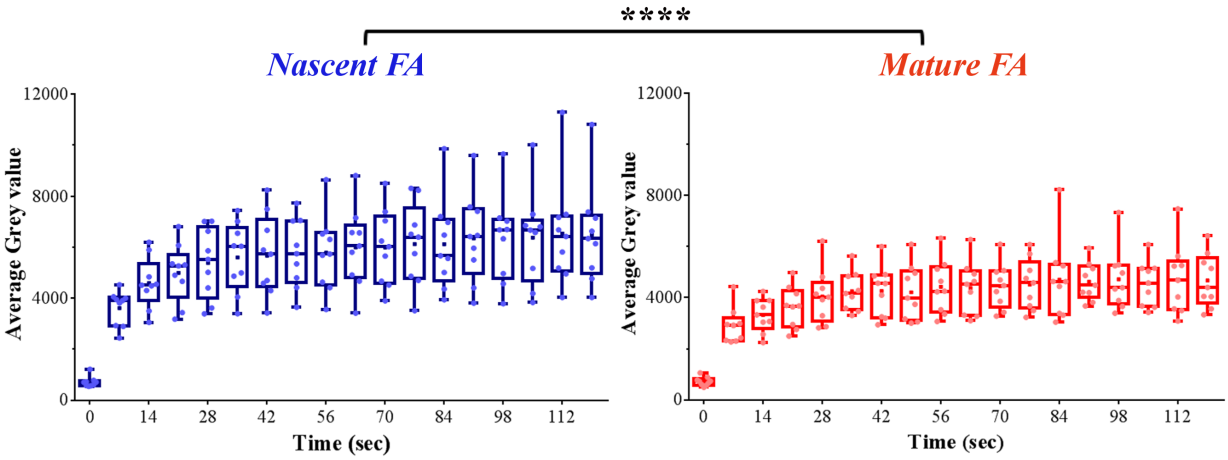

Figure 5.3: Box plot representing the absolute intensity profiles of post-conversion vinculin assembly into nascent and mature FAs from 12 different cells (n=20). Whiskers indicate the maximum and minimum intensities in the sample population and dashes represent median of the grouped data. Significance was tested using a two-tailed paired t-test (****P value < 0.0001).

The post-conversion vinculin assembly profiles of nascent and mature FAs were then represented in form of overtime intensity curves. Figure 5.3 displays a box plot representation for the two FA types, where blue and red curves represents nascent and mature FAs respectively. Using these curves, the absolute rate of post-conversion vinculin assembly into the two FA types was calculated using the following expression:

$$Average\ \ rate\ \ of\ \ vinculin\ \ turnover = \frac{Change\ \ in\ \ intensity}{Time}$$

The calculated average rates of vinculin assembly were 70 $\sec^{-1}$ for nascent FAs and 48 $\sec^{-1}$ for mature FAs. Nascent adhesions were therefore observed to have ~1.5 fold higher vinculin turnover rate as compared to mature adhesions.

Also, statistical significance of collected data sets (from 12 different cells) for nascent and mature FAs was tested using a paired t-test (explained in section 2.8.1). The choice of performing a t-test was based on the normal distribution of collected data sets for post-conversion vinculin incorporation in the two FA types. Shown in figure 5.4 are the frequency distribution histograms and box plot representation (in respective insets) of analyzed data sets for nascent (in blue) and mature (in red) FAs. A Gaussian function was fitted to respective distribution histograms to check for normal distributions of analyzed groups.

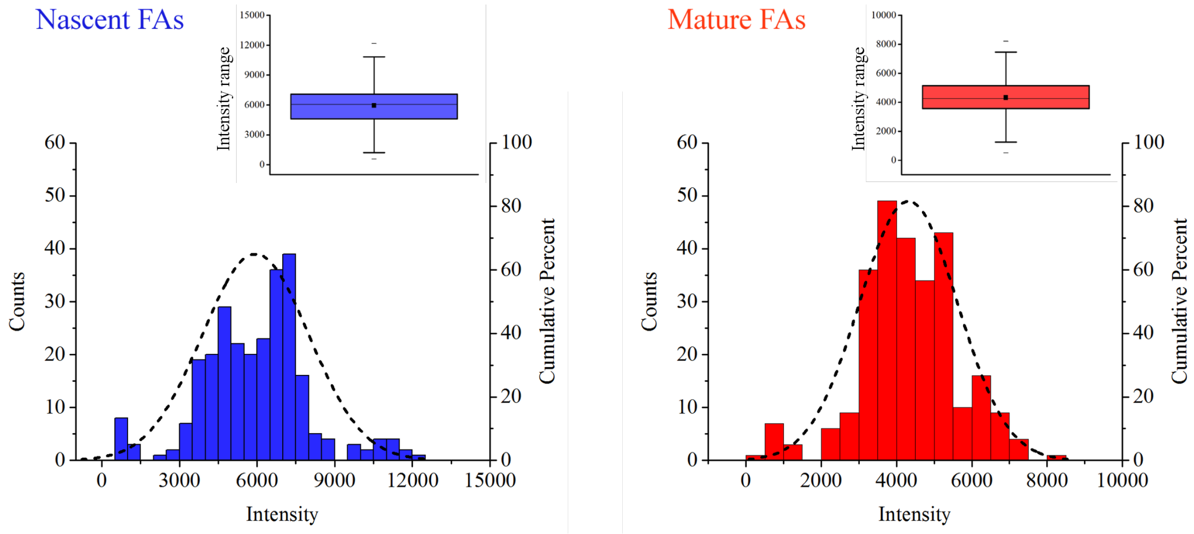

Figure 5.4: Histograms showing frequency distribution of analyzed data sets for post-conversion vinculin intensity profiles of nascent (in blue) and mature (in red) FAs from 12 different cells (n=20). Dotted lines displays the respective guassian fit functions to indicate normal distribution of collected data. The insets display data distribution in form of a box plots, with central line and black dot representing the respective median and mean.

Two-tailed paired t-test was performed using the GraphPad Prism software and a p-value of < 0.0001 was obtained. P-value of < 0.05 therefore indicates that the two FA types are significantly different and the observed difference is not by chance.

Further, post-conversion vinculin incorporation into sliding FAs, which undergo disassembly at cell rear was examined. FAs at cell rear, which were still stable at the time of photo-conversion but started sliding within 50-60 sec after conversion, were considered for analysis. Adhesions which displayed sliding at the time of photo-conversion, were excluded. Intensity profiles for disassembling FAs were quantified in the same manner using FA segmentation and tracking, as done previously for nascent and mature FAs. These FAs were identified by their tendency to undergo inward sliding prior to disassembly (as shown in figure 5.1). Vinculin turnover in these adhesion complexes were compared with previously analyzed nascent and mature FAs. Intensity profiles of three FA groups are presented in figure 5.5 as overtime intensity curves. The turnover behavior of sliding FAs was observed to acquire two phases (violet curve in figure

5.5). The first slow turnover phase, with absolute post-conversion vinculin incorporation rate of 52.3 sec^{-1}, similar to that observed for mature FAs. A faster vinculin incorporation phase, with absolute post-conversion vinculin incorporation rate of 64 sec^{-1} was observed, comparable to that observed for nascent FAs.

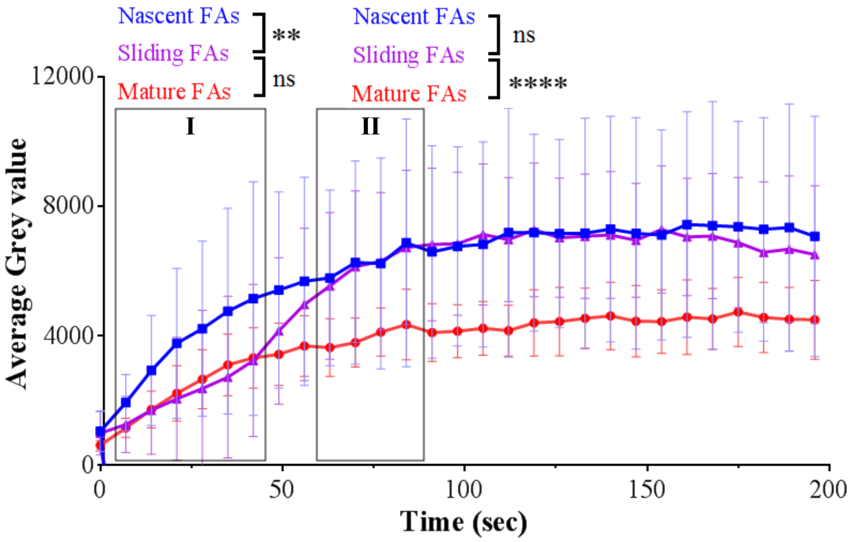

Figure 5.5: Intensity curve of post-conversion vinculin incorporation in sliding FAs in comparison with nascent and mature FAs. Error bars indicate the error in SD. Using the statistical ANOVA follow up test, sliding FAs displayed turnover similarity with mature FAs in their initial turnover phase (I) and with nascent FAs in the later turnover phase (II). N = 17 for NFAs, 12 for MFAs, 17 for SFAs.

Statistical ANOVA test (explained in section 2.8.2) was then performed to test for statistical significance of observed differences between the analyzed FA groups. Nascent, mature and sliding FAs in the (I) first as well as (II) second turnover phase of sliding FAs were found to be significantly different, with p-value of <0.0001 in both phases. Which indicated that at least one of the three FA groups was significantly different in both turnover phases. In order to statistically identify similarities and differences between these FA groups, Tukey's statistical comparison test (explained in section 2.8.2) was performed. The tested FA groups were arranged into pairs and their respective mean differences were analyzed. This test was performed separately for turnover phases I and II, where the test groups were arranged into three pairs i.e. nascent-mature (NFA-MFA), sliding-mature (SFA-MFA) and sliding-nascent (SFA-NFA). Plot in figure 5.6 presents the calculated differences between group means, using pair-wise Tukey's comparison in phase I (fig 5.6A) and phase II (fig 5.6B) of sliding FA turnover.

Blue data points in figure 5.6 represents the difference mean values of respective pairs with 95% confidence interval. In phase I (figure 5.6 A), the calculated q-ratio for the pair sliding-mature

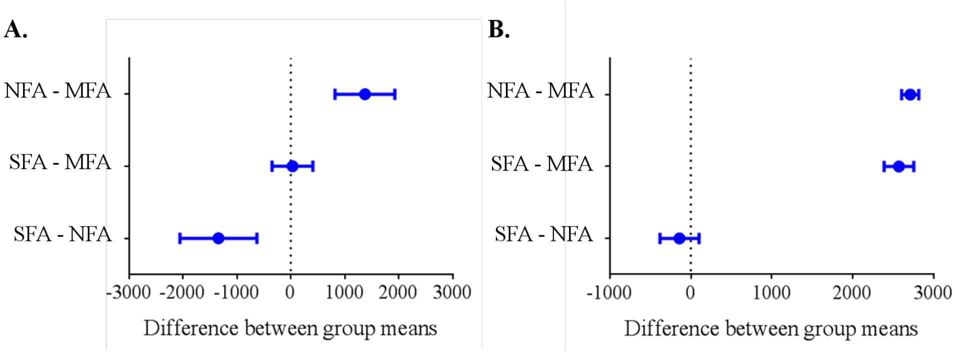

Figure 5.6: Plot representing the pair-wise differences between populations of nascent (NFA), mature (MFA) and sliding (SFA) focal adhesions, using Tukey's test. Pair-wise comparison of FA groups was performed in (A) early phase I and (B) late phase II of sliding FA turnover. Error bars indicates the standard error.

(SFA-MFA) was 0.350 and for the pair sliding-nascent (SFA-NFA) was 7.831. The small q-ratio of SFA-MFA pair indicated closely related turnover behaviors of SFAs and MFAs in the early SFA turnover phase I. In phase II (figure 5.6 B), the q-ratio for the pair sliding-mature (SFA-MFA) was 64.47 and for the pair sliding-nascent (SFA-NFA) was 2.663. Here, the small q-ratio of SFA-NFA pair indicated closely related turnover behaviors of SFAs and NFAs in the late SFA turnover phase II.

Together, the post-conversion intensity profiles of different FA types, in combination with statistical test and the grouped mean test confirmed distinct vinculin plaque turnover behaviors. The two phased turnover behavior of sliding FAs was observed, where an initial slow vinculin turnover phase was seen to change to a faster turnover phase prior to their disassembly at rear cell edge.

5.2 Asymmetric vinculin turnover in sliding FAs

Following the observation of overall molecular turnover in different FA complexes, specific sub-regional vinculin turnover sites within different adhesion complexes were identified. The rapid event of post-conversion vinculin incorporation into single FA complexes was monitored. Using normal cLSM imaging system, the fastest scanning time achieved for simultaneous acquisition of two imaging channels was ~9 seconds per frame. With this acquisition limit, it was not possible to monitor the faster process of vinculin transfer to the non-converted cell areas and its subsequent assembly into adhesion complexes. In order to improve the temporal ans spatial resolution of vinculin transfer and assembly, Fast AiryScan imaging system (explained in section 2.4.2) was used.

The popularly known sub-regional distinction within a FA complex is identified as distal and proximal end regions. The two ends are assigned according to their orientation with respect to the cell's nucleus, where the proximal FA end is towards the nucleus (or cell body) and the distal FA end is towards the cell periphery. On a functional level, the two FA ends differ in their attachment to the actin cytoskeleton, with proximal ends being firmly bound to actin filaments [99]. The sub-regional vinculin turnover differences, at distal and proximal ends of respective adhesion complexes are presented in this section. Figure 5.7 presents overtime incorporation of post-conversion vinculin into individual nascent (N), mature (M) and sliding (S) adhesions, where post-conversion vinculin turnover can be visualized as red signal spots overlaying the green focal adhesion complexes (indicated in magnified insets). White line in 0 sec inset marks the long axis of respective focal adhesion complexes, highlighting their distal (d) and proximal (p) ends.

Uniform assembly of post-conversion vinculin was observed along the long axis of nascent and mature adhesions. This can be seen as a homogeneous overlay of post-conversion vinculin (red) signal onto nascent and mature adhesion complexes (N and M insets in figure 5.7). No significantly preferred sub-regional distal or proximal sites for post-conversion vinculin incorporation were observed. Sliding FA (S) on the other hand displayed distal-proximal differences in post-conversion vinculin incorporation. Distal end sub-region of these adhesion complexes were seen to incorporate post-conversion vinculin first (indicated in 20 and 27 sec time points by arrow head in figure 5.7). A subsequent incorporation was then observed in the central sub-region (34 sec time point in figure 5.7), followed by proximal sub-regional incorporation (41 sec time point in figure 5.7). Additionally, the post-conversion vinculin incorporation can be seen on kymographic representation of the three FA types, along their long axis in figure 5.8.

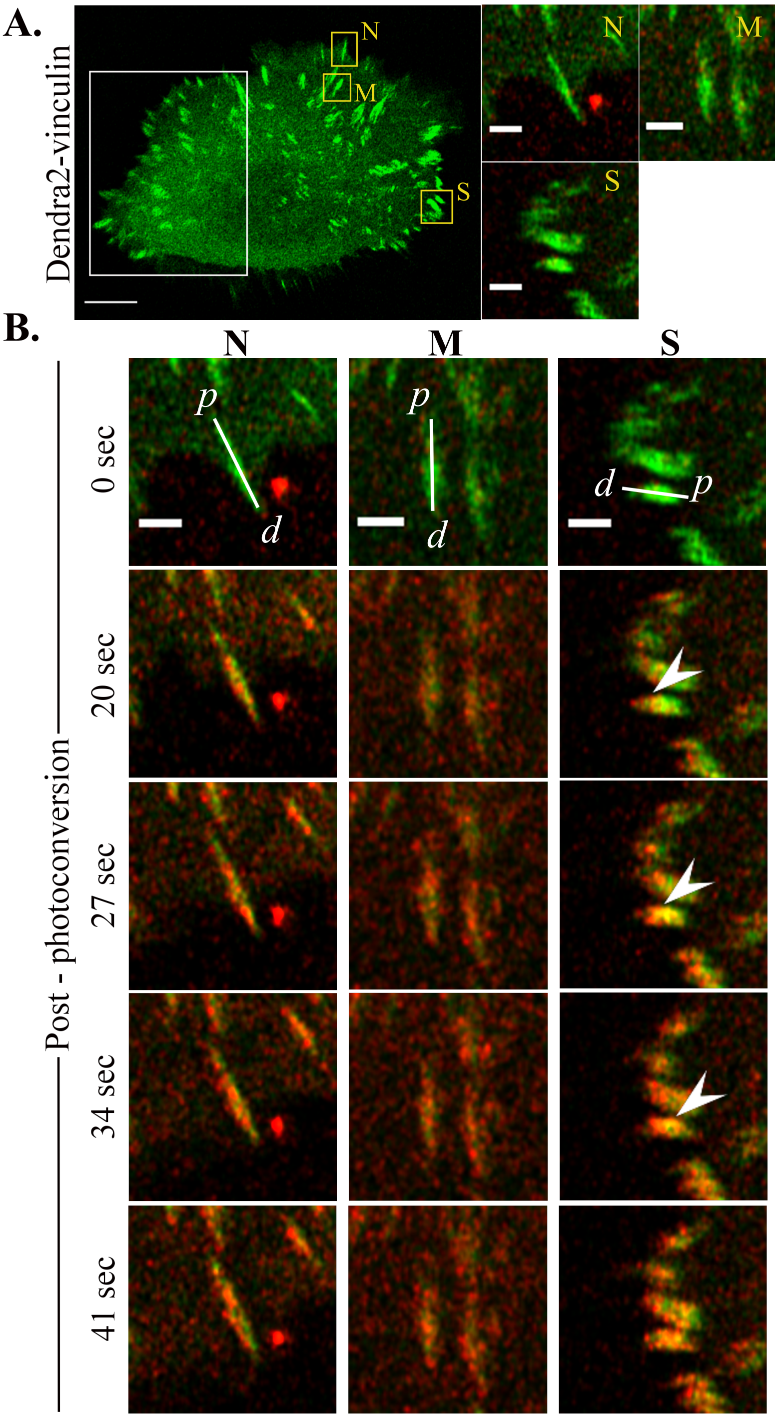

Figure 5.7: High resolution visualization of post-conversion vinculin assembly into different FAs. The magnified insets in B presents different types of FAs, where N, M and S represents the nascent, mature and sliding FAs respectively. White line along the FAs in 0 sec inset marks the distal (d) and proximal (p) ends of FA complexes. The arrow heads indicate asymmetric vinculin turnover in sliding FAs. Scale bar of image = 10 μm. Scale bar of insets = 2 μm.

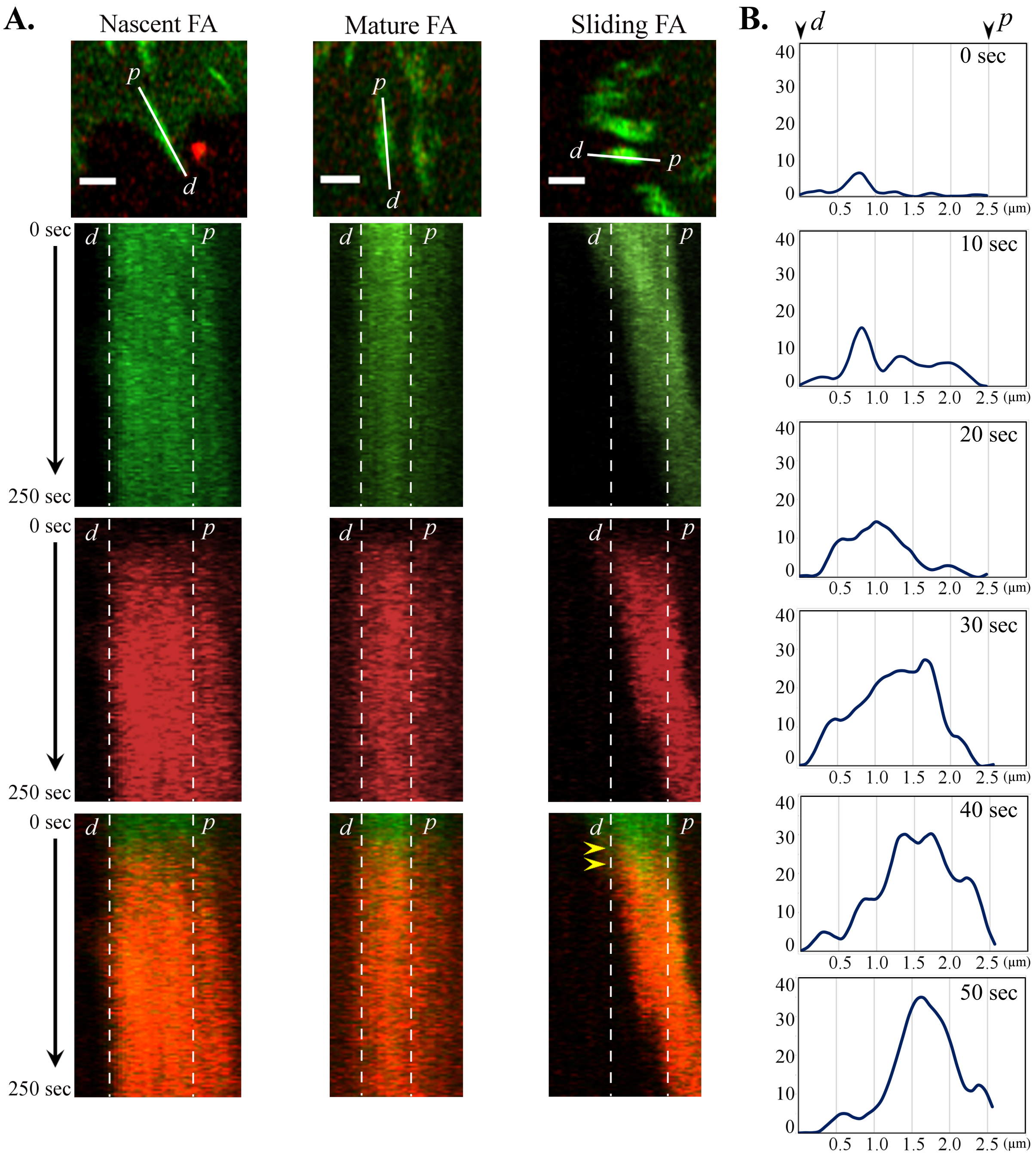

Figure 5.8: (A) Kymographic representation of post-conversion vinculin assembly into nascent, mature and sliding FAs. White line along FA long axis in the inset represents the analyzed region for kymographs. Scale bar of inset = 2 μm. Dotted lines represent the respective distal (d) and proximal (p) ends. (B) Overtime intensity curves of vinculin assembly in sliding FA along the d-p axis.

Kymographs were built along the long axis of FAs (white line along the FA axes) using the kymograph builder plugin, available in ImageJ. The green and red kymographs represents the respective native and photo-converted dendra2 forms. The left dotted line represents the distal FA end and right dotted line represents the proximal end on respective kymographs. The distal-proximal end boundaries were assigned according to respective FA sizes at 0 sec time point shown in figure 5.7. A homogeneous assembly of post-conversion vinculin was observed in nascent and mature FAs, as simultaneous red signal assembly at distal and proximal ends (on overlay kymographs in figure 5.8). Additionally, nascent FA elongation at their proximal end was observed. This can be seen on the overlay kymograph as overtime extension of post-conversion signal, away from the dotted proximal end boundary. Mature FAs however, display no preferred elongating end.

In sliding FAs, the post-conversion vinculin signal was observed to incorporate first at distal end sub-region (indicated by yellow arrow heads in the overlay kymograph in figure 5.8), as compared to the opposite proximal end region. The temporal delay of post-conversion vinculin incorporation at proximal end of sliding FA can be seen on the overtime intensity curves in figure 5.8-B, where incorporation signal along the length of distal-proximal axis is presented. Initial signal at distal end appeared at 10 sec as a peak at 0.7 μm. Further broadening of the peak (from 20 sec to 40 sec) indicates overtime post-conversion signal assembly into central and ultimately proximal FA sub-regions. With time, significant drop in distal end signal peak was observed (40 sec and 50 sec time points) due to the inward sliding of FA complex (explained in section 1.3.3) in the proximal end direction. The observed sub-regional distal-proximal turnover differences indicated polarized plaque protein assembly-disassembly on opposite FA ends of sliding FAs.

CHAPTER 6

Discussion

Understanding the fundamentals behind cell migration is of major interest, as it forms the framework for a large set of biological processes such as immune responses, tissue formation, maintenance of multicellular organisms and cancer malignancies. Also, cell motility is one of the main events associated with the process of wound healing, where epidermal cells migrate into the wounded area resulting in its closure. In this work, real time turnover dynamics of pivotal components of cell contractile machinery and focal adhesion complexes was studied in migrating human epidermal keratinocytes (nHEKs). Using dendra2 photoconversion to label sub-cellular molecular populations, the post-conversion movement of molecules into the non-converted cell areas was measured and their localizations were quantified.

6.1 Discussion of results on microfilament dynamics

Epithelial cell migration requires coordinated displacement of two actin rich compartments at the cell's leading edge namely, lamellipodium and lamella. Actin arcs in the lamella region serves as structural element that mediate spatial and temporal coordination between the two frontal compartments and drives directional cell motility [136]. Contractile arrays of actin arcs are bundled by myosin II [63] and generate tractions required for forward propulsion of the cell. The ventral rear-end stress fiber bundle is on the other hand, responsible for preventing protrusion formation at trailing edge and determines rear contractions [3], which in turn determines the overall rate of cell's migration by facilitating cell body translocations [137].

In this work, the turnover behavior of transverse arcs and rear-end ventral stress fibers were monitored in motile nHEKs. Diffusion driven cytosolic actin transfer into TAs and rear-end ventral SF areas was observed. Further, stress fiber actin turnover was observed, where the rear-end SF was found to be relatively more dynamic than transverse arcs. Observed in figure 4.7, the temporal increase of post-conversion actin assembly into rear-end SF is indicative of involved actin turnover. The distinct actin turnover behaviors of arcs and rear-end SF were also observed for front-to-rear actin retrograde flow (section 4.3), where unlike transverse arcs actin incorporation into ventral RSF was observed. In-vitro studies revealed the role of actin-depolymerizing factor (ADF)/cofillins in increasing depolymerization at pointed filament ends, providing a pool of actin monomers, thereby enhancing filament turnover. ADF/cofilins were additionally found to severe actin filaments, providing more number of filament ends for monomer addition [138]. The depolymerization and filament severing activity of ADF/cofilin was further verified to contribute in regulation of cell morphology and migration, where cells silenced for ADF/cofilin demonstrated significantly reduced motility [139]. The observation of post-conversion actin incorporation into rear-end SF is in line with a previously established stress fiber associated actin exchange, where a chemical reaction between the mobile interfibrillary (cytosolic) actin units and immobile stress fiber localized actin, led to rapid FRAP recovery of bleached stress fiber areas [36] [37], highlighting the involvement of mobile actin pools in filament turnover.

Actin turnover in rear-end SFs was identified in this work to occur at discrete locations on the rear-end stress fiber, indicating multiple turnover sites along the SF. Since ventral stress fibers originates from a bundling process, where transverse arcs stack together as they get retrogradely displaced towards the cell rear [63] [140], ventral SFs consists of multiple short actin fragments. Individual actin fragments will therefore have their own plus and minus ends, which will act as discrete actin assembly-disassembly sites. The multiple plus and minus sites might therefore establish the observed discrete turnover sites on the rear-end SF. As shown on the stress fiber kymograph in figure 4.8, rear-end SF displayed anterograde flow sites at proximal ends of membrane threads called retraction fibers, close to the rear cell edge. Anterograde flow of actin nodules through retraction fiber trails was observed to supply free actin material, additional to the available cytosolic mobile actin pool, for rear-end SF turnover (figure 4.9). The flow appeared as actin nodules of different sizes and resembled small actin aggregates. Usually one actin nodule per retraction thread was observed with their periodic appearance. They appeared spontaneously close to the distal end of the retraction fiber and moved continuously inwards. On reaching the proximal end of the thread, the flowing actin nodules stalled to form a bright aggregate close to the rear-end SF location, where they finally fused into the stress fiber bundle. These observations are similar to the inward flow of actin material seen in retraction fibers formed during mitosis in PtK2 cells [141]. Here, dense actin carrying nodules were seen to travel towards the cell body, along the long retraction fibers formed as a result of cellular rounding, marking the start of mitosis. Additionally, as transverse arcs undergo centripetal movement towards the cell rear, the formed ventral stress fibers are known to be more contractile. Increased contractility of new ventral SFs is further known to inactivate the VASP signaling molecule (catalyzes actin polymerization), thereby inhibiting actin polymerization process at cell rear [140]. The observed post-conversion incorporation of actin into the rear-end ventral stress fiber in this work, is therefore not influenced by formation of new actin structures but rather is majorly due to active assembly-disassembly cycles of actin units in the constituent filaments of rear-end ventral SFs.

Retrograde flow of actin at cell front, away from the cell border, have been known to contribute to the assembly of transverse arcs at the lamellipodia-lamella interface region. Inward flow of pre-formed small actin filaments, from fast flowing lamellipodial region reaches the lamella, where retrograde actin flow gets retarded [63]. Actin filaments from the retrograde flow, as well as from the anterograde flow [76] from the cell body, are arranged into transverse arcs at the convergence zone i.e. at the lamellipodia-lamella interface region. In this work, the observed anterograde flow of actin nodules through rear retraction fibers and their ultimate assimilation into the rear-end SF, proposes the existence of a similar flow and assembly mechanism, where actin materials are transported anterogradely to reach the stress fiber and gets arranged into the rear-end SF. These inward flowing actin materials could either be free actin monomers, aggregates or pre-formed mini-filaments. Unlike at the lamellipodium-lamella interface where actin flow leads to the formation of new stress fibers, at cell rear the flowing actin appears to contribute only in stress fiber turnover and maintenance.

Actin stress fibers consisting of indivudual filaments with alternating polarity [62] are bundled together by myosin II and α-actinin cross-linking molecules, displaying mutually exclusive binding along stress fibers and are arranged as periodic units [63]. Myosin II head domain displacement towards barbed ends of actin filaments facilitates required filament sliding and contractions [74] for migration. In this work, myosin II mobility in stress fibers of migrating cells was examined. Myosin II was observed to displace along both SF types i.e. actin transverse arcs and the rear-end ventral SF. Previous studies have shown existance of actin filament associated myosins as bipolar assemblies, which consists of multiple individual myosin filaments stacked together [68] [142]. These filament stacks once formed are not stable, rather they undergo continuous splitting into smaller filament stacks or undergo expansion by addition of new myosin molecules [143] [142]. Additionally, single myosin molecules located at the surface of bipolar assemblies have a tendency to undergo detachment from their native assemblies. Dissociation of these surface myosins is known to be faster than those present at the assembly core [144]. Also, myosin turnover in actin associated filament assemblies in lamella region is thought to be driven by mass action mechanism [76], which states that the direction of assembly/disassembly reaction is decided by the local concentration of monomers and polymers. If myosin monomer concenration is high, the reaction proceeds in assembly direction (to maintain the chemical equillibrium) and if the polymer concentration is higher, disassembly reaction prevails. In this work, the observed myosin signal propagation along SFs might involve a similar mechanism. The close proximity of myosin assemblies in SFs might cause dissociation of monomers, which will in turn increase the local concentration of monomeric myosin and thus triggers association on the neghbouring assembly. The surface myosin monomers therefore, undergo cycles of transient dissociation from their parent assemblies followed by rapid re-binding to the adjacent assembly. This detachment and re-binding of individual myosin molecules, together with myosin stack splitting could be responsible for generating the observed mobility of myosin II along the length of SFs seen in section 4.2.1 and 4.3, which gives an overall appearance of group of myosin molecules following each other. Also, the front-to-rear movement of myosin II observed in section 4.3, indicates that myosins can switch between different actin tracks. However, due to high network density of actin filaments, especially in transverse arcs region, it was impossible to identify individual actin tracks for myosin movement and to determine if these tracks were single or multiple actin filaments.

Double headed myosin II based contractions are believed to maintain high order bundling of actin filaments in the posterior part of the cell, which helps break adhesive interactions between the cell rear and the substrate by generating mechanical stresses [121] [106]. Myosin IIa knockdown studies resulted in complete loss of stress fibers and produced significantly lower traction forces at cell rear as compared to wild type cells [145]. This has established the role of myosin IIa in stress fiber formation and force generation for rear end detachment. Also, retraction of the cell rear is considered to be the rate limiting step in forward displacement of cells [121]. In this work, considering stress fiber myosin IIa transfer speed as an independent factor, dependence of cell migration speed was tested (figure 4.16). The observed ~56% dependence between the two factors suggests the role of stress fiber myosin II turnover rate in regulation of cell migration speed. It is however unclear at this point, if the dependence is regulated directly or indirectly by myosin II.

6.2 Discussion of results on focal adhesion dynamics

Directional cell migration requires formation of new adhesion points at front, followed by their maturation, attachment to the actin cytoskeleton and de-adhesion at cell rear. Specific phosphorylation of vinculin is thought to be crucial for cell spreading [103] and FA maturation [146]. Src-kinase mediated tyrosine phosphorylation (at Y^{100} and Y^{1065}) causes structural unfolding of vinculin, which then triggers its binding to the FA plaque complex [94]. Indeed, a gradient of phosphorylated vinculin at Tyr^{1065} was observed in FAs of migrating cells, with front FAs having the highest degree of phosphorylation, compared to FAs close to the cell body with lower degree of vinculin phosphorylation [146]. Additionally, specific mutations at Tyr^{1065} have reported a reduced FA turnover of vinculin [146]. These evidences directly indicate a strong dependence of vinculin residency in FA complexes on its tyrosine phosphorylation state, with high degree of phosphorylation corresponding to greater turnover rate.

In the current work, the altering vinculin turnover behavior of FAs was observed as they transition from nascent to mature to disassembling adhesion state. Previous attempts have validated the dynamic character of FA resident vinculin, where its turnover in nascent and mature focal adhesion sites has been reported to be a rapid process [147]. Seen in figure 5.3, vinculin exchange rates were found to be dissimilar for nascent and mature FAs, with nascent FAs being ~1.5 times more dynamic. This observation is in line with the previously stated front-to-rear Tyr phosphorylation gradient, where high phosphorylation state of vinculin at cell front leads to its higher turnover in nascent adhesions.The less dynamic mature adhesions located in the cell body, were further found to evolve into highly dynamic complexes upon finding themselves close to the rear cell edge (section 5.1). Based on the known facts about specific tyrosine kinases and their roles in phosphorylation of vinculin, the transformed high vinculin turnover in disassembling FAs could arise due to activation of certain Tyr kinases at cell rear edge. In migrating cells, its rear is known to induce maximum actomyosin generated contractile forces [73] to facilitate cell body translocations and this high tension region might therefore contain highly active mechanosensitive tyrosine kinases, which could maintain a higher degree of Tyr phosphorylation and thus a higher vinculin turnover state of adhesions located close to the rear cell edge.

In contrast to stationary adhesions assembled at front of a migrating cell, those at the retracting cell edges, move relative to the substratum. This sliding behavior of adhesions at cell rear is suggested to be important for rear edge retraction and migration [148] [149] [150]. Since efficiency of cell migration is determined by the ability of rear retraction [151], degree of FA sliding limits the overall migration speed. Sliding phenotype of rear FAs is identified so far as polarized renewal of trans-membrane integrin molecules, with continuous loss of integrins from distal ends of sliding FAs and recruitment of new ones at their proximal ends [107]. Myosin light chain phosphorylation at highly retracting cell rear induces low affinity states of integrins to facilitate de-adhesion and rear retraction [152] [153] [154]. These implications on FA sliding are made depending on the observed morphological changes, however the underlying regulatory mechanisms are still unknown. Also, the sliding phenotype has been examined so far only through the trans-membrane integrin domains but what happens to the interior FA plaque complex proteins is not yet determined. In this work, polarized turnover of vinculin plaque protein in FA sliding was observed using photoconverted vinculin assembly into FAs as an indication of the ongoing FA plaque exchange. Turnover rates of sliding FAs were seen to undergo changes from a slow to a high turnover phase. Vinculin recruitment and stabilization in FAs is thought to be force dependent [155], where contractile forces generated by attached actin filaments maintains the vinculin molecule in a stretched conformation. Stretched molecular conformation of vinculin prevents internal folding and keeps the binding sites exposed, retaining its binding ability with other FA plaque proteins. Also, vinculin is elucidated to be held by a relatively lower force (weak attachment) in disassembling adhesions [156], which might enable rapid vinculin exchange. Force alterations around plaque vinculin might therefore determine the change of vinculin exchange rates as mature FAs begin to undergo disassembly.

Further, relatively higher turnover was observed at distal ends of sliding adhesions as compared to their proximal ends. The dissimilar plaque protein turnover between distal and proximal FA ends suggests a possibility that during polarized renewal of integrins, the overall plasticity of the complex is also affected. FA plaque at distal FA ends might turn relatively more flexible due to the rapid affinity change of integrin in this region and thus accounts for higher plaque protein turnover. Since vinculin residency in FAs is not restricted only to its interaction with integrins, there might be additional factors responsible for the observed polarized turnover. These could be the possible mechanisms underlying the observed polarized vinculin turnover in sliding FAs, however deeper examination of localized force-dependent structural changes to vinculin and the role of associated FA plaque proteins will be needed to establish precise turnover mechanisms.

6.3 Kinetic interpretation of stress fiber and focal adhesion dynamics

Based on established knowledge and experimental observations from this work, a schematic representation of stress fiber and focal adhesion turnover dynamics of actin and vinculin is presented in figure 6.1. Since the rear-end stress fiber bundle is composed of multiple actin filaments stacked together [63], actin turnover in rear-end SF could occur at available plus (+) and minus (-) ends of constituent filaments. The turnover rates at the two filament ends will however differ, where plus ends will undergo rapid incorporation of post-conversion actin as compared to minus ends (indicated by bold double headed arrows in figure 6.1). Additionally, actin filament associated adaptor molecule, vinculin, at focal adhesion sites also undergoes continuous binding-unbinding cycles.

In a migrating cell system, structural and mechanical properties depend strongly upon the relative turnover rates of stress fiber and focal adhesion components. The turnover rates participates in setting the pace of cell attachment-detachment cycle, cell shape changes and cell body translocations. Quantitative characterization of stress fiber and focal adhesion kinetics might

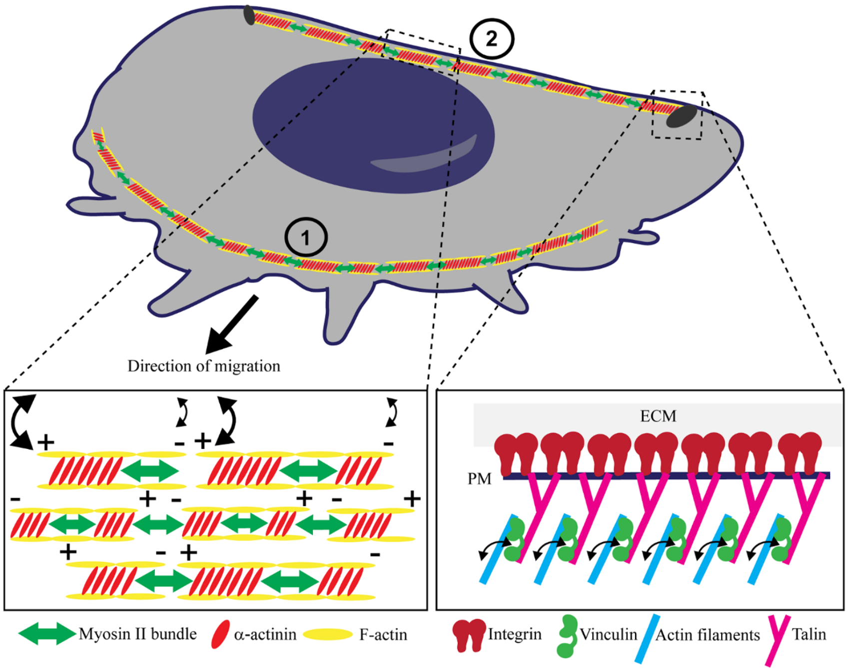

Figure 6.1: Schematic representation of stress fiber and focal adhesion turnover in migrating cells. Regions 1 and 2 indicates the respective transverse arcs and rear-end SF cell areas. Magnified insets emphasizes on the turnover specific sites of actin (left inset) and vinculin (right inset) in SFs and FAs. Two head arrows indicates prospected sites of component exchange and bold arrows at ′+′ actin fragment ends indicates higher turnover rates.

therefore be of interest, to define turnover rates that in turn will determine overall cell migration properties. To kinetically characterize the experimentally observed actin SF and FA turnover, the turnover process could be conceptualized as a simple binding process where free receptor sites on SFs and FAs are available for ligand binding. The *in-vitro* receptor-analyte binding model designed by Karlsson *et al.* [157] can serve as a reference for defining the SF and FA turnover rates in migrating cell systems. In this model, binding kinetics of an analyte to specific receptor was obtained using a Surface plasmon resonance (SPR) setup. The setup consisted of immobile receptor sites on a SPR surface and the analyte was introduced as a flowing solution (shown in figure 6.2). The overtime mass changes on the SPR surface due to analyte binding of the receptor were detected in form of a SPR response signal.

Similar to the analyte flow shown in figure 6.2, the post-conversion cytosolic transfer of actin and vinculin was observed as the primary mode of transfer of post-conversion fluorescence signal into the non-converted cell areas (results figure 4.7 and 5.2), followed by incorporation into discrete sub-cellular structures. The available plus and minus ends on SF bundles and vinculin sites on FAs could be considered as possible immobile receptor sites (turnover sites shown

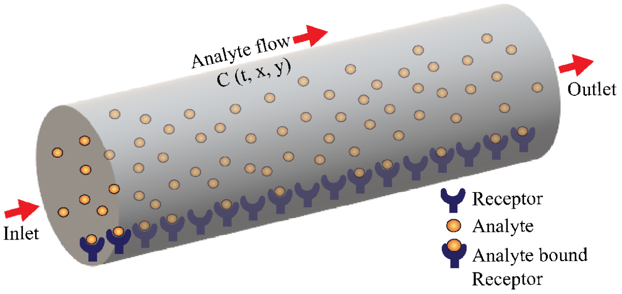

Figure 6.2: Schematic representation of flow setup used by Karlsson *et al.* [157], where the analyte was injected as a solution and binds to the immobile receptor components on the SPR surface.

in figure 6.1) and the respective cytosolic post-conversion molecular pools as the mobile analyte. Schematic diagram of post-conversion actin transfer is presented in figure 6.3, displaying analogy to the flow setup of Karlsson *et al.* [157]. Note that in the experiments described in this thesis, molecular transport was mostly due to diffusion whereas in the SPR setup, hydrodynamic flow is the predominant mechanism of transport. The turnover dynamics of actin SFs and vinculin in FAs can therefore be assumed to follow simple receptor-analyte binding kinetics.

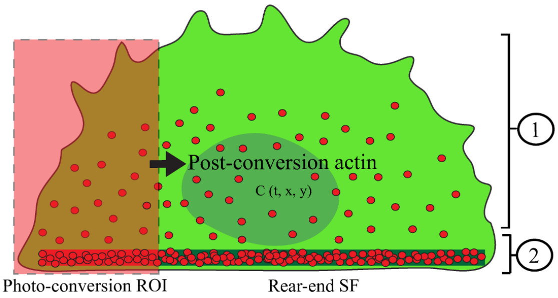

Figure 6.3: Schematic representation of post-conversion cytosolic actin transfer to the non-converted cellular regions. The cytosolic molecules acts as analytes and the rear-end SF acts as receptor sites. Regions 1 and 2 represents the respective cell areas for actin transverse arcs and rear-end stress fiber.

In fluorescence measurements, the intensity of fluorescent signal is proportional to the concentration of tagged species of interest [158]. If the cytosolic concentration of post-conversion moeity is C(t,x,y), where t is time and x,y are the coordinates where x is parallel to the direction of post-conversion flow and y is normal to the immobile SF/FA receptor sites. If I is the measured fluorescence signal intensity of SFs/FAs, then:

$$\frac{dI}{dt} \propto \frac{dC}{dt} \tag{6.1}$$

The post-conversion dendra2 signal distribution measured in the non-converted cell areas, is the principle indicator of the amount of analyte molecules transfered to receptor sites by cytosolic transfer. For defining the reaction kinetics, fluorescence signal intensities can be regarded as the measuring factor for molecular concentrations and the overtime intensity profiles of SFs/FAs will therefore represent the respective binding curves. In this case, considering the post-conversion cytosolic component as reactant A and the available receptor sites on SFs/FAs as reactant B, the binding reaction can then be written as follows:

$$[\mathrm{A}] + [\mathrm{B}] \underset{\mathrm{k}_d}{\overset{\mathrm{k}_a}{\rightleftharpoons}} [\mathrm{AB}]$$

where, k_a and k_d are the respective association and dissociation rate constants. The net rate of complex formation from A and B will depend on the concentration of available free analyte, unoccupied binding sites on the SFs/FAs and on stability of the formed complex;

$$\frac{d[AB]}{dt} = k_a[A][B] - k_d[AB] \tag{6.2}$$

Since the SFs and FAs are immobile components, [AB] will represent the concentration of bound analyte. From the proportionality equation 6.1, [AB] will be proportional to the measured fluorescence intensity I. The concentration of free receptor sites, [B], will be the difference between total and bound receptor concentration. Concentration of available receptors can be obtained indirectly from the saturated state, i.e. when all receptor sites are bound, leaving no room for additional analyte binding. For SFs/FAs, the plateau region of the intensitiy curves (figure 4.10 and 5.5) represents the saturated state with maximum signal intensity I_{max} and therefore (I_{max} - I) will be proportional to the free receptor concentration. During the binding reaction between free analyte and available binding sites at SFs/FAs, the concentration of cytosolic material will remain constant, as cell is a closed space and the overtime loss of contents will be negligible. Kinetics of the reaction will therefore depend majorly upon the overtime availability of binding sites and thus will follow pseudo first order kinetics. Since intensity is the measured quantity of the experimental data, using equation 6.1, equation 6.2 can be reformulated as:

$$\frac{dI}{dt} = k_aC(I_{max} - I) - k_dI \tag{6.3}$$

To evaluate the rate constants k_a and k_d, equation 6.3 can be rearranged to:

$$\frac{dI}{dt} = k_a C I_{max} - (k_a C + k_d) I \tag{6.4}$$

Once the value of C is known and I_{max} is obtained from the intensity curves at saturation state, the term k_a CI_{max} will be a constant. Using this equation, the measured fluorescence intensity, I, can be used directly. Rate constants can thereby be evaluated from a plot of dI/dt vs I, where the slope K will be:

$$K = k_a C + k_d \tag{6.5}$$

Upon varying the concentration (C) of available analyte, the association rate constant (k_a) can be readily obtained as the slope of a new plot of K vs C. To experimentally vary C in photo-conversion experiments, the photo-conversion ROI could be exposed to an altered UV exposure (e.g. more or less number of UV iterations). Altered iterations will enable altering the amount of photo-converted molecules and will ultimately vary the free analyte concentration.

This theoretical approach offers a preliminary method for quantification of stress fiber and focal adhesion turnover kinetics. Here, the experimentally measured fluorescence signal intensities can be used directly for quantitative analysis. Under real reaction conditions inside a cell, the measured fluorescence signal is however not just due to binding of available analyte molecules to the SFs/FAs. It is rather a combination of the binding and the transport process. The actual binding of post-conversion molecules to SFs/FAs can therefore be considered as a two step process, where transport of molecules is followed by their binding to the available receptor sites. Theoretical modelling performed by Myszka *et al.* [159] describes the effects of analyte transfer on the analyte-receptor binding kinetics. At high association rates, due to the effect of mass transfer, the concentration of analyte was shown to be available non-uniformly at the binding surface. Region of the surface closer to the source of analyte were observed to display faster binding compared to receptor regions farther away. The effect of mass transfer however became negligible as the association constant was lowered. Considering these results, the effect of mass analyte transfer will be pronounced on SF/FA turnover when the concentration of available binding sites will be higher, i.e. when the available plus and minus sites on actin SF bundle are higher.

In addition to mass transfer, migrating cells exhibits a highly dynamic internal environment where the cell contents are under continuous influence of flow and forces. Presence of myosin generated lateral pressure gradients, retrograde flow of molecules (especially actin) and interacting species might add to analyte transfer and ultimately affect SF/FA turnover. As observed in this work, the anterograde actin flow from the retraction fibers contributes significantly in rear-end SF turnover. The incoming actin material could be considered as an additional actin supply to the cytosolic analyte component. In other words, the anterograde actin supply will increase the local free actin concentration at cell rear, leading to non-uniform free analyte availability. Involvement of these biological aspects poses challenges for developing an elaborate and more efficient method for quantification of turnover kinetics.

CHAPTER 7

Conclusions and outlook

This work focusses on the turnover dynamics of cell migration components underlying microfilament and focal adhesion assemblies during persistent migration. Photoconversion of tagged fluorophore enabled selective labelling of molecular sub-populations and subsequent relocation of labelled molecules was monitored. The post-conversion intensity signal enabled monitoring respective molecular turnover processes, by simple tracking of redistributing signal.

In the first place, actin turnover in different stress fiber types was characterized. In the dynamic cellular environment, actin material is transported to stress fiber areas by rapid cytosolic transfer. The diffusive actin transfer shows no spatial differences, with central transverse arcs and rear ventral stress fiber regions showing similar cytosolic transfer. Following initial diffusive transfer, actin turnover behavior in transverse arcs and rear ventral stress fiber was found to be different. Arcs at central cell areas undergo no significant turnover for actin, demonstrating structurally stable actin filament bundles. Significant actin turnover was however observed in ventral stress fibers at cell rear, indicating continuous cycles of actin binding and release in these actin bundles. Plus, the rear ventral stress fiber is not under uniform turnover, but rather turnover occurs at discrete SF sites. The turning over actin in the rear ventral stress fiber is supplied by incoming actin materials via anterograde flow through retraction fiber trails. From previous knowledge of transverse arc assembly, where actin retrograde flow at cell front mediates stacking of pre-formed actin filaments, involvement of actin flow at cell rear in SF bundle turnover and maintainance was characterized. The differential turnover behaviors of the two spatially separated SFs indicates that in a migrating system, polarization of contractile machinery exists not just at structural and functional level, but also at the level of stress fiber dynamics. Even though the overall turnover behaviour in the rear-end SF was observed, it is still difficult to predict at this point, the exact mechanisms involved in such finely tuned regulation of spatially separated SF turnover process.

Stress fiber dynamics of the contractile motor protein, myosin II, was also monitored in this work. Transverse arcs and ventral SF associated myosin II was found to undergo displacements along the stress fiber network using actin bundles as scaffolds. Myosin dynamics along the SFs is not literal movement of myosin assemblies but is thought to be a consequence of dissociation-association cycles of individual myosin unit from/to the neighbouring assembly by mass action mechanism. Also, myosins were found to switch between different actin tracks. However, if the myosin movement tracks were single or multiple actin filaments, is not still evident. Further, the rate of myosin unit displacement along ventral stress fibers was found to correlate with the overall speed of cell's migration. Here, rates of myosin II turnover in stress fibers is thought to be possibly involved in migration speed regulation. However, identification of underlying regulations and factors involved, is an open question for future studies.

Further, turnover dynamics of focal adhesion resident adaptor protein, vinculin, was observed. Using experimental evidence and literature comparisons, focal adhesion exchange of bound vinculin was observed, indicating an exchange between dissolved molecular pool and bound FA resident pool. The overtime molecular exchange or the rate of vinculin exchange was observed to be higher in nascent adhesions as compared to mature adhesions. The rear disassembling focal adhesions were found to be unique, displaying a dual turnover behavior with an initial slow phase, followed by a faster turnover phase. The exchange rate in the early slow phase was similar to that of mature adhesions, however in fast turnover phase, exchange rate similar to nascent adhesions was observed. Once more, polarization at molecular turnover level in migrating cell system was characterized. Upon further analysis with improved temporal resolution, non-uniform vinculin turnover within disassembling FAs at cell rear was identified. Different exchange behaviors were observed at distal and proximal FA ends, where rapid turnover at distal FA ends was characterized. These results opens up a possibility that prior to polarized turnover of trans-membrane integrins in sliding FAs, the internal FA plaque turnover is polarized. Rapid distal plaque component turnover might make removal of associated integrins easier at this FA end as compared to the proximal side.

Overall, this work forms a basis for characterization of stress fiber and focal adhesion turnover and opens up the possibilities of kinetic quantification of these processes. In the field of life science research, where cell migration is a complex process underlying wound healing and cancer related studies, this work provides insights into cell polarity on a regulatory level and associated structural dynamics. This is a step forward in understanding the fundamentals behind the complex process of migration and offers challenges for future cell migration research.

Bibliography

[1] T. D. Coates, R. G. Watts, R. Hartman, and T. H. Howard. Relationship of F-actin distribution to development of polar shape in human polymorphonuclear neutrophils. *J. Cell Biol.*, 117(4):765–774, May 1992.

[2] S. H. Zigmond, H. I. Levitsky, and B. J. Kreel. Cell polarity: an examination of its behavioral expression and its consequences for polymorphonuclear leukocyte chemotaxis. *J. Cell Biol.*, 89(3):585–592, Jun 1981.

[3] P. T. Yam, C. A. Wilson, L. Ji, B. Hebert, E. L. Barnhart, N. A. Dye, P. W. Wiseman, G. Danuser, and J. A. Theriot. Actin-myosin network reorganization breaks symmetry at the cell rear to spontaneously initiate polarized cell motility. *J. Cell Biol.*, 178(7):1207–1221, Sep 2007.

[4] M. A. Lawson and F. R. Maxfield. Ca(2+)- and calcineurin-dependent recycling of an integrin to the front of migrating neutrophils. *Nature*, 377(6544):75–79, Sep 1995.

[5] S. J. Sullivan, G. Daukas, and S. H. Zigmond. Asymmetric distribution of the chemotactic peptide receptor on polymorphonuclear leukocytes. *J. Cell Biol.*, 99(4 Pt 1):1461–1467, Oct 1984.

[6] Y. L. Wang. Exchange of actin subunits at the leading edge of living fibroblasts: possible role of treadmilling. *J. Cell Biol.*, 101(2):597–602, Aug 1985.

[7] T. J. Mitchison and L. P. Cramer. Actin-based cell motility and cell locomotion. *Cell*, 84(3):371–379, Feb 1996.

[8] T. D. Pollard and G. G. Borisy. Cellular motility driven by assembly and disassembly of actin filaments. *Cell*, 112(4):453–465, Feb 2003.

[9] R. Ananthakrishnan and A. Ehrlicher. The forces behind cell movement. *Int. J. Biol. Sci.*, 3(5):303–317, Jun 2007.

[10] B. A. Maldonado and L. T. Furcht. Epidermal growth factor stimulates integrin-mediated cell migration of cultured human corneal epithelial cells on fibronectin and arginine-glycine-aspartic acid peptide. *Invest. Ophthalmol. Vis. Sci.*, 36(10):2120–2126, Sep 1995.

[11] R. S. Dise, M. R. Frey, R. H. Whitehead, and D. B. Polk. Epidermal growth factor stimulates Rac activation through Src and phosphatidylinositol 3-kinase to promote colonic epithelial cell migration. *Am. J. Physiol. Gastrointest. Liver Physiol.*, 294(1):G276–285, Jan 2008.

[12] R. N. Jorissen, F. Walker, N. Pouliot, T. P. Garrett, C. W. Ward, and A. W. Burgess. Epidermal growth factor receptor: mechanisms of activation and signalling. *Exp. Cell Res.*, 284(1):31–53, Mar 2003.

[13] M. A. Lemmon and J. Schlessinger. Cell signaling by receptor tyrosine kinases. *Cell*, 141(7):1117–1134, Jun 2010.

[14] D. B. Polk. Epidermal growth factor receptor-stimulated intestinal epithelial cell migration requires phospholipase C activity. *Gastroenterology*, 114(3):493–502, Mar 1998.

[15] R. L. Klemke, S. Cai, A. L. Giannini, P. J. Gallagher, P. de Lanerolle, and D. A. Cheresh. Regulation of cell motility by mitogen-activated protein kinase. *J. Cell Biol.*, 137(2):481–492, Apr 1997.

[16] M. Goke, M. Kanai, K. Lynch-Devaney, and D. K. Podolsky. Rapid mitogen-activated protein kinase activation by transforming growth factor alpha in wounded rat intestinal epithelial cells. *Gastroenterology*, 114(4):697–705, Apr 1998.

[17] M. Yebra, E. J. Filardo, E. M. Bayna, E. Kawahara, J. C. Becker, and D. A. Cheresh. Induction of carcinoma cell migration on vitronectin by NF-kappa B-dependent gene expression. *Mol. Biol. Cell*, 6(7):841–850, Jul 1995.

[18] A. Y. Chan, M. Bailly, N. Zebda, J. E. Segall, and J. S. Condeelis. Role of cofilin in epidermal growth factor-stimulated actin polymerization and lamellipod protrusion. *J. Cell Biol.*, 148(3):531–542, Feb 2000.

[19] M. M. Myat, S. Anderson, L. A. Allen, and A. Aderem. MARCKS regulates membrane ruffling and cell spreading. *Curr. Biol.*, 7(8):611–614, Aug 1997.

[20] J. M. Lewis, D. A. Cheresh, and M. A. Schwartz. Protein kinase C regulates alpha v beta 5-dependent cytoskeletal associations and focal adhesion kinase phosphorylation. *J. Cell Biol.*, 134(5):1323–1332, Sep 1996.

[21] S. Pastore, F. Mascia, V. Mariani, and G. Girolomoni. The epidermal growth factor receptor system in skin repair and inflammation. *J. Invest. Dermatol.*, 128(6):1365–1374, Jun 2008.

[22] J. V. Small and J. E. Celis. Filament arrangements in negatively stained cultured cells: the organization of actin. *Cytobiologie*, 16(2):308–325, Feb 1978.

[23] J. V. Small, G. Isenberg, and J. E. Celis. Polarity of actin at the leading edge of cultured cells. *Nature*, 272(5654):638–639, Apr 1978.

[24] M. D. Welch and R. D. Mullins. Cellular control of actin nucleation. *Annu. Rev. Cell Dev. Biol.*, 18:247–288, 2002.

[25] G. Letort, H. Ennomani, L. Gressin, M. Thery, and L. Blanchoin. Dynamic reorganization of the actin cytoskeleton. *F1000Res*, 4, 2015.

[26] C. S. Izzard and L. R. Lochner. Formation of cell-to-substrate contacts during fibroblast motility: an interference-reflexion study. *J. Cell. Sci.*, 42:81–116, Apr 1980.

[27] C. M. Regen and A. F. Horwitz. Dynamics of beta 1 integrin-mediated adhesive contacts in motile fibroblasts. *J. Cell Biol.*, 119(5):1347–1359, Dec 1992.

[28] C. Y. Chung, G. Potikyan, and R. A. Firtel. Control of cell polarity and chemotaxis by Akt/PKB and PI3 kinase through the regulation of PAKa. *Mol. Cell*, 7(5):937–947, May 2001.

[29] F. N. van Leeuwen, S. van Delft, H. E. Kain, R. A. van der Kammen, and J. G. Collard. Rac regulates phosphorylation of the myosin-II heavy chain, actinomyosin disassembly and cell spreading. *Nat. Cell Biol.*, 1(4):242–248, Aug 1999.

[30] A. P. Somlyo and A. V. Somlyo. Signal transduction by G-proteins, rho-kinase and protein phosphatase to smooth muscle and non-muscle myosin II. *J. Physiol. (Lond.)*, 522 Pt 2:177–185, Jan 2000.

[31] T. D. Pollard, L. Blanchoin, and R. D. Mullins. Molecular mechanisms controlling actin filament dynamics in nonmuscle cells. *Annu Rev Biophys Biomol Struct*, 29:545–576, 2000.

[32] Y. Fan, S. M. Eswarappa, M. Hitomi, and P. L. Fox. Myo1c facilitates G-actin transport to the leading edge of migrating endothelial cells. *J. Cell Biol.*, 198(1):47–55, Jul 2012.

[33] W. T. Chao and J. Kunz. Focal adhesion disassembly requires clathrin-dependent endocytosis of integrins. *FEBS Lett.*, 583(8):1337–1343, Apr 2009.

[34] E. J. Ezratty, C. Bertaux, E. E. Marcantonio, and G. G. Gundersen. Clathrin mediates integrin endocytosis for focal adhesion disassembly in migrating cells. *J. Cell Biol.*, 187(5):733–747, Nov 2009.

[35] M. G. Marquez, Y. R. Brandan, E. d. e. l. V. Guaytima, C. H. Pavan, N. O. Favale, and N. B. Sterin-Speziale. Physiologically induced restructuring of focal adhesions causes mobilization of vinculin by a vesicular endocytic recycling pathway. *Biochim. Biophys. Acta*, 1843(12):2991–3003, Dec 2014.

[36] T. E. Kreis, B. Geiger, and J. Schlessinger. Mobility of microinjected rhodamine actin within living chicken gizzard cells determined by fluorescence photobleaching recovery. *Cell*, 29(3):835–845, Jul 1982.

[37] S. A. Koestler, K. Rottner, F. Lai, J. Block, M. Vinzenz, and J. V. Small. F- and G-actin concentrations in lamellipodia of moving cells. *PLoS ONE*, 4(3):e4810, 2009.

[38] H. Wolfenson, A. Lubelski, T. Regev, J. Klafter, Y. I. Henis, and B. Geiger. A role for the juxtamembrane cytoplasm in the molecular dynamics of focal adhesions. *PLoS ONE*, 4(1):e4304, 2009.

[39] E. H. Egelman, N. Francis, and D. J. DeRosier. F-actin is a helix with a random variable twist. *Nature*, 298(5870):131–135, Jul 1982.

[40] A. Desai and T. J. Mitchison. Microtubule polymerization dynamics. *Annu. Rev. Cell Dev. Biol.*, 13:83–117, 1997.

[41] H. Herrmann, S. V. Strelkov, P. Burkhard, and U. Aebi. Intermediate filaments: primary determinants of cell architecture and plasticity. *J. Clin. Invest.*, 119(7):1772–1783, Jul 2009.

[42] A. G. Clark, O. Wartlick, G. Salbreux, and E. K. Paluch. Stresses at the cell surface during animal cell morphogenesis. *Curr. Biol.*, 24(10):R484–494, May 2014.

[43] P. W. Luther, H. B. Peng, and J. J. Lin. Changes in cell shape and actin distribution induced by constant electric fields. *Nature*, 303(5912):61–64, 1983.

[44] W. Kabsch, H. G. Mannherz, D. Suck, E. F. Pai, and K. C. Holmes. Atomic structure of the actin:DNase I complex. *Nature*, 347(6288):37–44, Sep 1990.

[45] B. Alberts, A. Johnson, J. Lewis, K. Raff, M.and Roberts, and P. Walter. *Molecular biology of the cell. 4th edn.* Ann Bot. 2003 Feb;91(3):401., 2003.

[46] T. D. Pollard. Measurement of rate constants for actin filament elongation in solution. *Anal. Biochem.*, 134(2):406–412, Oct 1983.

[47] M. H. Symons and T. J. Mitchison. Control of actin polymerization in live and permeabilized fibroblasts. *J. Cell Biol.*, 114(3):503–513, Aug 1991.

[48] J. H. Hartwig, G. M. Bokoch, C. L. Carpenter, P. A. Janmey, L. A. Taylor, A. Toker, and T. P. Stossel. Thrombin receptor ligation and activated Rac uncap actin filament barbed ends through phosphoinositide synthesis in permeabilized human platelets. *Cell*, 82(4):643–653, Aug 1995.

[49] S. Arber, F. A. Barbayannis, H. Hanser, C. Schneider, C. A. Stanyon, O. Bernard, and P. Caroni. Regulation of actin dynamics through phosphorylation of cofilin by LIM-kinase. *Nature*, 393(6687):805–809, Jun 1998.

[50] S. H. Zigmond. Actin cytoskeleton: the Arp2/3 complex gets to the point. *Curr. Biol.*, 8(18):R654–657, Sep 1998.

[51] L. M. Machesky and K. L. Gould. The Arp2/3 complex: a multifunctional actin organizer. *Curr. Opin. Cell Biol.*, 11(1):117–121, Feb 1999.

[52] L. M. Machesky, R. D. Mullins, H. N. Higgs, D. A. Kaiser, L. Blanchoin, R. C. May, M. E. Hall, and T. D. Pollard. Scar, a WASp-related protein, activates nucleation of actin filaments by the Arp2/3 complex. *Proc. Natl. Acad. Sci. U.S.A.*, 96(7):3739–3744, Mar 1999.

[53] R. D. Mullins, J. A. Heuser, and T. D. Pollard. The interaction of Arp2/3 complex with actin: nucleation, high affinity pointed end capping, and formation of branching networks of filaments. *Proc. Natl. Acad. Sci. U.S.A.*, 95(11):6181–6186, May 1998.

[54] M. D. Welch. The world according to Arp: regulation of actin nucleation by the Arp2/3 complex. *Trends Cell Biol.*, 9(11):423–427, Nov 1999.

[55] R. Rohatgi, L. Ma, H. Miki, M. Lopez, T. Kirchhausen, T. Takenawa, and M. W. Kirschner. The interaction between N-WASP and the Arp2/3 complex links Cdc42-dependent signals to actin assembly. *Cell*, 97(2):221–231, Apr 1999.

[56] K. LAKI, W. J. BOWEN, and A. CLARK. The polymerization of proteins; adenosine triphosphate and the polymerization of actin. *J. Gen. Physiol.*, 33(5):437–443, May 1950.

[57] S. K. Maciver and A. G. Weeds. Actophorin preferentially binds monomeric ADP-actin over ATP-bound actin: consequences for cell locomotion. *FEBS Lett.*, 347(2-3):251–256, Jun 1994.

[58] S. K. Maciver, B. J. Pope, S. Whytock, and A. G. Weeds. The effect of two actin depolymerizing factors (ADF/cofilins) on actin filament turnover: pH sensitivity of F-actin binding by human ADF, but not of Acanthamoeba actophorin. *Eur. J. Biochem.*, 256(2):388–397, Sep 1998.

[59] Tatyana M. Svitkina and Gary G. Borisy. Arp2/3 Complex and Actin Depolymerizing Factor/Cofilin in Dendritic Organization and Treadmilling of Actin Filament Array in Lamellipodia. *The Journal of Cell Biology*, 145(5):1009–1026, 1999.

[60] C. Le Clainche, D. Pantaloni, and M. F. Carlier. ATP hydrolysis on actin-related protein 2/3 complex causes debranching of dendritic actin arrays. *Proc. Natl. Acad. Sci. U.S.A.*, 100(11):6337–6342, May 2003.

[61] T. W. Anderson, A. N. Vaughan, and L. P. Cramer. Retrograde flow and myosin II activity within the leading cell edge deliver F-actin to the lamella to seed the formation of graded polarity actomyosin II filament bundles in migrating fibroblasts. *Mol. Biol. Cell*, 19(11):5006–5018, Nov 2008.

[62] L. P. Cramer, M. Siebert, and T. J. Mitchison. Identification of novel graded polarity actin filament bundles in locomoting heart fibroblasts: implications for the generation of motile force. *J. Cell Biol.*, 136(6):1287–1305, Mar 1997.

[63] Pirta Hotulainen and Pekka Lappalainen. Stress fibers are generated by two distinct actin assembly mechanisms in motile cells. *The Journal of Cell Biology*, 173(3):383–394, 2006.

[64] J. V. Small, K. Rottner, I. Kaverina, and K. I. Anderson. Assembling an actin cytoskeleton for cell attachment and movement. *Biochim. Biophys. Acta*, 1404(3):271–281, Sep 1998.

[65] A. B. Verkhovsky, T. M. Svitkina, and G. G. Borisy. Myosin II filament assemblies in the active lamella of fibroblasts: their morphogenesis and role in the formation of actin filament bundles. *J. Cell Biol.*, 131(4):989–1002, Nov 1995.

[66] W. E. Gordon. Immunofluorescent and ultrastructural studies of "sarcomeric" units in stress fibers of cultured non-muscle cells. *Exp. Cell Res.*, 117(2):253–260, Dec 1978.

[67] A. B. Verkhovsky and G. G. Borisy. Non-sarcomeric mode of myosin II organization in the fibroblast lamellum. *J. Cell Biol.*, 123(3):637–652, Nov 1993.

[68] M. Vicente-Manzanares, X. Ma, R. S. Adelstein, and A. R. Horwitz. Non-muscle myosin II takes centre stage in cell adhesion and migration. *Nat. Rev. Mol. Cell Biol.*, 10(11):778–790, Nov 2009.

[69] T. Wendt, D. Taylor, K. M. Trybus, and K. Taylor. Three-dimensional image reconstruction of dephosphorylated smooth muscle heavy meromyosin reveals asymmetry in the interaction between myosin heads and placement of subfragment 2. *Proc. Natl. Acad. Sci. U.S.A.*, 98(8):4361–4366, Apr 2001.

[70] B. Egan and J. R. Zierath. Exercise metabolism and the molecular regulation of skeletal muscle adaptation. *Cell Metab.*, 17(2):162–184, Feb 2013.

[71] M. J. Tyska and D. M. Warshaw. The myosin power stroke. *Cell Motil. Cytoskeleton*, 51(1):1–15, Jan 2002.

[72] P. L. Post, R. L. DeBiasio, and D. L. Taylor. A fluorescent protein biosensor of myosin II regulatory light chain phosphorylation reports a gradient of phosphorylated myosin II in migrating cells. *Mol. Biol. Cell*, 6(12):1755–1768, Dec 1995.

[73] J. Kolega. Cytoplasmic dynamics of myosin IIA and IIB: spatial 'sorting' of isoforms in locomoting cells. *J. Cell. Sci.*, 111 (Pt 15):2085–2095, Aug 1998.

[74] M. Vicente-Manzanares, J. Zareno, L. Whitmore, C. K. Choi, and A. F. Horwitz. Regulation of protrusion, adhesion dynamics, and polarity by myosins IIA and IIB in migrating cells. *J. Cell Biol.*, 176(5):573–580, Feb 2007.

[75] R. Rid, N. Schiefermeier, I. Grigoriev, J. V. Small, and I. Kaverina. The last but not the least: the origin and significance of trailing adhesions in fibroblastic cells. *Cell Motil. Cytoskeleton*, 61(3):161–171, Jul 2005.

[76] S. Schaub, S. Bohnet, V. M. Laurent, J. J. Meister, and A. B. Verkhovsky. Comparative maps of motion and assembly of filamentous actin and myosin II in migrating cells. *Mol. Biol. Cell*, 18(10):3723–3732, Oct 2007.

[77] A. Ponti, M. Machacek, S. L. Gupton, C. M. Waterman-Storer, and G. Danuser. Two distinct actin networks drive the protrusion of migrating cells. *Science*, 305(5691):1782–1786, Sep 2004.

[78] E. Zamir and B. Geiger. Molecular complexity and dynamics of cell-matrix adhesions. *J. Cell. Sci.*, 114(Pt 20):3583–3590, Oct 2001.

[79] B. Geiger, S. Yehuda-Levenberg, and A. D. Bershadsky. Molecular interactions in the submembrane plaque of cell-cell and cell-matrix adhesions. *Acta Anat (Basel)*, 154(1):46–62, 1995.

[80] R. Zaidel-Bar, M. Cohen, L. Addadi, and B. Geiger. Hierarchical assembly of cell-matrix adhesion complexes. *Biochem. Soc. Trans.*, 32(Pt3):416–420, Jun 2004.

[81] J. D. Humphries, P. Wang, C. Streuli, B. Geiger, M. J. Humphries, and C. Ballestrem. Vinculin controls focal adhesion formation by direct interactions with talin and actin. *J. Cell Biol.*, 179(5):1043–1057, Dec 2007.

[82] V. Petit and J. P. Thiery. Focal adhesions: structure and dynamics. *Biol. Cell*, 92(7):477–494, Oct 2000.

[83] N. Q. Balaban, U. S. Schwarz, D. Riveline, P. Goichberg, G. Tzur, I. Sabanay, D. Mahalu, S. Safran, A. Bershadsky, L. Addadi, and B. Geiger. Force and focal adhesion assembly: a close relationship studied using elastic micropatterned substrates. *Nat. Cell Biol.*, 3(5):466–472, May 2001.

[84] L. B. Case and C. M. Waterman. Integration of actin dynamics and cell adhesion by a three-dimensional, mechanosensitive molecular clutch. *Nat. Cell Biol.*, 17(8):955–963, Aug 2015.

[85] D. A. Lauffenburger and A. F. Horwitz. Cell migration: a physically integrated molecular process. *Cell*, 84(3):359–369, Feb 1996.

[86] B. M. Jockusch and M. Rudiger. Crosstalk between cell adhesion molecules: vinculin as a paradigm for regulation by conformation. *Trends Cell Biol.*, 6(8):311–315, Aug 1996.

[87] J. L. Coll, A. Ben-Ze'ev, R. M. Ezzell, J. L. Rodriguez Fernandez, H. Baribault, R. G. Oshima, and E. D. Adamson. Targeted disruption of vinculin genes in F9 and embryonic stem cells changes cell morphology, adhesion, and locomotion. *Proc. Natl. Acad. Sci. U.S.A.*, 92(20):9161–9165, Sep 1995.

[88] W. Xu, H. Baribault, and E. D. Adamson. Vinculin knockout results in heart and brain defects during embryonic development. *Development*, 125(2):327–337, Jan 1998.

[89] B. A. Danowski, K. Imanaka-Yoshida, J. M. Sanger, and J. W. Sanger. Costameres are sites of force transmission to the substratum in adult rat cardiomyocytes. *J. Cell Biol.*, 118(6):1411–1420, Sep 1992.

[90] J. L. Rodriguez Fernandez, B. Geiger, D. Salomon, and A. Ben-Ze'ev. Suppression of vinculin expression by antisense transfection confers changes in cell morphology, motility, and anchorage-dependent growth of 3T3 cells. *J. Cell Biol.*, 122(6):1285–1294, Sep 1993.

[91] R. P. Johnson and S. W. Craig. An intramolecular association between the head and tail domains of vinculin modulates talin binding. *J. Biol. Chem.*, 269(17):12611–12619, Apr 1994.

[92] C. Bakolitsa, D. M. Cohen, L. A. Bankston, A. A. Bobkov, G. W. Cadwell, L. Jennings, D. R. Critchley, S. W. Craig, and R. C. Liddington. Structural basis for vinculin activation at sites of cell adhesion. *Nature*, 430(6999):583–586, Jul 2004.

[93] T. Izard, G. Evans, R. A. Borgon, C. L. Rush, G. Bricogne, and P. R. Bois. Vinculin activation by talin through helical bundle conversion. *Nature*, 427(6970):171–175, Jan 2004.

[94] H. Chen, D. M. Cohen, D. M. Choudhury, N. Kioka, and S. W. Craig. Spatial distribution and functional significance of activated vinculin in living cells. *J. Cell Biol.*, 169(3):459–470, May 2005.

[95] A. Y. Alexandrova, K. Arnold, S. Schaub, J. M. Vasiliev, J. J. Meister, A. D. Bershadsky, and A. B. Verkhovsky. Comparative dynamics of retrograde actin flow and focal adhesions: formation of nascent adhesions triggers transition from fast to slow flow. *PLoS ONE*, 3(9):e3234, Sep 2008.

[96] A. del Rio, R. Perez-Jimenez, R. Liu, P. Roca-Cusachs, J. M. Fernandez, and M. P. Sheetz. Stretching single talin rod molecules activates vinculin binding. *Science*, 323(5914):638–641, Jan 2009.

[97] J. C. Friedland, M. H. Lee, and D. Boettiger. Mechanically activated integrin switch controls alpha5beta1 function. *Science*, 323(5914):642–644, Jan 2009.

[98] C. K. Choi, M. Vicente-Manzanares, J. Zareno, L. A. Whitmore, A. Mogilner, and A. R. Horwitz. Actin and alpha-actinin orchestrate the assembly and maturation of nascent adhesions in a myosin II motor-independent manner. *Nat. Cell Biol.*, 10(9):1039–1050, Sep 2008.

[99] H. Wolfenson, Y. I. Henis, B. Geiger, and A. D. Bershadsky. The heel and toe of the cell's foot: a multifaceted approach for understanding the structure and dynamics of focal adhesions. *Cell Motil. Cytoskeleton*, 66(11):1017–1029, Nov 2009.

[100] J. Golji, J. Lam, and M. R. Mofrad. Vinculin activation is necessary for complete talin binding. *Biophys. J.*, 100(2):332–340, Jan 2011.

[101] A. Bershadsky, A. Chausovsky, E. Becker, A. Lyubimova, and B. Geiger. Involvement of microtubules in the control of adhesion-dependent signal transduction. *Curr. Biol.*, 6(10):1279–1289, Oct 1996.

[102] E. Zamir, B. Z. Katz, S. Aota, K. M. Yamada, B. Geiger, and Z. Kam. Molecular diversity of cell-matrix adhesions. *J. Cell. Sci.*, 112 (Pt 11):1655–1669, Jun 1999.

[103] Z. Zhang, G. Izaguirre, S. Y. Lin, H. Y. Lee, E. Schaefer, and B. Haimovich. The phosphorylation of vinculin on tyrosine residues 100 and 1065, mediated by SRC kinases, affects cell spreading. *Mol. Biol. Cell*, 15(9):4234–4247, Sep 2004.

[104] D. J. Webb, J. T. Parsons, and A. F. Horwitz. Adhesion assembly, disassembly and turnover in migrating cells – over and over and over again. *Nat. Cell Biol.*, 4(4):97–100, Apr 2002.

[105] M. P. Sheetz. Cell migration by graded attachment to substrates and contraction. *Semin. Cell Biol.*, 5(3):149–155, Jun 1994.

[106] E. Crowley and A. F. Horwitz. Tyrosine phosphorylation and cytoskeletal tension regulate the release of fibroblast adhesions. *J. Cell Biol.*, 131(2):525–537, Oct 1995.

[107] C. Ballestrem, B. Hinz, B. A. Imhof, and B. Wehrle-Haller. Marching at the front and dragging behind: differential alphaVbeta3-integrin turnover regulates focal adhesion behavior. *J. Cell Biol.*, 155(7):1319–1332, Dec 2001.

[108] L. M. Pierini, M. A. Lawson, R. J. Eddy, B. Hendey, and F. R. Maxfield. Oriented endocytic recycling of alpha5beta1 in motile neutrophils. *Blood*, 95(8):2471–2480, Apr 2000.

[109] M. Ormo, A. B. Cubitt, K. Kallio, L. A. Gross, R. Y. Tsien, and S. J. Remington. Crystal structure of the Aequorea victoria green fluorescent protein. *Science*, 273(5280):1392–1395, Sep 1996.

[110] R. Heim, D. C. Prasher, and R. Y. Tsien. Wavelength mutations and posttranslational autoxidation of green fluorescent protein. *Proc. Natl. Acad. Sci. U.S.A.*, 91(26):12501–12504, Dec 1994.

[111] D. M. Chudakov, V. V. Belousov, A. G. Zaraisky, V. V. Novoselov, D. B. Staroverov, D. B. Zorov, S. Lukyanov, and K. A. Lukyanov. Kindling fluorescent proteins for precise in vivo photolabeling. *Nat. Biotechnol.*, 21(2):191–194, Feb 2003.

[112] V. Adam. Phototransformable fluorescent proteins: which one for which application? *Histochem. Cell Biol.*, 142(1):19–41, Jul 2014.

[113] Y. A. Labas, N. G. Gurskaya, Y. G. Yanushevich, A. F. Fradkov, K. A. Lukyanov, S. A. Lukyanov, and M. V. Matz. Diversity and evolution of the green fluorescent protein family. *Proc. Natl. Acad. Sci. U.S.A.*, 99(7):4256–4261, Apr 2002.

[114] N. G. Gurskaya, V. V. Verkhusha, A. S. Shcheglov, D. B. Staroverov, T. V. Chepurnykh, A. F. Fradkov, S. Lukyanov, and K. A. Lukyanov. Engineering of a monomeric green-to-red photoactivatable fluorescent protein induced by blue light. *Nat. Biotechnol.*, 24(4):461–465, Apr 2006.

[115] Evrogen (2006). Green-to-red photoswitchable fluorescent protein Dendra2- User manual. http://evrogen.com/products/dendra2/dendra2detaileddescription.shtml, 2006.

[116] V. Adam, K. Nienhaus, D. Bourgeois, and G. U. Nienhaus. Structural basis of enhanced photoconversion yield in green fluorescent protein-like protein Dendra2. *Biochemistry*, 48(22):4905–4915, Jun 2009.

[117] K. Nienhaus, G. U. Nienhaus, J. Wiedenmann, and H. Nar. Structural basis for photo-induced protein cleavage and green-to-red conversion of fluorescent protein EosFP. *Proc. Natl. Acad. Sci. U.S.A.*, 102(26):9156–9159, Jun 2005.

[118] G. U. Nienhaus, K. Nienhaus, A. Holzle, S. Ivanchenko, F. Renzi, F. Oswald, M. Wolff, F. Schmitt, C. Rocker, B. Vallone, W. Weidemann, R. Heilker, H. Nar, and J. Wiedenmann. Photoconvertible fluorescent protein EosFP: biophysical properties and cell biology applications. *Photochem. Photobiol.*, 82(2):351–358, 2006.

[119] I. Hayashi, H. Mizuno, K. I. Tong, T. Furuta, F. Tanaka, M. Yoshimura, A. Miyawaki, and M. Ikura. Crystallographic evidence for water-assisted photo-induced peptide cleavage in the stony coral fluorescent protein Kaede. *J. Mol. Biol.*, 372(4):918–926, Sep 2007.

[120] H. Mizuno, T. K. Mal, K. I. Tong, R. Ando, T. Furuta, M. Ikura, and A. Miyawaki. Photo-induced peptide cleavage in the green-to-red conversion of a fluorescent protein. *Mol. Cell*, 12(4):1051–1058, Oct 2003.

[121] P. Y. Jay, P. A. Pham, S. A. Wong, and E. L. Elson. A mechanical function of myosin II in cell motility. *J. Cell. Sci.*, 108 (Pt 1):387–393, Jan 1995.

[122] Thomas J. Fellers and Michael W. Davidson. Olympus Introduction to confocal microscopy National High Magnetic Field Laboratory The Florida State University Florida 32310, 2012.

[123] Carl Zeiss microscopy (2012). Confocal microscopy principle. https://www.zeiss.com/microscopy/int/products/confocal-microscopes/lsm-800-for-materials.html, 2012.

[124] J. Huff. The Airyscan detector from ZEISS: confocal imaging with improved signal-to-noise ratio and super-resolution. *Nature methods*, 12(6):1205, Dec 2015.

[125] L. A. Cameron, B. R. Houghtaling, and G. Yang. Fluorescent speckle microscopy. *Cold Spring Harb Protoc*, 2011(5):pdb.top106, May 2011.

[126] D. Kotsur, R. Leube, R. Windoffer, and J. Mattes. Active contour models for individual keratin filament tracking. volume 109-110, 2017.

[127] C. Tomasi and R. Manduchi. Bilateral filtering for gray and color images. In *Sixth International Conference on Computer Vision (IEEE Cat. No.98CH36271)*, pages 839–846, Jan 1998.

[128] N. Otsu. A Threshold Selection Method from Gray-Level Histograms. *IEEE Transactions on Systems, Man, and Cybernetics*, 9(1):62–66, Jan 1979.

[129] Rafael C. Gonzalez and Richard E. Woods. *Digital Image Processing (3rd Edition)*. Prentice-Hall, Inc., Upper Saddle River, NJ, USA, 2006.

[130] George J. Grevera. *Distance Transform Algorithms And Their Implementation And Evaluation*, pages 33–60. Springer New York, New York, NY, 2007.

[131] Chenyang Xu and J. L. Prince. Snakes, shapes, and gradient vector flow. *IEEE Transactions on Image Processing*, 7(3):359–369, March 1998.

[132] N. Hersch, B. Wolters, G. Dreissen, R. Springer, N. Kirchgessner, R. Merkel, and B. Hoffmann. The constant beat: cardiomyocytes adapt their forces by equal contraction upon environmental stiffening. *Biol Open*, 2(3):351–361, Mar 2013.

[133] M. Chrzanowska-Wodnicka and K. Burridge. Rho-stimulated contractility drives the formation of stress fibers and focal adhesions. *J. Cell Biol.*, 133(6):1403–1415, Jun 1996.

[134] R. A. Worthylake, S. Lemoine, J. M. Watson, and K. Burridge. RhoA is required for monocyte tail retraction during transendothelial migration. *J. Cell Biol.*, 154(1):147–160, Jul 2001.

[135] G. P. Nader, E. J. Ezratty, and G. G. Gundersen. FAK, talin and PIPKIγ regulate endocytosed integrin activation to polarize focal adhesion assembly. *Nat. Cell Biol.*, 18(5):491–503, 05 2016.

[136] D. T. Burnette, S. Manley, P. Sengupta, R. Sougrat, M. W. Davidson, B. Kachar, and J. Lippincott-Schwartz. A role for actin arcs in the leading-edge advance of migrating cells. *Nat. Cell Biol.*, 13(4):371–381, Apr 2011.

[137] W. T. Chen. Mechanism of retraction of the trailing edge during fibroblast movement. *J. Cell Biol.*, 90(1):187–200, Jul 1981.

[138] M. F. Carlier, V. Laurent, J. Santolini, R. Melki, D. Didry, G. X. Xia, Y. Hong, N. H. Chua, and D. Pantaloni. Actin depolymerizing factor (ADF/cofilin) enhances the rate of filament turnover: implication in actin-based motility. *J. Cell Biol.*, 136(6):1307–1322, Mar 1997.

[139] P. Hotulainen, E. Paunola, M. K. Vartiainen, and P. Lappalainen. Actin-depolymerizing factor and cofilin-1 play overlapping roles in promoting rapid F-actin depolymerization in mammalian nonmuscle cells. *Mol. Biol. Cell*, 16(2):649–664, Feb 2005.

[140] S. Tojkander, G. Gateva, A. Husain, R. Krishnan, and P. Lappalainen. Generation of contractile actomyosin bundles depends on mechanosensitive actin filament assembly and disassembly. *Elife*, 4:e06126, Dec 2015.

[141] Mitchison T. J. Actin based motility on retraction fibers in mitotic ptk2 cells. *Cell Motility*, 22(2):135–151, 1992.

[142] A. M. Fenix, N. Taneja, C. A. Buttler, J. Lewis, S. B. Van Engelenburg, R. Ohi, and D. T. Burnette. Expansion and concatenation of non-muscle myosin IIA filaments drive cellular contractile system formation during interphase and mitosis. *Mol. Biol. Cell*, Mar 2016.

[143] J. R. Beach, K. S. Bruun, L. Shao, D. Li, Z. Swider, K. Remmert, Y. Zhang, M. A. Conti, R. S. Adelstein, N. M. Rusan, E. Betzig, and J. A. Hammer. Actin dynamics and competition for myosin monomer govern the sequential amplification of myosin filaments. *Nat. Cell Biol.*, 19(2):85–93, 02 2017.

[144] S. Hu, K. Dasbiswas, Z. Guo, Y. H. Tee, V. Thiagarajan, P. Hersen, T. L. Chew, S. A. Safran, R. Zaidel-Bar, and A. D. Bershadsky. Long-range self-organization of cytoskeletal myosin II filament stacks. *Nat. Cell Biol.*, 19(2):133–141, 02 2017.

[145] M. H. Jorrisch, W. Shih, and S. Yamada. Myosin IIA deficient cells migrate efficiently despite reduced traction forces at cell periphery. *Biol Open*, 2(4):368–372, Apr 2013.

[146] C. Mohl, N. Kirchgessner, C. Schafer, K. Kupper, S. Born, G. Diez, W. H. Goldmann, R. Merkel, and B. Hoffmann. Becoming stable and strong: the interplay between vinculin exchange dynamics and adhesion strength during adhesion site maturation. *Cell Motil. Cytoskeleton*, 66(6):350–364, Jun 2009.

[147] L Tan, T Meyer, B Pfau, T Hofmann, TW Tan, and D Jones. Rapid vinculin exchange dynamics at focal adhesions in primary osteoblasts following shear flow stimulation. *Journal of musculoskeletal and neuronal interactions*, 10(1):92—99, March 2010.

[148] E. Zamir, M. Katz, Y. Posen, N. Erez, K. M. Yamada, B. Z. Katz, S. Lin, D. C. Lin, A. Bershadsky, Z. Kam, and B. Geiger. Dynamics and segregation of cell-matrix adhesions in cultured fibroblasts. *Nat. Cell Biol.*, 2(4):191–196, Apr 2000.

[149] L. B. Smilenov, A. Mikhailov, R. J. Pelham, E. E. Marcantonio, and G. G. Gundersen. Focal adhesion motility revealed in stationary fibroblasts. *Science*, 286(5442):1172–1174, Nov 1999.

[150] K. I. Anderson and R. Cross. Contact dynamics during keratocyte motility. *Curr. Biol.*, 10(5):253–260, Mar 2000.

[151] C. Ballestrem, B. Wehrle-Haller, B. Hinz, and B. A. Imhof. Actin-dependent lamellipodia formation and microtubule-dependent tail retraction control-directed cell migration. *Mol. Biol. Cell*, 11(9):2999–3012, Sep 2000.

[152] P. E. Hughes, M. W. Renshaw, M. Pfaff, J. Forsyth, V. M. Keivens, M. A. Schwartz, and M. H. Ginsberg. Suppression of integrin activation: a novel function of a Ras/Raf-initiated MAP kinase pathway. *Cell*, 88(4):521–530, Feb 1997.

[153] C. D. Nobes and A. Hall. Rho GTPases control polarity, protrusion, and adhesion during cell movement. *J. Cell Biol.*, 144(6):1235–1244, Mar 1999.

[154] V. J. Fincham, M. James, M. C. Frame, and S. J. Winder. Active ERK/MAP kinase is targeted to newly forming cell-matrix adhesions by integrin engagement and v-Src. *EMBO J.*, 19(12):2911–2923, Jun 2000.

[155] A. D. Bershadsky, N. Q. Balaban, and B. Geiger. Adhesion-dependent cell mechanosensitivity. *Annu. Rev. Cell Dev. Biol.*, 19:677–695, 2003.

[156] C. Grashoff, B. D. Hoffman, M. D. Brenner, R. Zhou, M. Parsons, M. T. Yang, M. A. McLean, S. G. Sligar, C. S. Chen, T. Ha, and M. A. Schwartz. Measuring mechanical tension across vinculin reveals regulation of focal adhesion dynamics. *Nature*, 466(7303):263–266, Jul 2010.

[157] R. Karlsson, A. Michaelsson, and L. Mattsson. Kinetic analysis of monoclonal antibody-antigen interactions with a new biosensor based analytical system. *J. Immunol. Methods*, 145(1-2):229–240, Dec 1991.

[158] V. Cherkas, S. Grebenyuk, D. Osypenko, A. V. Dovgan, E. O. Grushevskyi, M. Yedutenko, Y. Sheremet, A. Dromaretsky, A. Bozhenko, K. Agashkov, N. I. Kononenko, and P. Belan. Measurement of intracellular concentration of fluorescently-labeled targets in living cells. *PLoS ONE*, 13(4):e0194031, 2018.

[159] D. G. Myszka, X. He, M. Dembo, T. A. Morton, and B. Goldstein. Extending the range of rate constants available from BIACORE: interpreting mass transport-influenced binding data. *Biophys. J.*, 75(2):583–594, Aug 1998.

List of Figures

List of Tables

Acknowledgements

During the tenure of my PhD, I had the privilege of working with some extremely skilled people. I feel blessed to have them as my guides.

First and foremost, I would like to pay my sincere gratitude to my Doktorvater, Prof. Dr. Rudolf Merkel, for giving me an opportunity of working as a part of his research group. The door to his office was always open whenever i had questions about my research or writing. I thank him for being a critical reader of this thesis and for his valuable comments on it. With his bag full of ideas and never ending enthusiasm for science, he is someone I will always look up to.

I would like to extend my gratitude to other members of my PhD committee, Prof. Ulrich Kubitscheck (Institut für Physikalishe und Theoretische Chemie), Prof. Dr. Arne Lützen (Institut für Organische Chemie und Biochemie) and Dr. Gregor Kirfel (Institut für Zellbiologie), for taking their valuable time to evaluate this thesis.

Arriving into a new country and adjusting myself to an absolutely foreign work culture wouldn't have been possible without the support of Priv-Doz. Dr. Bernd Hoffmann (ICS7). In times of experimental struggles, I always had his expert suggestions, for which I am sincerely greatful. Regular discussions with him were incredibly helpful in finding my way through the project. His scientific intellect and the attitude of working hard, has always been and will be an inspiration to me.

My sincere thanks to our collaborators Dmytro Kotsur and Dr. Julian Mattes from Software Competence Center Hagenberg (Austria), for developing the stress fiber tracking software. Their inputs into framing the image processing routines for actin stress fiber related data, have been extremely valuable.

My special gratitue to the 'I-Tea' team of ICS7, Georg Dreissen and Dr. Ronald Springer. They have been a great support with all my technical issues. No matter how big or small the problems were, they were always available to find a solution. I would like to especially thank Georg Dreissen, for creating MatLab programs and making my image processing experience much less scary!

Learning and operating microscopic techniques wouldn't have been possible without the help of Nico Hampe (ICS7). I thank him for his amazing problem solving skills and for his patience with answering my infinite questions. A big thanks to the pillars of ICS7 laboratory, Simone Stiefel, Nils Hersch and Christina Linnartz, who have been brilliant in making lab plannings, schedules and introductions to new instruments.

Surviving together through all ups and downs during experiments, I shared an immense amount of knowledge and experience with Galiya Sakaeva. She has been a great officemate and moreover, a great friend. I thank her for all the cell culture support and discussions during standardization of experiments with nHEKs.

Most importantly, I acknowledge the help and support of Claudia Klamandt (secretory, ICS7), who made dealing with dreadful German paper work really smooth. She was always welcoming and ready to help with the most annoying of the stuff, with a big smile on her face.

Additional note of thanks to Lisann Eβer, Dr. Aljona-Gaiko Shcherbak, Dr. Tobias Braun, Tabea Wiedenhöft and Rejhana Kolasinac, for their cooperation and understanding while sharing the cell culture lab. Also, big thanks to other members of ICS7 like Krishna Sridhar, Jella Abraham, Dave Ahrens, Laura Schmidt, Dr. Gloria Fabris and Dr. Marco Hoffmann for creating a cheerful work environment.

Except of the institute, I would like to pay my gratitude towards all members of InCeM, our European Union's cell migration studies team, with whom I have had some great discussions. Interactions with fellow students and faculty members from different scientific disciplines, has helped me improve my scientific thought process. Special thanks to InCeM administrators Christine Kempchen, Prof. Rudolf Leube and Dr. Reinhard Windoffer, for putting up great opportunities for us, InCeM students.

Last but not the least, my most special gratitude to my dearest Soumik Ray, for providing me with unfailing support and continuous encouragement throughout the years and through the process of writing this thesis. Finally, I must express my profound gratitude to my mother, father, brother and grandparents, for their extraordinary love and support. Their blessings, although from miles away, were always there! This accomplishment wouldn't have been possible without them. Thank you!

Appendix: List of Abbreviations

°C	Degree celcius
μg	Microgram
μm	Micrometer
ADP	Adenosine-5’-diphosphate
Arp2/3	Actin related protein 2 and 3
ATP	Adenosine-5’-triphosphate
AU	Airy unit
C_c	Critical concentration
Ca^{2+}	Calcium ion
CLSM	Confocal laser scanning microscope
cm	Centimeter
CO_2	Carbon dioxide
DSFs	Dorsal stress fibers
d-end	Distal end
ECM	Extracellular matrix
EGF	Epidermal growth factor
EGFR	Epidermal growth factor receptor
F-actin	Filamentous actin
FAK	Focal adhesion kinase

FAs	Focal adhesions
FP	Fillopodium
FXs	Focal complexes
G-actin	Globular actin
GaAsP	Gallium Arsenide Phosphide detector
HeNe	Helium Neon
kDa	Kilodalton
LM	Lamellum
LP	Lamellipodium
MFA	Mature focal adhesions
mg	Milligram
Mg^{2+}	Magnesium ion
MHC	Myosin heavy chain
min	Minute
ml	Milliliter
NA	Numerical aperture
NBC	Nucleotide binding cleft
NFA	Nascent focal adhesions
nHEKs	Normal human epidermal keratinocytes
nm	Nanometer
NMMIIA	Non-muscle myosin IIA
PAFPs	Photoactivable fluorescent proteins

PCFPs	Photoconvertable fluorescent proteins
PBS	Phosphate buffered saline
p-end	Proximal end
P_i	Inorganic phosphate
PSFPs	Photoswitchable fluorescent proteins
PSF	Point spread function
RLC	Regulatory light chain
ROI	Region of interest
RSFs	Rear-end ventral stress fibers
sec	Seconds
SFA	Sliding focal adhesions
SFs	Stress fibers
SNR	Signal to noise ratio
TAs	Transverse arcs
VSFs	Ventral stress fibers
WASP	Wiscott-Aldrich syndrome protein